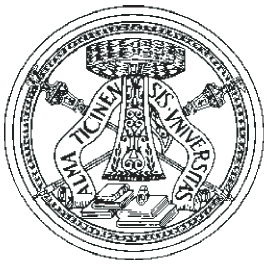

UNIVERSITY OF PAVIA

DEPARTMENT OF PHYSICS "ALESSANDRO VOLTA"

Dottorato di Ricerca in Fisica – XVII ciclo –

PHOTONIC MODES AND RADIATION-MATTER INTERACTION IN PHOTONIC CRYSTAL SLABS

Doctoral thesis by

DARIO GERACE

Supervisor: Prof. Lucio Claudio ANDREANI

To Sara

Contents

Abstract

In the present work we report on a theoretical investigation of electromagnetic radiation modes in planar dielectric waveguides periodically textured with either one- or two-dimensional patterns. This kind of systems, commonly called *photonic crystal slabs*, allow for a three-dimensional control of light propagation or confinement owing to the in-plane photonic band gap properties added to the vertical dielectric confinement. These systems are currently much studied owing not only to their interesting applicative perspectives, but also for their fundamental physical peculiarities. The analysis is carried out by using a recently developed theoretical method, called Guided-Mode Expansion. The light line issue, which allows for a distinction between truly guided, quasi-guided and leaky modes, is presented and discussed. Systems either completely periodic or with controlled defects are considered, in order to study the main physical properties of either delocalized or confined photonic modes. In particular, we consider both cavity modes in one-dimensional photonic crystal slabs, addressing the problem of the efficient determination of their quality factors, and line-defect waveguides in two-dimensional photonic crystal slabs, for which we study the propagation losses induced by intrinsic as well as extrinsic scattering mechanisms. It is shown that propagation losses comparable to high refractive index strip waveguides can be achieved with state-of-the-art fabrication technology of photonic crystal waveguides, which promises to be an important issue in view of prospective applications of such systems to integrated optics. Comparisons with recent experimental results are also provided throughout the work, which put our theoretical analysis on a solid basis. Finally, the problem of the strong coupling between radiation modes in photonic crystal slabs and material dipole-active excitations in semiconductors is theoretically treated by using a quantum mechanical formalism. It is shown that the interplay between light and matter can lead to the formation of mixed states, or a new kind of quasi-particles, which we call *photonic crystal polaritons*.

Introduction

The understanding of fundamental physical mechanisms underlying phenomena such as the propagation of light and its interaction with matter is one of the major conquests of human thinking. The classical theory of electromagnetism has allowed to explain, substantially, all electromagnetic phenomena since 1864[1]. The fusion of relativistic electromagnetic theory, where electric and magnetic fields are intended as components of a unique electromagnetic tensor, and Quantum Mechanics led, in the middle of the past century, to the most powerful theoretical construction that we have in Physics, namely Quantum Electrodynamics[2]. This theory brought a great insight on how things really go at the microscopic level, when electromagnetic radiation and ordinary matter manifest their pure quantum nature. Anyway, classical electromagnetism has not gone out of fashion during these decades. On the contrary, Maxwell's equations still represent a priceless source of information in many everyday problems.

It was, in some sense, a surprise for many scientists that at the end of XX century Maxwell's equations could still predict new physical phenomena. Indeed, every non scalar electromagnetic problem is a very complicated one, and many problems still have no exact analytical solution owing to the intrinsic vectorial nature of Maxwell's equations. The main source of new physical discoveries during the last decades in low-energy physics has been the understanding that radiation-matter interaction is not an unchanging property of material systems. Indeed, the spontaneous emission of photons from electronic excited states of atoms and molecules can be modified, e.g, by modifying the density of radiation modes interacting with those states [1]. Things began to be interesting for many physicists when the possibilities to artificially manipulate electromagnetic density of states in real systems grew together with the advances in nano-fabrication technology, allowing for

[1]This is the year in which James Clerk Maxwell published his seminal treatise on the "dynamic theory of the electromagnetic field," setting up the basis of fundamental equations for the evolution of electric and magnetic fields bringing his name.

[2]It is still the theory best verified experimentally.

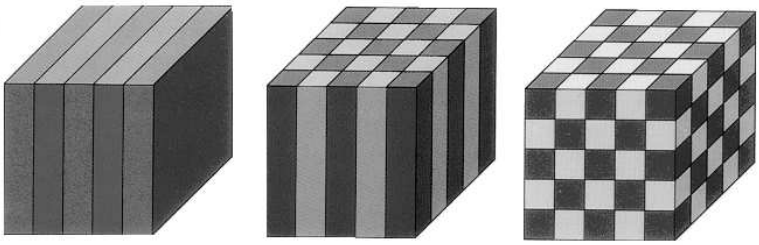

Figure 1: A schematic view of (a) one-dimensional, (b) two-dimensional and (c) three-dimensional photonic crystal structures, made by the periodic alternation of two different dielectric materials. Drawings taken from Ref. [5].

the tailoring of radiation-matter interaction at optical wavelengths. A fruitful source of discoveries in the last decades has been the proposal to modify the radiation properties of materials by fabricating artificial structures called *photonic crystals*.

In 1987 two seminal papers by Yablonovitch [2] and John [3] appeared almost simultaneously, giving rise to a new field of research concerning the study of physical properties of periodic dielectric media in one, two and three dimensions. In analogy with the periodic arrangement of atoms in ordinary crystals, these meta-materials were generically addressed to as *photonic crystals*. Schematic illustrations of such systems are given in Fig. 1. They are commonly constituted by two dielectric (non-magnetic) materials arranged in space with a certain periodic lattice. Indeed, one-dimensional (1D) photonic crystals have been studied for a long time as they provide far better reflection properties than metallic mirrors at optical wavelengths, and are commonly known as Bragg mirrors [4]. The electromagnetic problem for Bragg mirrors can be reduced to a scalar wave equation, whose solution is known for the majority of practical cases. On the contrary, the vectorial nature of the electromagnetic field leads to additional complication for two-dimensional (2D) or three-dimensional (3D) structures. The great interest of scientific community over the potential applications of photonic crystals is witnessed also by the huge amount of papers published in the last years on these topics (see also Refs. [5, 6, 7] and references therein).

The great intuition, which gave rise to new research efforts all over the world, has been to exploit the analogies between photonic and ordinary matter crystals. It was understood that the periodic dielectric function acts for photons in a way analogous to the periodic crystalline potential for electrons. From Solid State Physics, it is known that this periodic potential

is at the origin of the electronic band structure and band gaps [8]. Thus, one can reasonably expect that the dispersion of photons is greatly modified in photonic crystals as compared to homogeneous media. In particular, it seemed very interesting since the beginning of this active field of research the possible existence of photonic band gaps, i.e. frequency regions in which no photonic modes are allowed to propagate in the meta-material. Owing to the vectorial nature of the electromagnetic field, a photonic band gap is complete only if it exists in a given frequency range for all possible polarization states. Anyway, the photonic band gap may be truly complete only for three dimensional photonic crystals, because light propagation would be inhibited in any direction. This, added to the unique properties of Maxwell's equations that have no fundamental length scale (unlike, e.g., Schrödinger's equation in which there is the Planck constant), which gives rise to photonic band structures scalable according to the lattice constant [5], makes three dimensional photonic crystals very attractive for the control of the light propagation at optical wavelengths. Furthermore, if we introduce a structural defect in the otherwise periodic lattice of a photonic crystal, mid-gap modes whose eigenfunctions could be strongly localized may be obtained, giving rise to intra-gap defect modes in close analogy to impurity states in semiconductors or insulators. Thus, the potential importance of researching on photonic crystals is twofold. On one side, it is intuitive that the proper design of structural defects (linear or localized) into photonic crystals would allow to fabricate lossless waveguides or very high-Q cavities. Such waveguides would allow, e.g., to create optical interconnects with very sharp bends, thus going beyond the intrinsic curvature limits imposed by total internal reflection in commonly used dielectric waveguides [5]. These concepts clearly points at all-optical integration of many components (such as waveguides, resonators, add/drop filters, splitters, combiners, etc.) on a single photonic crystal chip. On the other hand, the spontaneous emission of atoms embedded in a 3D photonic crystal can be inhibited, if its resonance frequency lies within the photonic band gap, or enhanced and reshaped by photonic band structure (whose dispersion can be substantially different from the dispersion of light in a homogeneous medium). The latter aspect is concerned mostly with the fundamental understanding of radiation-matter interaction properties. After these first proposals made on a theoretical basis, the great challenge in the last years has been the fabrication of structures with minimum degree of imperfections, in order to reproduce the results predicted by theoretical calculations. Unfortunately, this challenge has proven too hard for current technology possibilities when dealing with 3D photonic crystals at sub-micrometric scales. In particular, there are many difficulties in introducing controlled line or point defects into 3D structures with robust photonic

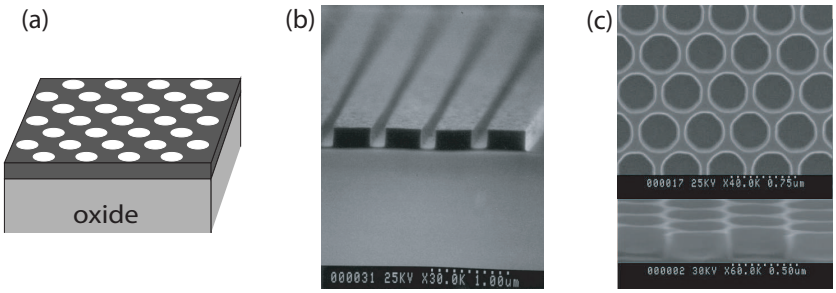

Figure 2: (a) Schematic picture of a planar waveguide patterned with a periodic lattice in the plane, or *photonic crystal slab*. SEM images (courtesy of D. Peyrade and M. Belotti) of Silicon-on-Insulator (b) 1D photonic crystal slab of Silicon stripes and (c) 2D photonic crystal slab with a triangular lattice of air holes in a Silicon background.

gaps.

In the last few years two-dimensional photonic crystal structures embedded in a planar dielectric waveguide geometry, commonly known as *photonic crystal slabs*, have been receiving much attention because they allow for a three dimensional control of light and retain or approximate many of the desired properties of 3D photonic crystals, but they are much more easily realized at sub-micron lengths. In these systems, the propagation or confinement of electromagnetic field is controlled by the photonic crystal structure in the 2D plane, and by the dielectric discontinuity provided by the slab waveguide in the vertical direction. A typical system is schematically displayed in Fig. 2a. Photonic crystal slabs are usually fabricated on a substrate made of a semiconductor or an insulator material. Many sophisticated technologies such as electron beam lithography and thin layer growing have been developed in the field of microelectronics and optoelectronics, and can be applied to their fabrication. Examples of fabricated structures are given in Figs. 2b and c for one- and two-dimensional in-plane periodicity, respectively. Both 1D and 2D samples shown in the figures were fabricated at the "Laboratoire de Photonique et Nanostructure," CNRS, Paris-Marcoussis, France, within a collaboration with the group of Prof. Y. Chen, "Ecole Normale Superieure," Paris. Silicon layers of thickness 260 nm were deposited on Silicon dioxide substrates and patterned by using electron-beam lithography and reactive ion etching to design the sub-micrometer periodic lattices. These photonic crystal slabs are commonly known as Silicon-on-Insulator (SOI) structures.

Most experimental investigations of photonic crystal slabs with a one- or two-dimensional periodic lattice concern in-plane transmission [9–12] or

surface reflectance/transmittance measurements [13–19] with the purpose of determining the photonic gaps and the band dispersion. Structures containing defect states like microcavities in 1D systems [20–22] or linear waveguides in 2D lattices [23–26] were also experimentally investigated. On the theoretical side, the study of photonic crystal slabs has been undertaken with plane-wave expansion method [27–30], scattering-matrix or grating theory approaches [31, 32], exact finite-difference time-domain (FDTD) calculations [33–36], modal methods [37–40], and perturbative approaches [41–43]. Most of these papers concern 2D structures, either periodic or with linear defects, though each theoretical method has its drawbacks and limitations. The theoretical study of 1D structures is restricted to a few papers and mostly focused onto the optical response in both in-plane [38, 40] and out-of-plane [18, 19, 22, 32, 43] configurations. For a thorough historical review of past research on photonic crystals and photonic crystal slabs see also [44]. Recent research developments and guidelines in these fields can be found in Ref. [45].

The present work aims at giving an original contribution to the development of some "hot" research topics within the photonic crystal scientific community, concerning the study of 1D and 2D photonic crystal slabs. Theoretical research has been carried out by using a recently developed numerical method [46–48], which allow for a fast and accurate calculation of the main physical properties, such as photonic band dispersion and out-of-plane losses of leaky modes, for photonic crystal slabs with one- and two-dimensional in-plane periodicity and strong refractive index contrast out of the slab plane. Objects of the present work are photonic crystals patterned in core layers of a high index material (such as Silicon or GaAs) between low index semi-infinite media, e.g. photonic crystal membranes or asymmetric photonic crystal slabs grown on a low index substrate (oxide), like the ones shown in Fig. 2.

Two guiding lines have been followed throughout this work on the eigenmodes in photonic crystal slabs: on one side the theoretical understanding of application-oriented physical properties, on the other the development of theoretical tools concerning more fundamental investigations of radiation-matter interaction effects in such systems. The analysis has been concentrated on both one- and two-dimensional periodic systems, either defect-free or with point or linear defects within the otherwise periodic structure. In particular, issues such as the determination of the quality factor for cavity modes in Fabry-Pérot cavities embedded in 1D photonic crystal slabs, and the calculation of disorder-induced out-of-plane losses for linear defect states in 2D photonic crystal slabs are addressed. Original results that may be of great importance for prospective applications of these systems to integrated optics

are presented. From a more fundamental point of view, a quantum theory of the exciton-photon coupling in photonic crystal slabs with embedded semiconductor quantum well(s) within the core layer of the planar waveguide is formulated. The weak and strong coupling regimes in both 1D and 2D lattices are studied, and the conditions for the formation of mixed states of radiation and material excitations are theoretically determined. These results still await for experimental confirmation.

This thesis basically relies on various collaborations and projects carried out by the Solid State Theory group at the University of Pavia, headed by Prof. L.C. Andreani. Part of the work has been financed by "Istituto Nazionale per la Fisica della Materia" (INFM) through the project PRA-Photonic, and by "Ministero dell'Istruzione, dell'Università e della Ricerca Scientifica" (MIUR), through the project Cofinanziamento-2002. The latter involves, besides the University of Pavia, which participates with both the experimental group of Prof. G. Guizzetti and the theoretical group of Prof. L.C. Andreani, the Universities of Torino,Trento, Firenze, and TASC-ELETTRA Synchrotron at Trieste. Collaborations with the group of Prof. Y. Chen at LPN-CNRS, Paris-Marcoussis, France, brought the Silicon-on-Insulator samples whose characterization is shown in this work. Experiments of angle-resolved reflectance are carried out at the optical spectroscopy laboratory of the Department of physics "Alessandro Volta," University of Pavia.

The presentation of the work is organized as follows. In the first Chapter, after an introduction to the general solution of Maxwell's equations in photonic crystals and uniform planar waveguides, the theoretical formulation of the method is presented. The successive chapters deal with the presentation of results. In Chapter 2 one-dimensional photonic crystal slabs are addressed, in both periodic and with point defects configurations for membrane and SOI structures. Two-dimensional photonic crystal slabs are studied in Chapter 3, periodic and with linear defects in a triangular lattice of air holes on membrane and SOI. Finally, a quantum theory of radiation-matter interaction for quantum well excitons in 1D and 2D photonic crystal slabs is presented in Chapter 4, where results on the formation of new quasi-particles that we call *photonic crystal polaritons* are discussed. Numerical results and comparisons with available experimental data, either from the optical spectroscopy group of the University of Pavia or from the literature, are extensively presented and commented. Some of the work and the main scientific results have already appeared, usually more synthetically, in various journals [49–53], or they will appear in forthcoming issues in the next months [54, 55].

Chapter 1

Theory of photonic eigenmodes

In this Chapter an outlook is given about the theoretical framework used to study both numerically and analytically the physical properties of photonic crystal slabs in the present work. Photonic crystal slabs are constituted by planar dielectric waveguides periodically patterned in the plane. The two constituent systems, namely the ideal two-dimensional photonic crystal and the uniform planar slab, will be separately introduced in the first Section. Finally, in the second Section the physics of these two systems will be put together and the theory of photonic eigenmodes in photonic crystal slabs will be pointed out. This method was first proposed in Refs. [46, 47] as a fast and accurate numerical tool for calculating the main dispersive properties of photonic crystal slabs, and it has been successively extended in order to treat also the problem of both intrinsic [48] and extrinsic (that is disorder-induced) [50] out-of-plane radiation losses within a perturbative formalism. Numerical results concerning both one- and two-dimensional photonic systems in the plane of the waveguide will be extensively presented in the next two chapters.

1.1 Solutions of Maxwell's equations

It is well known that in a uniform, isotropic and non dispersive medium of refractive index n the dispersion relation of the radiation field, that is the expression relating the frequency (or energy) of the electromagnetic field and the wave vector $\mathbf{k}$, is simply given by

$$\omega = \frac{c}{n}|\mathbf{k}| \tag{1.1}$$

where $v = c/n$ is the group velocity of the field in the medium. The dispersion $\omega = \omega(\mathbf{k})$ can be greatly changed by modifying the structural properties

of dielectric materials, e.g. by using photonic crystals or dielectric waveguides. As already introduced, photonic crystals are meta-materials basically constituted of two different dielectric media periodically arranged in space in one, two or three dimensions (see Fig. 1). The dispersion of photonic modes in a photonic crystal is characterized by the presence of band gaps, i.e. frequency regions for which the propagation of the electromagnetic field is inhibited within the medium. The photonic band dispersion is one of the main concepts that allows to study and understand the interesting physics of these systems. The following paragraph is devoted to the introduction of basic concepts related to photonic band calculations by using the plane wave expansion method. The wave equations formulated as an eigenvalue problem will be discussed, and a general numerical method to solve it will be given for two-dimensionally periodic systems, for which the vectorial wave equation reduces to two independent scalar equations. In the second paragraph the solution of Maxwell's equation in planar dielectric slabs will be described, leading to the calculation of photonic eigenmodes and to the definition of guided and radiative eigenmodes.

1.1.1 Eigenmodes in periodic dielectric media

The starting point of every electromagnetic study is the formulation of the problem in terms of Maxwell's equations. In particular, eigenmodes in photonic crystals are essentially the solution of the classical problem posed by Maxwell's equations in a medium with spatial periodicity in either the dielectric constant, either the magnetic permeability, or both. In the following we will assume that free charges and electric currents are absent, in order to calculate the proper eigenmodes of the electromagnetic field neglecting radiation-matter interaction (the latter will be treated from a quantum point of view in the last Chapter of this work). Under these assumptions, Maxwell's equations in Gaussian units read

$$\nabla \cdot \mathbf{D}(\mathbf{r},t) = 0, \qquad \nabla \times \mathbf{E}(\mathbf{r},t) = -\frac{1}{c}\frac{\partial}{\partial t}\mathbf{B}(\mathbf{r},t), \tag{1.2}$$

$$\nabla \cdot \mathbf{B}(\mathbf{r},t) = 0, \qquad \nabla \times \mathbf{H}(\mathbf{r},t) = \frac{1}{c}\frac{\partial}{\partial t}\mathbf{D}(\mathbf{r},t). \tag{1.3}$$

The electric and magnetic fields, $\mathbf{E}$ and $\mathbf{H}$, are related to electric displacement ($\mathbf{D}$) and magnetic induction ($\mathbf{B}$) by the constitutive relations

$$\mathbf{D}(\mathbf{r},t) = \overline{\epsilon}(\mathbf{r})\mathbf{E}(\mathbf{r},t), \qquad \mathbf{B}(\mathbf{r},t) = \overline{\mu}(\mathbf{r})\mathbf{H}(\mathbf{r},t), \tag{1.4}$$

where $\overline{\epsilon}$ and $\overline{\mu}$ are the electric and magnetic function tensors, respectively. We assume that the media composing the photonic crystal structure are

isotropic, i.e. $\overline{\epsilon} = \epsilon$ and $\overline{\mu} = \mu$. We further assume that the media are non-magnetic, i.e. $\mu = 1$ and $\mathbf{B} = \mathbf{H}$. Finally, by taking an oscillating temporal dependence of the fields

$$\mathbf{E}(\mathbf{r}, t) = \mathbf{E}(\mathbf{r})e^{-i\omega t} \quad \mathbf{H}(\mathbf{r}, t) = \mathbf{H}(\mathbf{r})e^{-i\omega t} \tag{1.5}$$

the general solution of Maxwell's wave equations can be found as a superposition of harmonics, thanks to the linearity of the electromagnetic problem. By inserting Eqs. 1.5 in Eqs. 1.2 and 1.3, taking into account the constitutive equations and the assumptions made above, Maxwell's equations can be written in the closed, second-order forms for either the electric or the magnetic fields

$$\nabla \cdot \epsilon(\mathbf{r})\mathbf{E}(\mathbf{r}) = 0, \qquad \nabla \times \nabla \times \mathbf{E}(\mathbf{r}) = \frac{\omega^2}{c^2}\epsilon(\mathbf{r})\mathbf{E}(\mathbf{r}), \tag{1.6}$$

$$\nabla \cdot \mathbf{H}(\mathbf{r}) = 0, \qquad \nabla \times \left(\frac{1}{\epsilon(\mathbf{r})}\nabla \times \mathbf{H}(\mathbf{r})\right) = \frac{\omega^2}{c^2}\mathbf{H}(\mathbf{r}). \tag{1.7}$$

It is evident that the equations at the right hand side can be reformulated in terms of eigenvalue problems, appearing very similar to stationary Schrödinger equation [5]. In particular, the role of the hamiltonian is replaced here by a differential operator whose *potential* is represented by $[1 - \epsilon(\mathbf{r})]\omega^2/c^2$. Notice that this effective potential for photons enters as a multiplication factor, instead of an additive one as for material particles obeying Schrödinger equation. The main difference between Eqs. 1.6 and 1.7 and the Schrödinger equation, however, is the vectorial nature of the electromagnetic field as compared to matter fields. It is more convenient to work with Maxwell's equation for the magnetic field, because $\mathbf{H}$ is transverse (see left hand side in Eq. 1.7) and the master equation has the typical form of an eigenvalue problem [5]. In fact, since the divergence equation for the $\mathbf{E}$-field involves the spatially dependent dielectric constant, the corresponding wave equation on the right hand side of Eq. 1.6 has the form of a generalized eigenvalue problem, which is more complicated to solve [5]. From now on, we will consider the solutions of Maxwell's equations as coming from the solution of the second equation in Eq. 1.7. After the solution of the second-order equation for the magnetic field, the electric field can be obtained from the relation

$$\mathbf{E}(\mathbf{r}) = i\frac{c}{\omega\epsilon(\mathbf{r})}\nabla \times \mathbf{H}(\mathbf{r}), \tag{1.8}$$

which comes from the right hand side of Eq. 1.3, considering the first relations in Eqs. 1.4 and 1.5.

Until now we have not specified any particular initial conditions for the electromagnetic problem. Thus, the next step is to impose the periodic spatial dependence of $\epsilon(\mathbf{r})$, which characterizes photonic crystals. The periodicity can be in one, two or three dimensions, as schematically depicted in

Fig. 1. It can be seen that the photonic structure of a photonic crystal can be constructed by the repetition of a given unit cell according to a specified periodic pattern. This can be reduced to only two concepts, namely a basis and a lattice. The photonic lattice defines the spatial arrangement of the unit cell, while the basis specifies the content of the unit cell. These concepts are borrowed from the principles of electronic band calculations in Solid State Physics [8]. The periodicity of $\epsilon(\mathbf{r})$ can be expressed by the relation

$$\epsilon(\mathbf{r}) = \epsilon(\mathbf{r} + \mathbf{R}) \tag{1.9}$$

where $\mathbf{R}$ is a vector defined by the linear combination of primitive lattice vectors $\mathbf{a}_i$, with i equal to the dimensions of the periodic lattice. The photonic crystal structure is invariant for any discrete translation defined by a vector $\mathbf{R}$ belonging to the vectorial space $\mathbb{V}$ with basis $\{\mathbf{a}_i\}$. The dimensionality of $\mathbb{V}$ is equal to the number of dimensions in which $\epsilon(\mathbf{r})$ is periodic. The master equation for the magnetic field can be rewritten as an eigenvalue problem

$$\hat{\mathbf{O}}(\mathbf{r})\mathbf{H}(\mathbf{r}) = \Omega\mathbf{H}(\mathbf{r}) \tag{1.10}$$

where the operator $\hat{\mathbf{O}}(\mathbf{r})$ and its eigenvalues are

$$\hat{\mathbf{O}}(\mathbf{r}) = \nabla \times \left(\frac{1}{\epsilon(\mathbf{r})}\nabla \times , \qquad \Omega = \frac{\omega^2}{c^2}\right. \tag{1.11}$$

It can be easily demonstrated that $\hat{\mathbf{O}}$ is hermitian and positive definite [5], thus it has real and positive eigenvalues with a complete set of orthonormal eigenvectors. The eigenvectors $\mathbf{H}(\mathbf{r})$ are the field patterns of the harmonic modes whose frequencies are obtained by the corresponding eigenvalues as $\omega = c\sqrt{\Omega}$.

The operator formalism, very similar to the Hamiltonian formulation of quantum mechanics, and the spatial periodicity of the effective potential for this electromagnetic problem allow for a direct application of concepts and theorems known from Solid State theories. In particular, Bloch's theorem can be applied to Eq. 1.10 as in the case of electronic wave equation in ordinary crystals with a periodic potential due to the regular arrangement of atoms. The discrete translation operator $\hat{T}_{\mathbf{R}}$, with $\mathbf{R} \in \mathbb{V}$, commutes with the "hamiltonian" $\hat{\mathbf{O}}$ and the two operators possess a common set of eigenvectors; $\mathbf{k}$ is a good "quantum number" for this problem [8]. This statement is known as the Bloch-Floquet theorem when applied to electromagnetic problems: *The general solution of Eq. 1.10 under the condition of discrete translational invariance expressed by Eq. 1.9 is given by a function* $\mathbf{u}_{\mathbf{k}}(\mathbf{r})$ *having the same periodicity of* $\epsilon(\mathbf{r})$*, multiplied by a phase factor* $\exp(i\mathbf{k}\cdot\mathbf{r})$[1]. The concepts

[1]The demonstration of Bloch-Floquet theorem is easily obtained by noting that the discrete translation operator commutes with the operator $\hat{\mathbf{O}}$. For an extensive proof we refer to Refs. [5] and [6].

of photonic band dispersion and of Bloch modes come now as a natural consequence from the basic aspects of electronic band calculations in solids. According to the Bloch-Floquet theorem, we can write the magnetic field in a photonic crystal as

$$\mathbf{H}_{\mathbf{k}}(\mathbf{r}) = e^{i\mathbf{k}\cdot\mathbf{r}}\mathbf{u}_{\mathbf{k}}(\mathbf{r}), \qquad \mathbf{u}_{\mathbf{k}}(\mathbf{r}) = \mathbf{u}_{\mathbf{k}}(\mathbf{r}+\mathbf{R}). \tag{1.12}$$

By substituting the first of Eq. 1.12 in the master equation 1.7, one gets the following equation for the periodic part of the magnetic field

$$(i\mathbf{k}+\nabla)\times\left[\frac{1}{\epsilon(\mathbf{r})}(i\mathbf{k}+\nabla)\times\mathbf{u}_{\mathbf{k}}(\mathbf{r})\right] = \frac{\omega_{\mathbf{k}}^2}{c^2}\mathbf{u}_{\mathbf{k}}(\mathbf{r}), \tag{1.13}$$

with the transversality condition $(i\mathbf{k}+\nabla)\cdot\mathbf{u}_{\mathbf{k}}(\mathbf{r}) = 0$. For each $\mathbf{k}$, the solutions of Eq. 1.13 are discretized and can be labelled by an integer index $n \in \mathbb{N}$. The photonic band structure is given by the family of continuous functions $\omega = \omega_n(\mathbf{k})$, indexed in order of increasing frequency by the band number. In in the photonic band dispersion there are frequency ranges in which there are no solutions for any $\mathbf{k}$, then the system has a *photonic band gap*.

In order to solve Eq. 1.13 explicitly, let us define the reciprocal space, coming from the periodicity of the dielectric constant. The dual space $\mathbb{G}$ of the space vector $\mathbb{V}$, whose set of primitive vectors can be generated by the set $\{\mathbf{a}_i\}$, is given by the condition $\mathbf{G}\cdot\mathbf{R} = 2\pi N$, where $N \in \mathbb{Z}$. A set of primitive vectors $\{\mathbf{b}_i\}$ is defined, in fact, by imposing that $\mathbf{a}_i \cdot \mathbf{b}_j = 2\pi\delta_{ij}$, where δ_{ij} is the Kronecker's delta. Thus, by recalling the relation $\mathbf{x}\cdot(\mathbf{x}\times\mathbf{y}) = 0$ of vectorial calculus, where $\mathbf{x}$ and $\mathbf{y}$ are generic vectors, the following rules can be applied to construct a number of primitive reciprocal lattice vectors depending on the dimensions of periodicity

$$\begin{cases} \mathbf{b}_i = 2\pi\frac{\mathbf{a}_j\times\mathbf{a}_k}{\mathbf{a}_i\cdot(\mathbf{a}_j\times\mathbf{a}_k)} & 3D \\ \mathbf{b}_i = 2\pi\lim_{\delta\to 0}\frac{\mathbf{a}_j\times\delta\hat{\mathbf{k}}}{\mathbf{a}_i\cdot(\mathbf{a}_j\times\delta\hat{\mathbf{k}})} & 2D \\ \mathbf{b}_1 = \frac{2\pi}{|\mathbf{a}_1|}\hat{\mathbf{a}}_1 & 1D \end{cases} \tag{1.14}$$

where for the 2D photonic crystal $\hat{\mathbf{k}}$ represents the direction of the z axis, and $\delta\hat{\mathbf{k}}$ is a vector basis of arbitrary length used to calculate the basis $\{\mathbf{b}_1, \mathbf{b}_2\}$, and whose length is sent to zero after performing the vectorial products. For each linear combination of the primitive lattice vectors, $\mathbf{R} = n_1\mathbf{a}_1 + n_2\mathbf{a}_2 + n_3\mathbf{a}_3$ and $\mathbf{G} = m_1\mathbf{b}_1 + m_2\mathbf{b}_2 + m_3\mathbf{b}_3$, the condition $\mathbf{G}\cdot\mathbf{R} = 2\pi N$ is thus satisfied. As in Solid State Physics, we can define a *Brillouin zone* in the reciprocal lattice, which is an ensemble of wave vectors $\mathbf{k}$ belonging to a spatial region delimited by cutting the reciprocal space with planes perpendicular to the primitive vectors at a distance $|\mathbf{b}_i|/2$ from the origin.

Only these wave vectors are needed to classify the photonic eigenmodes, intending both eigenvalues and eigenvectors. In fact, any other $\mathbf{k}'$ can be always obtained by $\mathbf{k}' = \mathbf{k} + \mathbf{G}$, for some $\mathbf{G} \in \mathbb{G}$ and $\mathbf{k}$ in the first Brillouin zone. A consequence of the translational invariance is that $\mathbf{H}_{\mathbf{k}}(\mathbf{r}) = \mathbf{H}_{\mathbf{k}'}(\mathbf{r})$ if $\mathbf{k}' - \mathbf{k} = \mathbf{G} \in \mathbb{G}$, and thus there would be some redundancy in labelling the eigenmodes with all the $\mathbf{k}$ vectors in reciprocal space, without introducing the concept of Brillouin zone.

Examples of primitive lattice vectors and of irreducible Brillouin zones for the simple photonic crystals displayed in Fig. 1 are schematically shown in Fig. 1.1. In this case, owing to the particular simplicity of the direct lattice, the primitive vectors can be obtained straightforwardly by Eq. 1.14 and form an orthogonal basis set. Obtaining $\{\mathbf{b}_i\}$ can be not so simple for more complicated lattices, but it is basically a geometrical problem. The bold lines in Fig. 1.1 mark the *irreducible Brillouin zone*, that is the region of reciprocal space irreducible with respect to the other possible symmetry transformations of the master equation. For instance, the invariance of Eq. 1.13 under time-reversal yields the equivalence $\omega_n(-\mathbf{k}) = \omega_n(\mathbf{k})$, which means that the photonic band structure can be calculated reducing the Brillouin zone to non-negative Bloch vectors. Fixed point symmetry transformations, such as rotations, inversions, reflections, gathered in the point group of the crystal, finally lead to the possibility of further reducing the Brillouin zone. It should be noticed from Fig. 1.1 that the irreducible Brillouin zone can be much smaller than the whole Brillouin zone, especially for 3D photonic crystals. Furthermore, to avoid solving the master equation for every point $\mathbf{k}$ in the irreducible Brillouin zone, it is often enough to calculate the bands along the main symmetry lines, which connect high symmetry points of the lattice (marked as Γ, X and M in the case of square or cubic lattices).

After defining the reciprocal space and the first Brillouin zone, the general form of Bloch states can be explicitly developed on a known basis of eigenfunctions in order to solve the master equation as a linear eigenvalue problem, like for electrons in solids. After almost 2 decades of research on photonic crystals, many techniques have been employed to calculate the photonic band structure. Anyway, the plane wave expansion method (PWE) has the powerful advantage of being straightforwardly applicable and easy to understand, even if its convergence properties are not always the optimum from a computational point of view. The method consists in solving Eq. 1.13 after the expansion of $\mathbf{u}_{\mathbf{k}}$ on a complete set of eigenfunctions. The most natural basis is represented by plane waves, as every periodic function can be expanded in Fourier series in the following way

$$\mathbf{u}_{\mathbf{k}}(\mathbf{r}) = \sum_{\mathbf{G}\in\mathbb{G}} \sum_{\sigma} c_{\mathbf{k}\sigma}(\mathbf{G}) \hat{\mathbf{e}}_{\sigma} e^{i\mathbf{G}\cdot\mathbf{r}}, \tag{1.15}$$

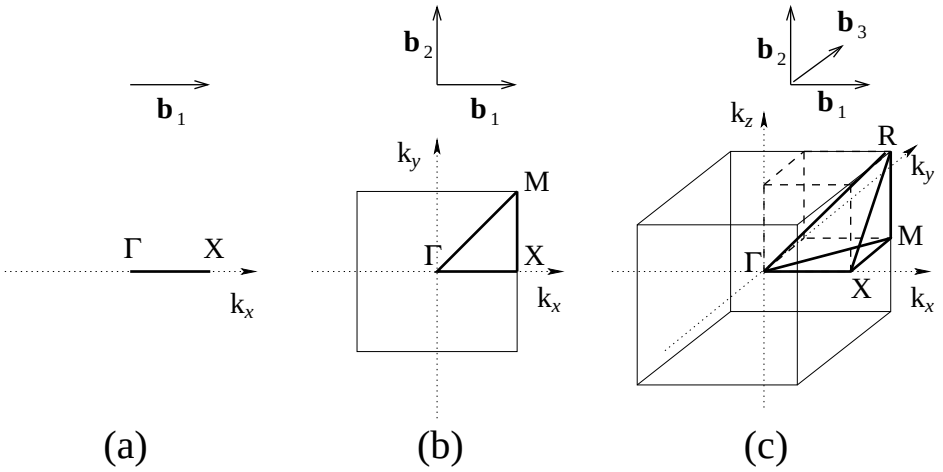

Figure 1.1: Brillouin zones for the photonic crystal structures of Fig. 1: (a) 1D, (b) 2D and (c) 3D. Bold lines mark the irreducible Brillouin zones, while $\{\mathbf{b}_i\}$ represent the set of primitive vectors for generating the dual space $\mathbb{G}$. The main symmetry points are also indicated.

where $\sigma = \sigma(\mathbf{k}+\mathbf{G})$ labels the two possible independent polarization states of each partial wave, and of course it depends on $\mathbf{k}+\mathbf{G}$ through the condition $(\mathbf{k}+\mathbf{G})\cdot\hat{\mathbf{e}}_{\mathbf{k}+\mathbf{G},\sigma} = 0$, $\hat{\mathbf{e}}_{\mathbf{k}+\mathbf{G},\sigma}$ being the normalized polarization vector. This additional degree of freedom comes from the vectorial nature of the field, whose three components are related by the divergence equation. Thus, only two components are really independent, and for each couple of quantum numbers $\mathbf{k}, n$ there are two independent solutions with different polarizations. In order to implement the calculation numerically, the sum over the reciprocal lattice vectors must be truncated to a maximum value $\mathbf{G} \in \mathbb{G}$ so that $|\mathbf{G}| < G_{\max}$. This way Eq. 1.15 becomes a finite expansion. The truncation of the sum is the main approximation of the method. The master equation 1.13 has to be rewritten in Fourier space by calculating the matrix elements of the "hamiltonian" $\hat{\mathbf{O}}$ on the basis of plane waves. By expanding the periodic dielectric function in Fourier series

$$\epsilon(\mathbf{r}) = \sum_{\mathbf{G}\in\mathbb{G}} \epsilon(\mathbf{G}) e^{i\mathbf{G}\cdot\mathbf{r}}, \tag{1.16}$$

it is easy to obtain the following linear eigenvalue equation

$$\sum_{\mathbf{G}',\sigma'} \mathcal{H}^{\sigma,\sigma'}_{\mathbf{G},\mathbf{G}'} c_{\mathbf{k}\sigma'}(\mathbf{G}') = \frac{\omega^2_{\mathbf{k}}}{c^2} c_{\mathbf{k}\sigma}(\mathbf{G}) \tag{1.17}$$

where the "hamiltonian" matrix elements in Fourier space are given by

$$\mathcal{H}^{\sigma,\sigma'}_{\mathbf{G},\mathbf{G}'} = |\mathbf{k}+\mathbf{G}||\mathbf{k}+\mathbf{G}'|\eta(\mathbf{G}-\mathbf{G}') \begin{pmatrix} \hat{\mathbf{e}}_{\sigma_2}\cdot\hat{\mathbf{e}}_{\sigma'_2} & -\hat{\mathbf{e}}_{\sigma_2}\cdot\hat{\mathbf{e}}_{\sigma'_1} \\ -\hat{\mathbf{e}}_{\sigma_1}\cdot\hat{\mathbf{e}}_{\sigma'_2} & \hat{\mathbf{e}}_{\sigma_1}\cdot\hat{\mathbf{e}}_{\sigma'_1} \end{pmatrix} \tag{1.18}$$

and the matrix $\eta(\mathbf{G}-\mathbf{G}') = \epsilon^{-1}(\mathbf{G}-\mathbf{G}')$ is the inverse of the dielectric function Fourier transform

$$\epsilon(\mathbf{G}-\mathbf{G}') = \frac{1}{A_c}\int_{A_c} \epsilon(\mathbf{r}) e^{i(\mathbf{G}-\mathbf{G}')\cdot\mathbf{r}} \mathrm{d}\mathbf{r}, \tag{1.19}$$

and the integral is evaluated over the space A_c occupied by the unit cell in the direct lattice. The latter can be easily calculated from the primitive lattice vectors $\{\mathbf{a}_i\}$[2]. It is worth noting that for a 3D photonic crystal Eq. 1.17 has to be solved considering both polarization degrees of freedom, because they are coupled by $\epsilon^{-1}(\mathbf{G}-\mathbf{G}')$. In the next paragraph it will be shown that for a 2D photonic crystal, assuming only in-plane propagation, the two polarizations decouple giving rise to two scalar equations.

The solution of Eq. 1.17 can be found numerically, yielding the determination of the photonic band structure $\omega_n(\mathbf{k})$ and its eigenvectors through the coefficients $c_{\mathbf{k}\sigma}(\mathbf{G})$ of the Fourier expansion. The matrix 1.18 has dimensions $2N \times 2N$, where N is the number of reciprocal space vectors $\mathbf{G}$ so that $|\mathbf{G}| < G_{\max}$. It evident that likewise the operator $\hat{\mathbf{O}}$ the matrix $[\mathcal{H}]$ is hermitian with non-negative real eigenvalues. For a study on the convergence properties of the PWE method we refer to [56], in which mathematical foundations are given for the faster convergence of the so called *inverse rule*, or also *Ho-Chan-Soukoulis* (HCS) method since its first application in Ref. [57]. Basically, this method consists in calculating Eq. 1.19 for the given lattice and basis, and then inverting numerically the dielectric function matrix in order to construct the hamiltonian 1.18. This is the method that has been used in the numerical implementation of PWE throughout the present work.

Two-dimensional photonic crystals

As pointed out in this Section, a 2D photonic crystal is a meta-material whose dielectric function presents periodicity in a horizontal plane and is uniform in the direction perpendicular to this plane, as schematically depicted in Fig. 1. The PWE method is particularly suited for calculating the photonic band structure of 2D photonic crystals, because good convergence properties are obtained by using the HCS method and CPU time required for a numerical calculation of a full photonic band structure is very low. Since the periodicity

[2]In fact, the unit cell length, area or volume is given by: (i) $|\mathbf{a}_1|$ for 1D, (ii) $|\mathbf{a}_1 \times \mathbf{a}_2|$ for 2D, and (iii) $|\mathbf{a}_1 \cdot (\mathbf{a}_2 \times \mathbf{a}_3)|$ for 3D photonic crystals, respectively.

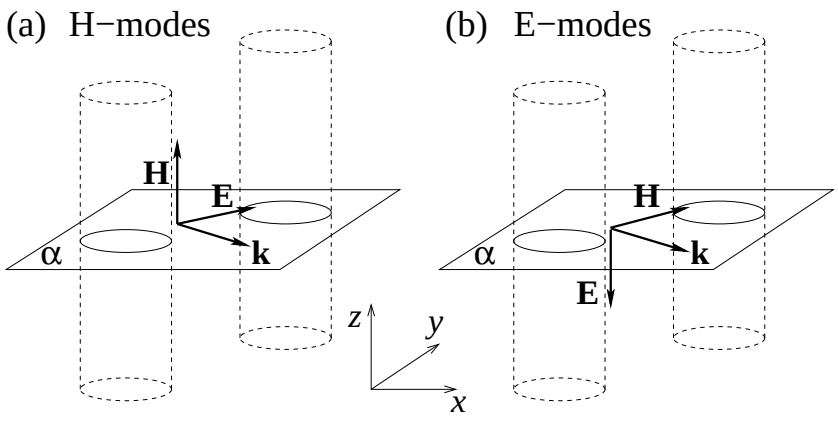

Figure 1.2: (a) Even and (b) odd modes with respect to a generic horizontal symmetry plane α. Considering in-plane propagation in a 1D or 2D photonic crystal, eigensolutions can be decomposed in (a) H-modes ($\mathbf{H} \parallel \hat{\mathbf{z}}$) and (b) E-modes ($\mathbf{E} \parallel \hat{\mathbf{z}}$).

is in 2 dimensions, the dielectric function is $\epsilon = \epsilon(x, y)$ giving rise to two-dimensional lattices both in direct and reciprocal spaces, with two primitive vectors. The construction of primitive vectors in reciprocal space is done by using the simple rule given 1.14. Here we do not specify to any particular lattice; for the square lattice we refer to Fig. 1.1, while the triangular lattice of air holes will be treated in Chapter 3. The formalism is restricted to in-plane propagation only, and thus $\mathbf{k} = (k_x, k_y, 0)$. In this case two different parities can be used to classify electromagnetic eigenmodes, schematically shown in Fig. 1.2, called E-modes and H-modes, respectively. By considering a horizontal plane $\alpha \parallel (x, y)$, for in-plane propagation and transversality conditions the photonic modes can be either even or odd with respect to mirror reflection through the plane α. Even modes have the magnetic field perpendicular to the plane ($\mathbf{H}$ is a pseudo-vector and doesn't change sign when reflected) and electric field lying in the plane, viceversa for odd modes ($\mathbf{E}$ is a vector)[3]. In brief, E-modes have field components (H_x, H_y, E_z) and H-modes (E_x, E_y, H_z), all the other components can be set to zero. Since for a crystal infinitely extended in the z-direction there are infinite mirror plane α parallel to (x, y), the fields have to be uniform with respect to z. Thus, the two polarization vectors are $\hat{\mathbf{e}}_{\sigma_1}(\mathbf{k} + \mathbf{G}) = (0, 0, 1)$ and $\hat{\mathbf{e}}_{\sigma_2}(\mathbf{k} + \mathbf{G}) = (e_x(\mathbf{k}+\mathbf{G}), e_y(\mathbf{k}+\mathbf{G}), 0)$, where $\hat{\mathbf{e}}_{\mathbf{k}+\mathbf{G},\sigma} \cdot (\mathbf{k}+\mathbf{G}) = 0$. These two polarizations are evidently independent, that is $\hat{\mathbf{e}}_{\mathbf{k}+\mathbf{G},\sigma_1} \cdot \hat{\mathbf{e}}_{\mathbf{k}+\mathbf{G}',\sigma_2} = 0 \ \forall \ \mathbf{G}, \mathbf{G}' \in \mathbb{G}$. It is

[3]In the literature these modes are also defined TE (H-modes) and TM (E-modes).

worth reminding that the in-plane fields are not necessarily orthogonal to the corresponding Bloch wave vector in the photonic crystal structure.

In conclusion, for in-plane propagation in a 2D photonic crystal σ is a "good quantum number" to classify photonic eigenmodes: $\omega_{n,\sigma}(\mathbf{k})$ and $\mathbf{H}_{\mathbf{k},n,\sigma}(\mathbf{r})$. If we label with σ_1 the H-modes and with σ_2 the E-modes, from Eqs. 1.17 and 1.18 we easily obtain that the master equation is split into two independent equations [58]

$$\sum_{\mathbf{G}'}(\mathbf{k}+\mathbf{G})\cdot(\mathbf{k}+\mathbf{G}')\,\eta(\mathbf{G}-\mathbf{G}')\,c_{\mathbf{k}\sigma_1}(\mathbf{G}')=\frac{\omega_{\mathbf{k}}^2}{c^2}\,c_{\mathbf{k}\sigma_1}(\mathbf{G}),\qquad \mathrm{H-modes} \tag{1.20}$$

$$\sum_{\mathbf{G}'}|\mathbf{k}+\mathbf{G}||\mathbf{k}+\mathbf{G}'|\,\eta(\mathbf{G}-\mathbf{G}')\,c_{\mathbf{k}\sigma_2}(\mathbf{G}')=\frac{\omega_{\mathbf{k}}^2}{c^2}\,c_{\mathbf{k}\sigma_2}(\mathbf{G}),\qquad \mathrm{E-modes.} \tag{1.21}$$

The solution of Eqs. 1.20 and 1.21 independently allows to reduce the dimension of the eigenvalue problem to $N\times N$ matrices.

1.1.2 Eigenmodes in planar dielectric waveguides

Planar dielectric waveguides are commonly made of thin slabs of high index contrast material, called the *core* layer, standing between low index semi-infinite media, called *claddings*. If the thickness of the core layer is of the order of the wavelength of the electromagnetic radiation, interesting confinement effects influence the photonic dispersion and the propagation properties on light beams. The purpose of the present Section is to show how the solution of Maxwell's equations in these systems leads to the definition of different photonic eigenmodes.

We start from the generic Maxwell's equations in a homogeneous medium with magnetic permeability μ and dielectric constant ϵ

$$\nabla\cdot\mathbf{E}=0,\qquad \nabla\times\mathbf{E}=-\frac{1}{c}\frac{\partial\mathbf{B}}{\partial t}, \tag{1.22}$$

$$\nabla\cdot\mathbf{B}=0,\qquad \nabla\times\mathbf{B}=\frac{\mu\epsilon}{c}\frac{\partial\mathbf{E}}{\partial t}. \tag{1.23}$$

By combining the two curl equations we obtain

$$\nabla\times\nabla\times\mathbf{E}=-\frac{\mu\epsilon}{c^2}\frac{\partial^2\mathbf{E}}{\partial t^2},\qquad \nabla\times\nabla\times\mathbf{B}=-\frac{\mu\epsilon}{c^2}\frac{\partial^2\mathbf{B}}{\partial t^2}. \tag{1.24}$$

Recalling the relation $\nabla\times\nabla\times\mathbf{a}=\nabla(\nabla\cdot\mathbf{a})-\nabla^2\mathbf{a}$ for the generic vector $\mathbf{a}$ and assuming harmonic temporal dependence, Eq. 1.5, one gets that the generic field component Ψ satisfies the Helmholtz equation

$$\left(\nabla^2+\mu\epsilon\frac{\omega^2}{c^2}\right)\Psi(\mathbf{r})=0. \tag{1.25}$$

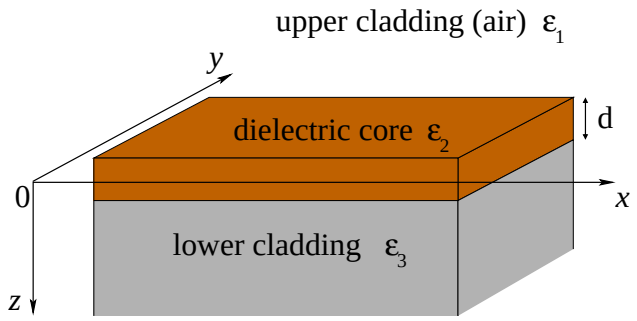

Figure 1.3: Schematic illustration of a uniform dielectric slab of dielectric constant $\epsilon_2 = n_2^2$ between low index claddings. The reference frame used in this work is indicated.

Now, we want to find the eigenmodes of Eq. 1.25 for the system represented in Fig. 1.3. We consider a planar waveguide of thickness d made of a non-absorbing dielectric material with refractive index n_2 and dielectric constant $\epsilon_2 = n_2^2$, both real. The core layer is sandwiched between non-absorbing materials of lower refractive indices n_1 and n_3 for the upper and lower claddings, respectively. The (x, y) plane is chosen to lie in the middle of the core layer and the vertical axis is directed from the upper to the lower cladding, thus the planes of discontinuity for the dielectric constant $\epsilon = \epsilon(z)$ are $z_1 = -d/2$ and $z_2 = +d/2$, respectively. We assume, in general, the following relations between the dielectric constants in the three layers: $\epsilon_2 > \epsilon_3 > \epsilon_1$. Under proper conditions, light can be confined to propagate in the dielectric slab. Boundary conditions at core/claddings interfaces lead to wave vector quantization along z. The analogy with the typical quantum mechanical problem of a particle in a one-dimensional box is clear. Anyway, since the continuous translational symmetry in the plane (x, y) is preserved, the in-plane momentum is a good quantum number and can be used to classify the eigensolutions. For every fixed $\mathbf{k}_\parallel = (k_x, k_y, 0)$ we expect a discrete spectrum of photonic modes coming from the quantization of k_z. The corresponding photonic modes are truly guided waves. Each component of the fields $\mathbf{E}$ and $\mathbf{H}$ has the following functional form[4]

$$\Psi(\mathbf{r}) = \Psi(z)e^{i(k_x x - \omega t)}, \tag{1.26}$$

where the fields are assumed uniform in y. Equation 1.25 thus becomes

$$\frac{\partial^2 \Psi(z)}{\partial z^2} + \left(\epsilon(z)\frac{\omega^2}{c^2} - k_x^2\right)\Psi(z) = 0. \tag{1.27}$$

[4]We assume, without loss of generality, propagation along x, and non-magnetic materials, that is $\mu = 1$ and $\mathbf{B} = \mathbf{H}$.

Before embarking in the formal solution of Eq. 1.25, we may learn a great deal about the physical nature of possible eigenmodes by simple arguments. The general solution of this eigenvalue problem can be given, in each uniform layer, in terms of the propagation constant defined by

$$\beta_j^2 = \epsilon_j \frac{\omega^2}{c^2} - k_x^2 \,, \quad j = 1, 2, 3. \tag{1.28}$$

We write, for the generic field component Ψ, the following general solution

$$\Psi(z) = \begin{cases} \psi_1^+ e^{i\beta_1(z+d/2)} + \psi_1^- e^{-i\beta_1(z+d/2)} & \text{for } z < -d/2 \\ \psi_2^+ e^{i\beta_2 z} + \psi_2^- e^{-i\beta_2 z} & \text{for } |z| < d/2 \\ \psi_3^+ e^{i\beta_3(z-d/2)} + \psi_3^- e^{-i\beta_3(z-d/2)} & \text{for } z > +d/2 \end{cases} . \tag{1.29}$$

It is worth noting that, from a "ray optics" point of view, guided modes correspond to a total internal reflection mechanism, as it can be argued from Fig. 1.4a. From Snell's law of refraction between a high index medium and a low index one

$$n_2 \sin\theta_2 = n_j \sin\theta_j \,, \qquad n_2 > n_j \quad \text{with} \quad (j = 1, 3) \tag{1.30}$$

a critical internal angle can be defined

$$\theta = \arcsin\left(\frac{n_j}{n_2}\right), \tag{1.31}$$

such that propagating beam angle of refraction is 90° and thus light is totally reflected within the core layer. Equation 1.29 allows to divide the (k_x, ω) plane into different regions corresponding to the values of β_j, as schematically shown in Fig. 1.4b. It is easy to understand that according to the real or imaginary nature of β_j, the corresponding solutions of Eq. 1.27 can be oscillating, evanescent, or divergent. In particular, guided mode field components are oscillating within the core layer and evanescent in the claddings, and are discretized by the confining potential along z; on the other hand, it is clear that infinite solutions exist such that their field components form a continuum set of states whose behavior is oscillating also in the claddings. The latter are called radiative (or leaky) modes, as they radiate electromagnetic energy far away from the guiding layer [4]. When the fields increase without bounds at least on one side away from the waveguide, then the solution is not physically realizable and does not correspond to a real wave, so that no modes exist in that region of (k_x, ω) plane. The various regions are separated by the dispersions of light in the different homogeneous media, defined by the three *light lines* $\omega = ck_x/\sqrt{\epsilon_1}$, $\omega = ck_x/\sqrt{\epsilon_3}$, and $\omega = ck_x/\sqrt{\epsilon_2}$ from top to bottom. The next step, thus, is to specialize Eq. 1.29 to guided

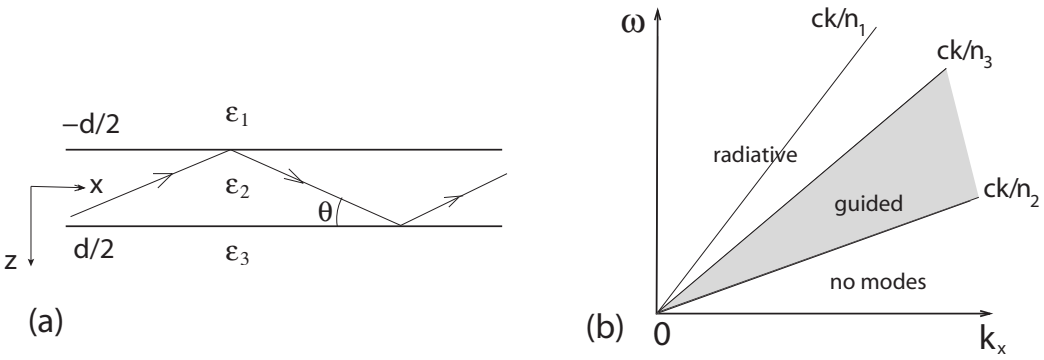

Figure 1.4: (a) A uniform planar waveguide with dielectric discontinuity along z. (b) Nature of photonic eigenmodes for the uniform slab in the $(\mathbf{k}, \omega)$ plane. The spectrum is discretized in the guided modes region, which is displayed by the light grey area. The boundaries of the different regions are called *light lines*.

mode solutions, in order to find the photonic dispersion of guided modes corresponding to the shaded region of the (k_x, ω) plane in Fig. 1.4b.

The presence of an incidence plane, which is represented by (x, z) in our reference frame, allows for a distinction of possible solutions, according to their parity with respect to reflection through this plane. Thus, photonic eignemodes are classified as odd (transverse electric field, TE modes) or even (transverse magnetic field, TM modes) with respect to the symmetry operation $\hat{\sigma}_{xz}$; TE modes have non-vanishing field components (H_x, E_y, H_z), while TM modes have only (E_x, H_y, E_z) components. The general solution, Eq. 1.29, can be specified to truly guided solutions by defining the real propagation constants in each layer

$$\chi_1 = \left(k_x^2 - \epsilon_1 \frac{\omega^2}{c^2}\right)^{1/2}, \quad \beta = \left(\epsilon_2 \frac{\omega^2}{c^2} - k_x^2\right)^{1/2}, \quad \chi_3 = \left(k_x^2 - \epsilon_3 \frac{\omega^2}{c^2}\right)^{1/2}. \quad (1.32)$$

The field components, evanescent in the claddings and oscillating in the core layer, are given by

$$\text{TE} \Rightarrow \quad E_y(z) = \begin{cases} E_1^- e^{\chi_1 (z+d/2)} & \text{for } z < -d/2 \\ E_2^+ e^{i\beta z} + E_2^- e^{-i\beta z} & \text{for } |z| < d/2 \\ E_3^+ e^{-\chi_3 (z-d/2)} & \text{for } z > d/2 \end{cases} \quad (1.33)$$

for TE modes and by

$$\text{TM} \Rightarrow \quad H_y(z) = \begin{cases} H_1^- e^{\chi_1 (z+d/2)} & \text{for } z < -d/2 \\ H_2^+ e^{i\beta z} + H_2^- e^{-i\beta z} & \text{for } |z| < d/2 \\ H_3^+ e^{-\chi_3 (z-d/2)} & \text{for } z > d/2 \end{cases} \quad (1.34)$$

for TM modes, respectively. In order to relate the field amplitudes at each interface, we adopt the transfer matrix formalism. Interface matrices for TE and TM modes are different, owing to the different continuity conditions for **E** and **H** fields. It can be shown that transfer matrices divide into propagation T-matrices and interface T-matrices. Referring to the generic scheme of Fig. 1.5, these matrices can be written as[5]

$$T_2 = \begin{pmatrix} e^{ik_{z2}d} & 0 \\ 0 & e^{-ik_{z2}d} \end{pmatrix}, \tag{1.35}$$

$$T_{i\to j}^{(TE)} = \frac{1}{2k_{zj}} \begin{pmatrix} k_{zi}+k_{zj} & k_{zj}-k_{zi} \\ k_{zj}-k_{zi} & k_{zi}+k_{zj} \end{pmatrix}, \tag{1.36}$$

$$T_{i\to j}^{(TM)} = \frac{1}{2\sqrt{\epsilon_i}\sqrt{\epsilon_j}k_{zj}} \begin{pmatrix} \epsilon_j k_{zi}+\epsilon_i k_{zj} & \epsilon_j k_{zi}-\epsilon_i k_{zj} \\ \epsilon_j k_{zi}-\epsilon_i k_{zj} & \epsilon_j k_{zi}+\epsilon_i k_{zj} \end{pmatrix}, \tag{1.37}$$

where i can be 1 or 2 and correspondingly j should be 2 or 3. Specifying now these matrices to our problem, we have for the two polarizations

$$\text{TE} \Rightarrow \quad \begin{pmatrix} E_3^+ \\ 0 \end{pmatrix} = T_{2\to 3}^{(TE)} T_2(d) T_{1\to 2}^{(TE)} \begin{pmatrix} 0 \\ E_1^- \end{pmatrix}, \tag{1.38}$$

$$\text{TM} \Rightarrow \quad \begin{pmatrix} H_3^+ \\ 0 \end{pmatrix} = T_{2\to 3}^{(TM)} T_2(d) T_{1\to 2}^{(TM)} \begin{pmatrix} 0 \\ H_1^- \end{pmatrix}, \tag{1.39}$$

which, after some lengthy calculations and imposing the condition $\det(T_{\text{tot}}) = 0$, lead to the following secular equations for TE and TM guided modes, respectively[6]

$$\text{TE} \Rightarrow \quad \beta(\chi_1+\chi_3)\cos(\beta d) + (\chi_1\chi_3 - \beta^2)\sin(\beta d) = 0, \tag{1.40}$$

$$\text{TM} \Rightarrow \quad \frac{\beta}{\epsilon_2}\left(\frac{\chi_1}{\epsilon_1}+\frac{\chi_3}{\epsilon_3}\right)\cos(\beta d) + \left(\frac{\chi_1\chi_3}{\epsilon_1\epsilon_3} - \frac{\beta^2}{\epsilon_2^2}\right)\sin(\beta d) = 0. \tag{1.41}$$

It is evident that the zeros of Eqs. 1.40 and 1.41 have to be found numerically, for fixed k_x, in the frequency window $ck_x/n_2 < \omega < ck_x/n_3$. The solution yields a finite number of eigenfrequencies $\omega_n(k_x)$, corresponding to discretized values of k_{z2}. The field patterns can be straightforwardly determined by giving the initial amplitudes, E_1^- and H_1^-, respectively. Assuming normalized fields, these amplitudes can be set to unity. Once obtained one of the fields, e.g. the magnetic field for TM modes, the other can be recast by applying Maxwell's equations, e.g. Eq. 1.8. The number of confined modes for a

[5]For a straightforward derivation of these transfer matrices, Maxwell boundary conditions between the fields at the dielectric interfaces must be applied.

[6]In order to get the secular equations, one has to impose that $k_{z1} = i\chi_1$, $k_{z2} = \beta$, and $k_{z3} = i\chi_3$.

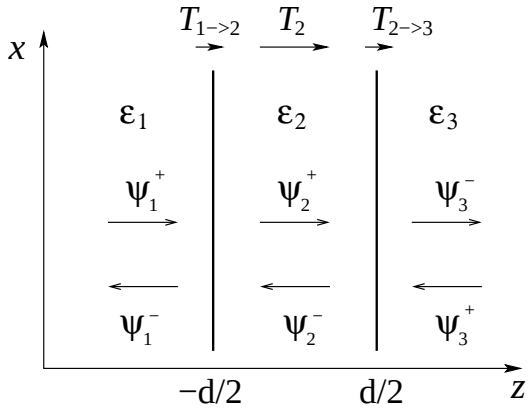

Figure 1.5: Scheme of a three layer structure related by transfer matrices. The schematic illustration refers to the structure of Fig. 1.3.

given k_x depends on the core thickness d, the thicker is the slab the more guided modes are present in the solutions of Eqs. 1.40 and 1.41. It is worth noting that all the guided modes of an asymmetric planar waveguide have finite cut-off frequencies, which can be understood by the expression of these frequencies as a function of the main structural parameters. In fact, an analytical formula can be obtained by imposing the cut-off condition, i.e. $\chi_3 = 0 \Rightarrow k_x^2 = \epsilon_3 \omega^2/c^2$, in the secular equations. It is straightforward to get, respectively for TE and TM modes,

$$\omega_{\text{c.o.}}^{(TE)} = \frac{\pi c}{d\sqrt{\epsilon_2 - \epsilon_1}} \left[m + \frac{1}{\pi} \arctan\left(\frac{\sqrt{\epsilon_3 - \epsilon_1}}{\sqrt{\epsilon_2 - \epsilon_3}} \right) \right] \tag{1.42}$$

$$\omega_{\text{c.o.}}^{(TM)} = \frac{\pi c}{d\sqrt{\epsilon_2 - \epsilon_1}} \left[m + \frac{1}{\pi} \arctan\left(\frac{\epsilon_2}{\epsilon_1} \frac{\sqrt{\epsilon_3 - \epsilon_1}}{\sqrt{\epsilon_2 - \epsilon_3}} \right) \right], \tag{1.43}$$

where $m = 0, 1, 2, ...$ labels the order of guided modes[7].

It is worth pointing out that in the particular case of a symmetric slab waveguide like, e.g., a suspended dielectric membrane (also called *air bridge*), the solution of the secular equation factorizes in two independent conditions. This is due to the symmetry operation with respect to the horizontal midplane of the slab, which allows to further classify the modes as even ($\sigma_{xy} = +1$) or odd ($\sigma_{xy} = -1$). By imposing $\epsilon_1 = \epsilon_3$ and $\chi_1 = \chi_2 = \chi$ in Eqs. 1.40 and 1.41 and after some trivial calculations, we obtain that the following characteristic equations have to be solved in order to find photonic

[7]These formulas coincide with previous analytical treatments of planar waveguides, which can be found in Ref. [4].

eigenmodes:

$$\text{TE even} \qquad \chi\cos(\beta d/2) - \beta\sin(\beta d/2) = 0, \tag{1.44}$$

$$\text{TE odd} \qquad \chi\sin(\beta d/2) + \beta\cos(\beta d/2) = 0 \tag{1.45}$$

for TE modes and

$$\text{TM even} \qquad \epsilon_2\chi\sin(\beta d/2) + \epsilon_1\beta\cos(\beta d/2) = 0, \tag{1.46}$$

$$\text{TM odd} \qquad \epsilon_2\chi\cos(\beta d/2) - \epsilon_1\beta\sin(\beta d/2) = 0 \tag{1.47}$$

for TM modes, respectively. One of the peculiarities of symmetric waveguides as compared to asymmetric ones is that the lowest order TE and TM modes have zero cut-off frequency, that is their dispersion starts as the one of an effective homogeneous medium. Moreover, it can be easily seen that TE and TM higher-order modes have degenerate cut-off frequencies. From Eqs. 1.42 and 1.43, with $\epsilon_1 = \epsilon_3$, the analytical formula for all-order cut-off frequencies in a symmetric dielectric slab is

$$\omega_{\text{c.o.}}^{(TE)} = \omega_{\text{c.o.}}^{(TM)} = \frac{m\pi c}{d\sqrt{\epsilon_2 - \epsilon_1}} \tag{1.48}$$

with $m = 0, 1, 2, ...$ as for the asymmetric waveguide. Fundamental TE and TM modes have zero cut-off frequency for a symmetric planar waveguide.

The dispersion of guided photonic modes has been experimentally measured in a Silicon (Si) planar waveguide on a Silicon dioxide (SiO_2) cladding. This system is commonly known as Silicon-on-Insulator (SOI). SOI wafers with $d = 260$ nm Si layer on a 1 μm SiO_2 were fabricated by SOITEC, and measured with an experimental technique known as Attenuated Total Reflectance (ATR) at the optical spectroscopy laboratory of the Department of physics "Alessandro Volta," University of Pavia, Italy. A schematic illustration of the kinematics of an ATR experiment is shown in Fig. 1.6a. An incident beam of polarized (TE or TM) light is coupled to evanescent modes supported by the slab waveguide through a ZnSe prism[8]. The conservation of in-plane momentum, related to angle of incidence, allows to observe pronounced dips in the angle-resolved ATR spectrum. The positions of the dips mark some points in the $(\mathbf{k}_\parallel, E)$ plane, allowing for a direct determination of guided mode dispersion (see App. A). The results of these measurements are plotted in Fig. 1.6b, with closed (open) points for TE (TM) incident light.

To compare experimental data with theoretical calculations on a wide energy range, we solved Eqs. 1.40 and 1.41 by using frequency dependent dielectric constants ϵ_{Si} and ϵ_{SiO_2}. Secular equations are solved self-consistently: at each wave vector k_x we determine the frequency interval $[\omega_{\text{low}}, \omega_{\text{up}}]$, with ω_{low}

[8]Details concerning the ATR set-up can be found in Ref. [53].

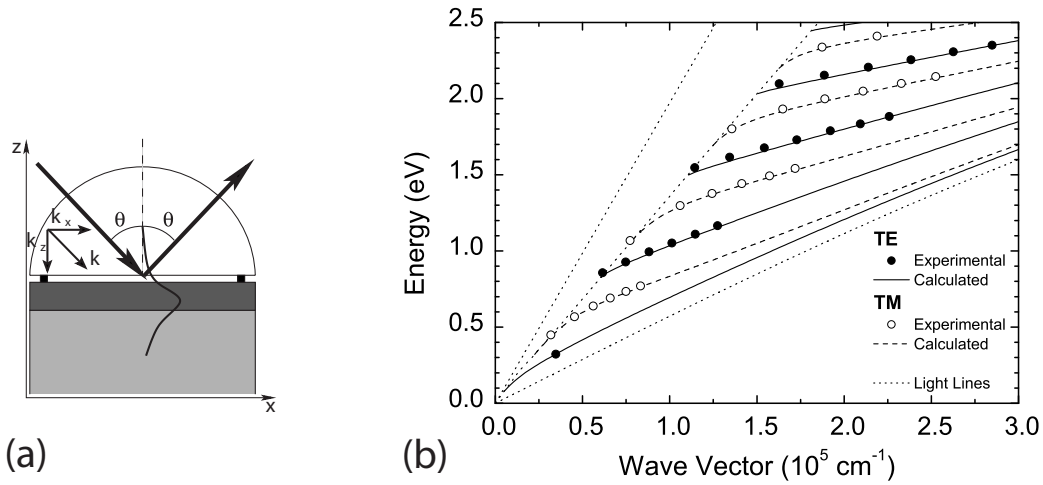

Figure 1.6: (a) Schematic illustration of an Attenuated Total Reflectance experiment. The semi-spherical prism is made of a material with intermediate refractive index between air and the core layer. (b) Experimentally determined dispersions and theoretical calculations (with frequency dependent dielectric constants) of guided modes in a 260 nm thick Silicon slab grown on a Silicon dioxide substrate. Both TE (closed circles and full lines) and TM (open circles and dashed lines) modes are exited in a ATR experiment with polarized incoming beam. Experimental points, extracted from ATR spectra (not shown here), are a courtesy of M. Galli and D. Bajoni.

lying on the Si light line and $\omega_{\rm up}$ on the SiO_2 light line, over which the zeros of Eqs. 1.40 and 1.41 are found. The frequencies $\omega_{\rm low}$ and $\omega_{\rm up}$ are calculated iteratively through the relation $\omega_{\rm low} = ck_x/n_{\rm Si}(\omega_{\rm low})$ and $\omega_{\rm up} = ck_x/n_{\rm SiO_2}(\omega_{\rm up})$. Real dielectric constants of Si and SiO_2 as a function of frequency are taken from input files (courtesy of M. Patrini). Finally, the solution of Eqs. 1.40 and 1.41 with energy dispersive dielectric constants allows to determine the exact dispersion of guided photonic modes, $\omega = \omega_{\alpha,\sigma}(k_x)$, where α labels the order of the confined solution and σ its polarization. The results, shown in Fig. 1.6b with lines (full for TE, dashed for TM), are in excellent agreement with experimental points extracted from angle-resolved ATR spectra. The Si, SiO_2 and air light lines are also plotted for clarity. These light lines are actually not straight lines, because of the energy dispersion of Si and SiO_2 refractive indices. It can be noticed that excitation of photonic modes via ATR measurements is possible only up to the crossing of guided modes with the lower cladding light line. It is important to stress that the close agreement between theory and experiment is the result of the iterative procedure

for solving the characteristic equations with frequency dispersion of refractive indices, owing to the large energy range (from 0.2 to 2.5 eV) of spectral analysis. This is, to the best of our knowledge, the first complete determination of guided modes in SOI planar waveguides, which also serves as an important proof of the theory.

1.2 Theory of photonic crystal slabs

Photonic crystals embedded in planar waveguides, also known as *photonic crystal slabs*, allow for a full three dimensional control of light. They exploit the considerable freedom in designing photonic structures (periodic or containing defects) given by the development of sub-micrometer size lithography and etching processes, besides the confinement properties (see last paragraph) of high refractive index contrast waveguides. A schematic picture of a photonic crystal slab is given in Fig. 1.7a. The investigation of these systems has been greatly improved in recent years, also because the fabrication of good quality three-dimensional photonic crystals is still a challenge, while in many cases the fabrication of photonic crystal slabs takes great advantages of knowhow coming from current opto-electronic industry. For these reasons, as already pointed out in the introductory notes, they are promising systems for future applications as building blocks of all-optical circuits.

Electromagnetic eigenmodes in dielectric slabs with a periodic pattern have notable differences as compared to the ideal reference systems (i.e., not waveguide-embedded), which are well known from the literature for the cases of both 1D [4, 5] and 2D [5] periodicity. A most important issue is the *light-line problem*: only photonic modes which lie below the light line of the cladding material (or materials, if the waveguide is asymmetric) are truly guided and stationary, while those lying above the light line in the first Brillouin zone are coupled to leaky waveguide modes and are subject to intrinsic radiative losses. The physical nature of different eigenmodes in photonic crystal slabs is schematically summarized in Fig. 1.7b. The dispersion diagram of the uniform planar waveguide is modified by the in-plane periodicity of dielectric constants, which introduces an irreducible Brillouin zone where guided modes are folded back and split, creating photonic band gaps. After the folding, some of the modes that should have been truly guided in the uniform slab fall above the cladding light line, and become quasi-guided.

These *quasi-guided modes* are actually resonances in a region of continuous energy spectrum[9], and for this reason they are more difficult to calculate

[9]This problem is similar, from a certain point of view, to the Fano resonances problem

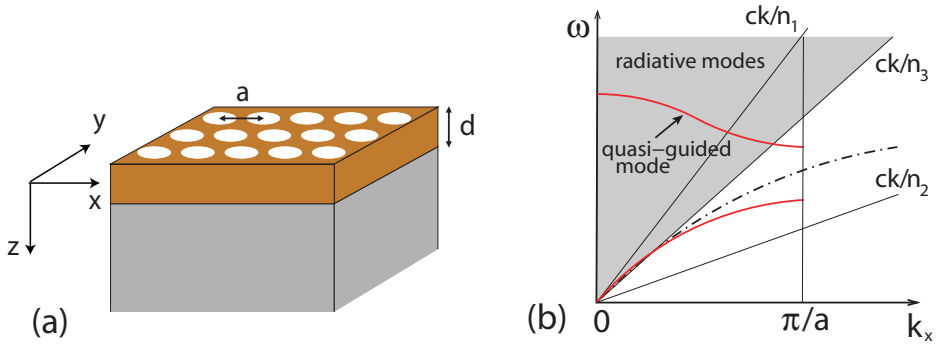

Figure 1.7: (a) Schematic drawing of a two-dimensional photonic crystal slab, made up of high refractive index core layer sandwiched between low index claddings and periodically patterned in the plane (x, y); (b) illustration of the nature of photonic eigenmodes in photonic crystal slabs.

than truly guided modes below the light line. Indeed, while the dispersion of truly guided modes in photonic crystal slabs can be obtained by a plane-wave expansion with a supercell in the vertical direction [28], the energies and especially the losses of quasi-guided modes are most commonly studied by exact numerical approaches such as Finite-Difference-Time-Domain (FDTD) [6], or scattering matrix calculations [31, 32]. The most common drawback of exact methods, however, is the computational effort required in order to treat realistic systems or to obtain convergent results. This prevents, in most cases, the systematic study of physical properties as a function, e.g., of structural parameters such as core thickness or air fraction, which would be useful for designing desired operating structures. No systematic studies of such kind have been found in literature for what concerns photonic crystal slabs, taking into account also the additional degrees of freedom introduced by quasi-guided modes.

In this Section a theory of photonic eigenmodes in photonic crystal slabs is presented. The present method has been first proposed a few years ago as a powerful tool to study dispersion characteristics [46] and intrinsic out-of-plane radiation losses [47, 48] in a variety of photonic crystal slab configurations, and it will be referred to henceforth as Guided-Mode Expansion method. The main advantages of this approximate approach are as follows. First of all it allows a three dimensional analysis of the electromagnetic problem, leading to reliable calculations of both truly guided and quasi-guided modes in photonic crystal slabs, while preserving a computational effort that

in Solid State Physics [59].

is close to the two-dimensional PWE method. This allows the fast although systematic study of many physical properties by varying a certain number of parameters (e.g. waveguide thickness, air fraction, dielectric contrast, and so on), which is highly desirable when designing new structures. Secondly, it can be straightforwardly extended to a perturbative theory of the coupling between guided and radiative modes, which leads to the calculation of intrinsic and extrinsic (i.e. disorder-induced) out-of-plane losses. Besides allowing the calculation of such fundamental quantities, the method yields a clear and easily understandable physical insight into this complicate electromagnetic problem. Finally, the direct calculation of eigenmodes in photonic crystal slabs allows to make studies on a more fundamental point of view, e.g. concerning the theoretical formulation of a quantum formalism for the radiation-matter interaction that will be presented in the last Chapter of this work.

1.2.1 The Guided-Mode Expansion method

The description of the method is given here in its most general formulation. It basically relies on a finite-basis expansion in order to transform the second-order equation for the magnetic field into a linear eigenvalue problem. The basis is chosen to consist of a set of eigenfunctions in which the planar and vertical dynamics are separated. For the planar dynamics the natural basis is given by the complete set of plane waves (see also Eq. 1.15), while the vertical dynamics is best described by the guided modes of an effective homogeneous waveguide where the dielectric constant of each layer is defined by the spatial average of the dielectric constant $\epsilon_j(x,y)$ (with $j = 1,2,3$ labelling the layers) over the photonic pattern. For this reason it is defined Guided-Mode Expansion (GME) method. The starting point is the second-order Maxwell equation for the magnetic field, which is rewritten here for convenience

$$\nabla \times \left[\frac{1}{\epsilon(\mathbf{x},z)} \nabla \times \mathbf{H} \right] = \frac{\omega^2}{c^2} \mathbf{H}, \tag{1.49}$$

where $\mathbf{x} = (x,y)$ is the in-plane coordinate vector. Generally speaking, the implementation of GME method is not much different from the PWE. Equation 1.49 can be formulated as a linear eigenvalue problem in Fourier space (like Eq. 1.17), after expanding the field on the chosen set of basis states. For each wave vector $\mathbf{k}$ within the irreducible Brillouin zone of the

in-plane periodic lattice[10], the magnetic field is expanded as

$$\mathbf{H}_{\mathbf{k}}(\mathbf{r}) = \sum_{\mathbf{G}} \sum_{\alpha} c_{\mathbf{k},\alpha}(\mathbf{G}) \mathbf{H}_{\mathbf{k}+\mathbf{G},\alpha}(\mathbf{r}) = \sum_{\mathbf{G}} \sum_{\alpha} c_{\mathbf{k},\alpha}(\mathbf{G}) \hat{\mathbf{h}}_{\mathbf{k}+\mathbf{G},\alpha}(z) \mathrm{e}^{i(\mathbf{k}+\mathbf{G})\cdot\mathbf{x}}, \quad (1.50)$$

where $\mathbf{G} \in \mathbb{G}$ is a two-dimensional reciprocal lattice vector, the integer "quantum number" $\alpha = 1, 2, \ldots, \alpha_{\max}$ labels the guided mode order, $\mathbf{x} = (x, y)$ is the in-plane coordinate vector, and $\hat{\mathbf{h}}_{\alpha,\mathbf{k}+\mathbf{G}}(z)$ is a normalized envelope function representing the guided magnetic field of the effective waveguide, which has to be found from Eqs. 1.33 and 1.34 for TE and TM polarized partial waves, respectively.

The transfer matrix formalism outlined in Sec. 1.1.2 is used to find the coefficients of the fields for the guided modes; a generalized orthonormal set of reference vectors is defined for fixed in-plane wave vectors $\mathbf{k} + \mathbf{G}$

$$\left(\frac{\mathbf{k}+\mathbf{G}}{|\mathbf{k}+\mathbf{G}|}, \hat{\mathbf{e}}_{\mathbf{k}+\mathbf{G}}, \hat{\mathbf{z}} \right), \quad (1.51)$$

where $\hat{\mathbf{e}}_{\mathbf{k}+\mathbf{G}}$ is the in-plane polarization unit vector, such that $\hat{\mathbf{e}}_{\mathbf{k}+\mathbf{G}} = (e_{x,\mathbf{k}+\mathbf{G}}, e_{y,\mathbf{k}+\mathbf{G}}, 0)$ and $\hat{\mathbf{e}}_{\mathbf{k}+\mathbf{G}} \cdot (\mathbf{k}+\mathbf{G}) = 0$, while $\hat{\mathbf{z}} = (0, 0, 1)$. Then, the corresponding propagation constants of Eq. 1.32 are redefined as

$$\chi_1(\mathbf{k}+\mathbf{G}) = \left(|\mathbf{k}+\mathbf{G}|^2 - \epsilon_{\mathrm{eff}}^{(1)} \frac{\omega^2}{c^2} \right)^{1/2}, \quad (1.52)$$

$$\beta(\mathbf{k}+\mathbf{G}) = \left(\epsilon_{\mathrm{eff}}^{(2)} \frac{\omega^2}{c^2} - |\mathbf{k}+\mathbf{G}|^2 \right)^{1/2}, \quad (1.53)$$

$$\chi_3(\mathbf{k}+\mathbf{G}) = \left(|\mathbf{k}+\mathbf{G}|^2 - \epsilon_{\mathrm{eff}}^{(3)} \frac{\omega^2}{c^2} \right)^{1/2}. \quad (1.54)$$

For in-plane polarized modes (TE modes) we have to find the coefficients defined in Eq. 1.33 for the electric field, which is $\mathbf{E}_{\mathbf{k}+\mathbf{G}}^{(\mathrm{TE})} = E \hat{\mathbf{e}}_{\mathbf{k}+\mathbf{G}}$. This is done by using the transfer matrices 1.35 and 1.36 to relate the field coefficients in the various layers, where each layer is assumed to have effective dielectric constant $\epsilon_{\mathrm{eff}}^{(j)}$ $(j = 1, 2, 3)$. Because the general formalism is developed for the magnetic field, once the guided electric field profiles are obtained at fixed $\mathbf{k}+\mathbf{G}$ we have to recover the corresponding magnetic field coefficients, which can be done by exploiting Maxwell'equation (analogous to Eq. 1.8)

$$\mathbf{H}(\mathbf{r}) = -i \frac{c}{\omega} \nabla \times \mathbf{E}(\mathbf{r}). \quad (1.55)$$

[10]The construction of reciprocal lattice primitive vectors and of the irreducible Brillouin zone for the two-dimensional periodic lattice follows the general guidelines of Sec. 1.1.1.

The explicit form of Eq. 1.33 is given by

$$\hat{\mathbf{E}}_{\mathbf{g}}^{(\mathrm{TE})}(z) = \frac{1}{\sqrt{N}} i \left(\frac{\omega_{\mathbf{g}}}{c}\right) \hat{\mathbf{e}}_{\mathbf{g}} \begin{cases} B_{\mathbf{g}}^{(1)} e^{\chi_{\mathbf{g}}^{(1)}(z+d/2)} & \text{for } z < -d/2 \\ A_{\mathbf{g}}^{(2)} e^{i\beta_{\mathbf{g}} z} + B_{\mathbf{g}}^{(2)} e^{-i\beta_{\mathbf{g}} z} & \text{for } |z| < d/2 \\ A_{\mathbf{g}}^{(3)} e^{-\chi_{\mathbf{g}}^{(3)}(z-d/2)} & \text{for } z > d/2 \end{cases}, \tag{1.56}$$

from which, through Eq. 1.55, we obtain

$$\hat{\mathbf{h}}_{\mathbf{g}}^{(\mathrm{TE})}(z) = \frac{1}{\sqrt{N}} \begin{cases} B_{\mathbf{g}}^{(1)} e^{\chi_{\mathbf{g}}^{(1)}(z+d/2)} (-\chi_{\mathbf{g}}^{(1)} \hat{\mathbf{g}} + i|\mathbf{g}|\hat{\mathbf{z}}) \\ i\beta_{\mathbf{g}} \left(-A_{\mathbf{g}}^{(2)} e^{i\beta_{\mathbf{g}} z} + B_{\mathbf{g}}^{(2)} e^{-i\beta_{\mathbf{g}} z}\right) \hat{\mathbf{g}} + \\ \quad + i|\mathbf{g}| \left(A_{\mathbf{g}}^{(2)} e^{i\beta_{\mathbf{g}} z} + B_{\mathbf{g}}^{(2)} e^{-i\beta_{\mathbf{g}} z}\right) \hat{\mathbf{z}} \\ A_{\mathbf{g}}^{(3)} e^{-\chi_{\mathbf{g}}^{(3)}(z-d/2)} (\chi_{\mathbf{g}}^{(3)} \hat{\mathbf{g}} + i|\mathbf{g}|\hat{\mathbf{z}}) \end{cases}, \tag{1.57}$$

where we have indicated with $\hat{\mathbf{g}}$ the unitary vector $(\mathbf{k}+\mathbf{G})/|\mathbf{k}+\mathbf{G}|$ and by $\mathbf{g}$ the wave vector $\mathbf{k}+\mathbf{G}$, for convenience of notation. The normalization factor can be calculated as a function of coefficients B_1, A_2, B_2, A_3 from the condition

$$N = \int |\mathbf{H}(\mathbf{x}, z)|^2 \mathrm{d}\mathbf{x}\mathrm{d}z \tag{1.58}$$

For TM modes, the coefficients of the guided magnetic field can be found directly by applying the transfer matrices 1.35 and 1.37 to the expression

$$\hat{\mathbf{h}}_{\mathbf{g}}^{(\mathrm{TM})}(z) = \frac{1}{\sqrt{N}} \hat{\mathbf{e}}_{\mathbf{g}} \begin{cases} D_{\mathbf{g}}^{(1)} e^{\chi_{\mathbf{g}}^{(1)}(z+d/2)} & \text{for } z < -d/2 \\ C_{\mathbf{g}}^{(2)} e^{i\beta_{\mathbf{g}} z} + D_{\mathbf{g}}^{(2)} e^{-i\beta_{\mathbf{g}} z} & \text{for } |z| < d/2 \\ C_{\mathbf{g}}^{(3)} e^{-\chi_{\mathbf{g}}^{(3)}(z-d/2)} & \text{for } z > d/2 \end{cases}. \tag{1.59}$$

After the solution of the vertical problem that yields the guided modes of the effective waveguide, Eq. (1.49) can be transformed into a linear eigenvalue problem (for fixed $\mathbf{k}$)

$$\sum_{\mathbf{g}'} \sum_{\alpha'} \mathcal{H}_{\mathbf{g},\mathbf{g}'}^{\alpha,\alpha'} c_{\alpha'}(\mathbf{g}') = \frac{\omega^2}{c^2} c_{\alpha}(\mathbf{g}), \tag{1.60}$$

where the "hamiltonian" matrix $\mathcal{H}_{\mathbf{g},\mathbf{g}'}^{\alpha,\alpha'}$ is hermitian and its elements can be calculated explicitly by the general expression

$$\mathcal{H}_{\mathbf{g},\mathbf{g}'}^{\alpha,\alpha'} = \int \mathbf{H}_{\mathbf{g},\alpha}^{*}(\mathbf{r}) \cdot \left[\nabla \times \left(\frac{1}{\epsilon(\mathbf{r})} \nabla \times \mathbf{H}_{\mathbf{g}',\alpha'}(\mathbf{r})\right)\right] \mathrm{d}\mathbf{r}\,, \tag{1.61}$$

where $\mathbf{H}_{\mathbf{g},\alpha}(\mathbf{r})$ is one of the eigenfunctions of the expansion (Eq. 1.50); rearranging the vectorial products Eq. 1.61 becomes

$$\mathcal{H}_{\mathbf{g},\mathbf{g}'}^{\alpha,\alpha'} = \int \frac{1}{\epsilon(\mathbf{r})} \left[\nabla \times \left(\hat{\mathbf{h}}_{\mathbf{g},\alpha}^{*}(z) \mathrm{e}^{-i\mathbf{g}\cdot\mathbf{x}}\right)\right] \cdot \left[\nabla \times \left(\hat{\mathbf{h}}_{\mathbf{g}',\alpha'}(z) \mathrm{e}^{i\mathbf{g}'\cdot\mathbf{x}}\right)\right] \mathrm{d}\mathbf{r}\,. \tag{1.62}$$

It is worth pointing out that in a 2D photonic crystal slab there is no possibility to separate the two polarizations, which are coupled owing to the presence of the vertical degree of freedom. Thus the eigenmodes cannot be classified anymore as purely TE or TM. Both guided mode solutions have to be included in the expansion and taken into account when constructing the photonic hamiltonian matrix (Eq. 1.62)[11]. Thus, we introduce a new quantum number σ =TE/TM labelling the polarization.

The matrix elements of Eq. 1.62 can be expressed in terms of the inverse dielectric tensor in each layer $\eta_j(\mathbf{g},\mathbf{g}') = \epsilon_j^{-1}(\mathbf{G}-\mathbf{G}')$, by assuming the separability of $\epsilon(\mathbf{r})$ and calculating the 2D integral in the xy plane. In fact, assuming that $\epsilon^{-1}(\mathbf{x},z)$ can be factorized as

$$\epsilon^{-1}(\mathbf{x},z) = \begin{cases} \epsilon_1^{-1}(\mathbf{x}) & \text{for } z < -d/2 \\ \epsilon_2^{-1}(\mathbf{x}) & \text{for } |z| < d/2 \\ \epsilon_3^{-1}(\mathbf{x}) & \text{for } z > d/2 \end{cases}, \tag{1.63}$$

the curl functions in Eq. 1.62 are explicitly calculated from Eqs. 1.57 (which, through Eq. 1.8, is basically given by Eq. 1.56 multiplied by $-i\epsilon\omega/c$) and 1.59. Finally, we get a very compact form of the hermitian hamiltonian matrix which can be written as

$$\begin{aligned} \mathcal{H}^{\sigma,\sigma'}_{\mathbf{g},\mathbf{g}',\alpha,\alpha'} = \quad & \epsilon_1^{-1}(\mathbf{G}-\mathbf{G}') \int_{-\infty}^{-d/2} \mathrm{d}z\, F^{(1)\sigma,\sigma'}_{\mathbf{g},\mathbf{g}',\alpha,\alpha'}(z) + \\ & \epsilon_2^{-1}(\mathbf{G}-\mathbf{G}') \int_{-d/2}^{d/2} \mathrm{d}z\, F^{(2)\sigma,\sigma'}_{\mathbf{g},\mathbf{g}',\alpha,\alpha'}(z) + \\ & \epsilon_3^{-1}(\mathbf{G}-\mathbf{G}') \int_{d/2}^{+\infty} \mathrm{d}z\, F^{(3)\sigma,\sigma'}_{\mathbf{g},\mathbf{g}',\alpha,\alpha'}(z)\,, \end{aligned} \tag{1.64}$$

where the functions $F^{(j)}_{\{*\}}(z)$ are explicitly determined, after some lengthy calculations, in terms of guided modes coefficients $\{A,B\}$ and $\{C,D\}$, and the integrals in the various layers are easily performed analytically[12]. The matrix $\epsilon_j^{-1}(\mathbf{G}-\mathbf{G}')$ is the same quantity which appears in usual 2D plane-wave calculations and can be conveniently evaluated by HCS method, that is by a numerical inversion of the dielectric matrices $\epsilon_j(\mathbf{G}-\mathbf{G}')$ [57]. It is evident that the numerical implementation required by this method is not much different from usual band structure calculation of a 2D photonic crystal with the PWE method. Anyway, it is worth pointing out that the dimensions of the matrix can lead to a more time-consuming diagonalization process than

[11] This is like in a three dimensional photonic crystal, see Eqs. 1.17 and 1.18.

[12] The integrand functions are exponentially decaying in the claddings and oscillating in the core layer.

PWE calculations[13]. After the construction of Eq. 1.64 for the given lattice, the numerical diagonalization of this matrix yields the eigenvalues $\omega_n^\alpha(\mathbf{k})$ and the corresponding eigenvectors, given by the explicit determination of the expansion coefficients $c_{\mathbf{k},\alpha,\sigma}(\mathbf{G})$ of Eq. 1.50.

The main approximation of the present method is as follows: even if the guided modes of the effective waveguide represent an orthonormal set of states, the basis is not complete since the radiative modes are not included in the expansion. The energy spectrum thus obtained treats on the same footing both truly guided and quasi-guided photonic modes, but the latter must be intended actually as resonances in a continuum of radiative modes, with a finite lifetime. The coupling to radiative modes at all energies produces a second-order shift of the resonance energies: this effect (usually of the order of a few percent) is neglected in the present formulation. The error in the determination of mode frequencies is largest for larger air fractions. However, the most important effect is the first-order coupling to radiative modes at the same energy for modes that fall above the light line leading to a radiative decay, i.e., to an imaginary part of the energy, which can be calculated by time-dependent perturbation theory. This procedure, formally analogous to Fermi's Golden Rule in quantum mechanics, will be addressed in the next paragraph.

Other approximations made in this guided-mode expansion method are as follows. The effective dielectric constant of the homogeneous waveguide, which defines the basis of guided modes for the expansion, is a key parameter in this approach. We assume that each layer composing the planar waveguide is patterned with a periodic lattice of air regions in a dielectric (or oxide for the claddings) matrix. Throughout this work, the effective dielectric constant is taken as the spatial average defined by

$$\epsilon_{\text{eff}}^{(j)} = f_{\text{air}}\epsilon_{\text{air}} + (1 - f_{\text{air}})\epsilon_j \,, \tag{1.65}$$

where $j = 1, 2, 3$ labels upper cladding, core and lower cladding, f_{air} is the air fraction common to all layers, for both TE and TM polarizations, and ϵ_j is the dielectric constant of the higher refractive index materials in each layer. This definition is by no means unique. For one-dimensional lattices of stripes, however, Eq. 1.65 can be considered the exact definition of the effective dielectric constant for TE polarization and anyway when the electric field is perpendicular to the direction of periodicity [60]. For TM-polarized modes, which have electric field components along x and z, the situation is

[13]The dimension of Eq. 1.64 for fixed $\mathbf{k}$ is given, in general, by $2(\alpha \cdot N) \times 2(\alpha \cdot N)$, α being the number of guided modes and N the number of plane waves used in the basis set.

more complex[14]. It is known from the literature that the x component of the electric field is subject to an effective dielectric constant that is obtained from the inverse averaging rule [60]. Therefore a different choice of ϵ_{eff} in the patterned region could be suggested for TM modes. Choices of ϵ_{eff} differing from Eq. 1.65 do not lead to any appreciable change of the results above the mode cutoff, as we have verified, in the case of 1D systems. The frequency position of the cutoff does depend on the choice of ϵ_{eff}, especially for large air fractions, however a comparison with exact scattering matrix calculations [19, 46] shows that the average dielectric constant defined by Eq. 1.65 gives very good agreement with the frequencies and cutoff positions obtained from the exact calculations. It should also be noted that the electromagnetic field close to mode cutoff is mostly extended in the claddings, where the dielectric constants are homogeneous for the airbridge and SOI structures studied throughout the present work.

The number of reciprocal lattice vectors $\mathbf{G}$ is limited by a finite cut-off $G_{\max}$, like for usual plane-wave calculations [57] (see also Sec. 1.1.1), and in addition a restricted number of guided modes of the effective waveguide is kept in the expansion. For the calculations shown in this work, the number of plane waves in the basis set depends on the lattice considered, but it is usually taken to be < 37 for simply periodic 1D photonic crystal slabs and < 109 for 2D triangular lattices of air holes, which are generally sufficient for convergence with better than percent accuracy. It should be noted that these numbers are valid thanks to the implementation of HCS method for the diagonalization of the inverse dielectric matrices in each layer, which greatly improves convergence properties in the number of plane waves [56]. The number of guided modes in the expansion is usually taken to be $\leq \alpha_{\max} = 8$, but it depends on the core thickness (thinner slabs need less guided modes in the basis set). All these approximations are justified *a posteriori* by the close agreement of the calculated photonic frequencies with those obtained from reflectivity calculations made with the exact scattering-matrix method [44, 46].

As a final remark, we point out that the choice of the basis for the expansion makes the method particularly suited to study systems with a strong refractive index contrast between the core layer and the claddings. In particular, for suspended dielectric membranes or air/dielectric/oxide structures results obtained by the present approach can be considered reliable and accurate. Accuracy of the present method has not been completely checked

[14]It is known in the grating literature that the application of coupled-wave analysis to the case of TM polarization is more difficult and special methods are needed to stabilize numerical convergence, as discussed, e.g., in Ref. [61].

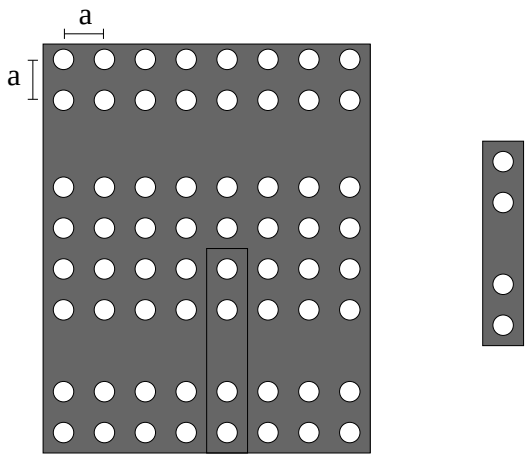

Figure 1.8: Linear defects in a square lattice of air holes. The elementary cell of the superlattice is shown on the right hand side.

for low index contrast symmetric structures, while for strongly asymmetric waveguide layers such as, e.g., air/GaAs/AlGaAs the results are often not accurate enough, owing to the limited number of guided modes that can be taken in the basis. In this work we restrict ourselves to study high index contrast structures.

The supercell method

As already mentioned, the GME approach allows for a quick extension to treat structures with more complicated patterns in the plane of the waveguide, such as point or linear defects embedded in an otherwise periodic lattice. If we want to study photonic eigenmodes, e.g., of a linear defect waveguide in a two-dimensional photonic crystal slab, we have to consider a periodic array of linear defects equally spaced (see Fig. 1.8). This artificially periodization of the system we want to study is called *supercell* method. Since the periodicity of the original lattice is preserved along one of the two main symmetry directions, the wave vector along that direction is conserved. A defect mode will be evanescent in the direction perpendicular to its propagation Bloch vector. Thus, if the supercell is sufficiently large, the guided modes of adjacent elementary cells will not overlap, and the resulting dispersion will be that of a single defect. In Fig. 1.8 a schematic picture of the elementary cell to be used in this case is displayed.

In order to expand the fields in the basis set of plane waves, we have to consider new primitive lattice vectors $\mathbf{a}_1$ and $\mathbf{a}_2$, which in this particular case

have the same directions of the original square lattice, but generally this is not verified. The most difficult task is to calculate the matrix $\epsilon_{\mathbf{G},\mathbf{G}'}$ for the superlattice. Looking, e.g., at the model structure of Fig. 1.8, we see that the dielectric function inside the supercell can be expressed as

$$\epsilon(\mathbf{x}) = \epsilon_{\text{diel}} + (\epsilon_{\text{air}} - \epsilon_{\text{diel}}) \sum_j \Theta(|\mathbf{x} - \mathbf{x}_j| - r) \quad \forall\, \mathbf{x} \in \text{ unit cell} \tag{1.66}$$

where ϵ_{diel} indicates the dielectric constant of the dark grey material, $\mathbf{x}_j$ are the positions of the holes within the unit cell, r is their radius, and $\Theta(x)$ is the step function[15]. The expression 1.66 is very convenient for computing the Fourier integral, Eq. 1.19. Indeed, the Fourier transform of the elementary cell of a composed lattice can be expressed as the Fourier transform of the cell of the square lattice multiplied by a structure factor that takes into account the diplacements $\mathbf{x}_j$, and it can be written as

$$\epsilon_{\mathbf{G},\mathbf{G}'} = \begin{cases} S(\mathbf{G} - \mathbf{G}')F_{\text{hole}}(\mathbf{G}) & \text{for} \mathbf{G} \neq \mathbf{G}' \\ f\epsilon_{\text{air}} + (1-f)\epsilon_{\text{diel}} & \text{for} \mathbf{G} = \mathbf{G}' \end{cases}, \tag{1.67}$$

where f is the supercell air fraction, $\mathbf{G}, \mathbf{G}'$ are reciprocal lattice vectors of the supercell lattice, S is the structure factor, and F_{hole} is the elementary Fourier transform. The structure factor is obtained by

$$S(\mathbf{G}) = \frac{A_c}{A} \sum_j e^{i\mathbf{G}\cdot\mathbf{x}_j}, \tag{1.68}$$

where A_c is the area of the square lattice unit cell, while A is the area of the supercell elementary cell. By using Eq. 1.67, we can thus solve the eigenvalue problem (Eq. 1.60), finally obtaining the correct dispersion relation for defect states. This method can be generalized, of course, to treat every patterned structure for which Eq. 1.67 can be calculated. Convergence in the number of plane waves used in the basis set has to be checked in each specific case.

1.2.2 Perturbative theory of radiation losses

In a photonic crystal slab, the periodic patterning in the plane of the waveguide leads to out-of-plane scattering of the guided Bloch waves. Such scattering mechanisms give rise, e.g., to well known features in transmission or reflection spectra of gratings and are generally known in the literature as

[15]The step function, or *Heaviside* function, is generally defined as

$$\Theta(x) = \begin{cases} 1 & x < 0 \\ 0 & x > 0 \end{cases}.$$

Wood's anomalies. Commonly, Wood's anomalies can be divided into two main classes: diffractive anomalies, caused by openings of new diffraction orders in the transmission or reflection spectra at a given angle, or waveguide anomalies, caused by the resonant coupling of an incoming light beam with surface or waveguide modes. From an historical viewpoint, diffractive anomalies were discovered in metallic gratings by Wood [62], and theoretically explained by Rayleigh [63], and are also known as *Rayleigh anomalies*. Waveguide anomalies, instead, are examples of a Fano resonance [59], where a discrete mode becomes a resonance owing to the coupling to a continuum of modes at the same energy. These losses are also called out-of-plane diffraction losses, because they physically correspond to diffraction precesses out of the waveguide plane for the Bloch waves propagating in the photonic crystal slab.

Recently, some theoretical approaches have been developed in order to treat the problem of these anomalies from a diffractive optics point of view, such as scattering matrix-based methods [31, 32], or from the exact solution of time-dependent Maxwell's equations through FDTD simulations [34, 36]. Here we tackle and solve this problem on a different theoretical basis. Coupling of waveguide eigenmodes to leaky modes of the effective waveguide is taken into account by time-dependent perturbation theory, which leads to an expression for the imaginary part of the mode frequency in terms of the photonic density of states at fixed in-plane wave vector [47][16]. This approach is very close to the formal description of Maxwell's equations as an hermitian eigenvalue problem that we have been using until now. Moreover, the procedure is formally analogous to Fermi's golden rule in quantum mechanics. Strictly speaking, we could address the present perturbative treatment of photonic eigenmodes in photonic crystal slabs as the *Photonic Golden Rule*. Basically, the imaginary part of mode frequencies can be associated to the finite lifetime of the corresponding photonic state, induced by the coupling to radiative modes. In this sense, applying the Photonic Golden Rule is very similar to the perturbative calculation of decay rates for electronic states induced by time-dependent perturbations. The main advantage of the present approach, besides the straightforward interpretation of the scattering mechanism of Bloch waves, is the possibility to include disorder-induced losses of truly guided modes within the perturbative hamiltonian, as it will be shown in the final part of the present paragraph.

[16]The perturbative treatment of the coupling to radiative modes is analogous to that introduced by Ochiai and Sakoda [42], however in the present method the dielectric modulation described by the tensor $\epsilon_{\mathbf{G},\mathbf{G}'}$ is treated exactly, thereby going beyond the nearly-free-photon approximation of Ref. [42].

The coupling between guided and radiative modes in the operator formalism can be expressed as

$$\Gamma_{\text{guid}\to\text{rad}} \propto \sum_{\text{rad}} |\langle \mathbf{H}_{\text{guid}} | \hat{\mathbf{O}}_p | \mathbf{H}_{\text{rad}} \rangle|^2 \,, \tag{1.69}$$

where $\mathbf{H}_{\text{guid}}$ is the solution of an eigenvalue problem of the form 1.10 with the matrix operator 1.64 and eigenvalues $\Omega = \omega^2/c^2$, while $\mathbf{H}_{\text{rad}}$ represents the continuum set of radiative modes at a given frequency for the effective homogeneous waveguide. The perturbation operator that couples guided to radiative modes is represented by $\hat{\mathbf{O}}_p = \epsilon^{-1}(\mathbf{r})$, because the scattering losses are caused by the non-separability of the spatially dependent dielectric constant. From Eq. 1.69 one gets the following expression for the imaginary part of mode eigenvalues [42]

$$-\text{Im}\left(\frac{\omega_{\mathbf{k}}^2}{c^2}\right) = \pi \, |\mathcal{H}_{\text{guid,rad}}|^2 \; \rho\left(\mathbf{k}; \frac{\omega_{\mathbf{k}}^2}{c^2}\right), \tag{1.70}$$

which is very similar to Fermi's Golden Rule[17]. Here $\rho(\mathbf{k}; \omega_{\mathbf{k}}^2/c^2)$ is the 1D density of photonic states at fixed $\mathbf{k}$, owing to the conservation of the in-plane wave vector, which has to be calculated for each polarization and (possibly) parity with respect to the horizontal midplane from the definition

$$\rho\left(\mathbf{k}; \frac{\omega_{\mathbf{k}}^2}{c^2}\right) = \sum_{k_z>0} \delta\left(\frac{\omega_{\mathbf{k}}^2}{c^2} - \frac{|\mathbf{k}|^2 + k_z^2}{\epsilon_{(\text{clad})}}\right). \tag{1.71}$$

When the waveguide is asymmetric (like in the case of the SOI structure), care must be taken to express the leaky modes in terms of outgoing states and to relate them to the respective state densities [64], which depend on the cladding considered. The state density of radiation modes has a divergence on the light line, which is a crucial issue for diffraction losses in a photonic crystal slab. The matrix element $\mathcal{H}_{\text{guid,rad}}$ is given by

$$\mathcal{H}_{\text{guid,rad}} = \int \frac{1}{\epsilon(\mathbf{r})} [\nabla \times \mathbf{H}^*_{\text{guid}}(\mathbf{r})] \cdot [\nabla \times \mathbf{H}_{\text{rad}}(\mathbf{r})] \, \mathrm{d}\mathbf{r} \,. \tag{1.72}$$

[17]The formal analogy with the expression of perturbative transition probability for an atom in a continuous radiation field should be noticed

$$\Gamma_{1\to2} = \frac{2\pi}{\hbar} |\langle 1|\hat{H}_I|2\rangle|^2 \rho(E_1 - E_2),$$

where $\hat{H}_I$ is the interaction hamiltonian and $\rho(E_1 - E_2)$ is the density of radiation states at the energy corresponding to the transition. This probability could be interpreted as a radiation damping of the emission or absorption lineshape of the transition, which can be also seen as an imaginary part of the mode frequency.

When the guided mode solution is expanded in terms of its eigenvectors like in Eq. 1.50, the matrix elements in Eq. 1.72 become

$$\mathcal{H}_{\text{guid,rad}} = \sum_{\mathbf{G},\sigma,\sigma'} c^{*}_{\mathbf{k},\alpha,\sigma}(\mathbf{G}) \mathcal{M}^{\sigma,\sigma'}_{\mathbf{G},\alpha}(\mathbf{k},\omega)\,, \tag{1.73}$$

where σ labels the polarization (TE or TM) state of the corresponding guided or radiation mode in the uniform planar slab. The procedure for the calculation of $\mathcal{M}$ follows mutatis mutandis the one used to get Eq. 1.64. At the end, an expression for Eq. 1.73 analogous to Eq. 1.64 is obtained

$$\begin{aligned} \mathcal{M}^{\sigma,\sigma'}_{\mathbf{G},\alpha}(\mathbf{k},\omega) = \quad & \epsilon_1^{-1}(\mathbf{G}) \int_{-\infty}^{-d/2} \mathrm{d}z\, G^{(1)}_{\mathbf{G},\alpha,\sigma,\sigma'}(z) + \\ & \epsilon_2^{-1}(\mathbf{G}) \int_{-d/2}^{d/2} \mathrm{d}z\, G^{(2)}_{\mathbf{G},\alpha,\sigma,\sigma'}(z) + \\ & \epsilon_3^{-1}(\mathbf{G}) \int_{d/2}^{+\infty} \mathrm{d}z\, G^{(3)}_{\mathbf{G},\alpha,\sigma,\sigma'}(z)\,, \end{aligned} \tag{1.74}$$

where the functions $G^{(j)}_{\{*\}}(z)$ have to be determined in terms of products of the coefficients of guided and radiative modes, respectively. The integrability of these functions for $z \to \pm\infty$ is always preserved by the products between an exponentially decaying function coming from the guided mode solutions and an oscillating one coming from radiative modes. Notice that after the calculation of Eq. 1.72, through Eq. 1.70 we get the imaginary part of ω^2/c^2, while we are interested in the quantity $\mathrm{Im}(\omega)$, which is obtained by the relation

$$\mathrm{Im}(\omega) = \frac{\mathrm{Im}(\omega^2)}{2\,\mathrm{Re}(\omega)}\,. \tag{1.75}$$

It should be noted that, owing to the scalability of the electromagnetic problem, the complex photonic dispersion in photonic crystal systems is usually displayed by the dimensionless frequency $\omega a/(2\pi c)$.

A model of disorder

As already pointed out, one of the main advantages of GME theory is that it allows to study also structures with more complicated in-plane patterns, by using a supercell. The supercell technique can be straightforwardly embedded in the perturbative treatment of diffraction losses in order to take into account also disorder effects. Among the many possible sources of disorder in a photonic crystal structure (such as non-vertical hole shape, non-homogeneous etching, surface roughness, etc.), we chose to model variation in air fraction due to imperfections in the e-beam process (see Fig. 1.9). We considered a

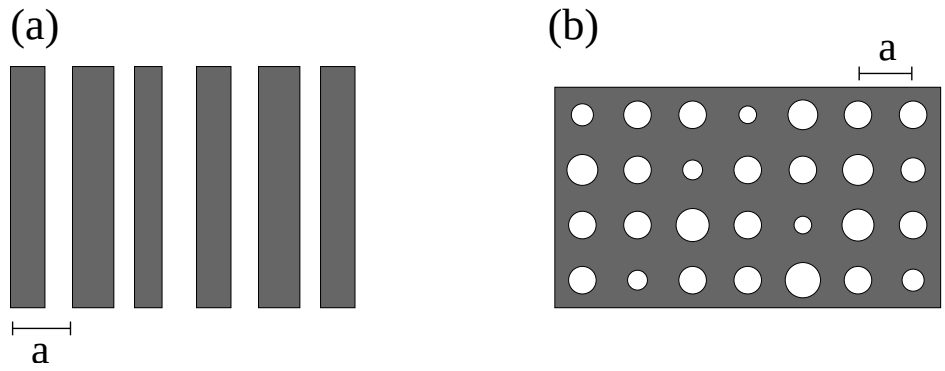

Figure 1.9: Schematic illustration of disordered supercell in (a) 1D lattice of stripes and (d) 2D lattice of holes. In both cases the effect of the random variation of the disorder parameter is exaggerated, usually being of a few percent. Moreover, a is constant within the supercell, the variation being only in the air fraction.

random variation of stripes length or hole radii within a large supercell. The variation is distributed over the supercell with Gaussian probability.

$$P(r) \propto \exp\left(\frac{-(r-\bar{r})^2}{2(\Delta r)^2}\right). \tag{1.76}$$

This way, the root mean square deviation of the Gaussian function, $\Delta r/a$ (or $\Delta l_1/a$ for 1D lattices, where l_1 is the length of the air slits), is taken as our disorder parameter, as schematically illustrated in Fig. 1.9. These variations of air fraction from the nominal value of the perfectly periodic lattice, $\bar{r}$, change the dielectric function to $\epsilon_{\rm dis}(\mathbf{r})$ and give rise to a dielectric perturbation,

$$\Delta\epsilon(\mathbf{r}) = \epsilon_{\rm dis}(\mathbf{r}) - \epsilon(\mathbf{r}). \tag{1.77}$$

The perturbative matrix element 1.72 thus becomes

$$\mathcal{H}^{\rm (dis)}_{\rm guid,rad} = \int \left(\epsilon(\mathbf{r}) + \Delta\epsilon(\mathbf{r})\right)^{-1} \left[\nabla \times \mathbf{H}^*_{\rm guid}(\mathbf{r})\right] \cdot \left[\nabla \times \mathbf{H}_{\rm rad}(\mathbf{r})\right] {\rm d}\mathbf{r}\,, \tag{1.78}$$

which can be approximated by ($\Delta\epsilon \ll \epsilon$)

$$\mathcal{H}^{\rm (dis)}_{\rm guid,rad} = \mathcal{H}^{(0)}_{\rm guid,rad} - \int \frac{\Delta\epsilon(\mathbf{r})}{\epsilon^2(\mathbf{r})} [\nabla \times \mathbf{H}^*_{\rm guid}(\mathbf{r})] \cdot [\nabla \times \mathbf{H}_{\rm rad}(\mathbf{r})]\, {\rm d}\mathbf{r} + O\left[\frac{(\Delta\epsilon)^2}{\epsilon^4(\mathbf{r})}\right], \tag{1.79}$$

where $\mathcal{H}^{(0)}_{\rm guid,rad}$ is given by 1.73, and the second term can be calculated straightforwardly from the matrix elements of Eq. 1.74 after the calculation of the Fourier transform $\Delta\epsilon(\mathbf{G})$. Basically, we solve the eigenvalue problem

to find photonic frequencies of guided and quasi-guided modes for the unperturbed lattice, and then we introduce disorder in order to estimate the losses for the given photonic mode. This way, the photonic band dispersion both below and above the light line is associated to real and imaginary parts of mode frequencies, the latter including both intrinsic and extrinsic effects. Results on disorder-induced diffraction losses for line defect modes in two-dimensional photonic crystal slabs, very important for prospective applications of these systems to integrated optics, will be presented in Chapter. 3.

Chapter 2

One-dimensional photonic crystal slabs

A theoretical study of one-dimensional (1D) lattices embedded in planar waveguides with strong refractive index contrast is presented in this Chapter. The theoretical approach relies on the Guided-Mode Expansion method outlined in Sec. 1.2. The Chapter is organized as follows: in the first two Sections results concerning the photonic band dispersion will be presented, with a systematic study of gap maps and intrinsic diffraction losses of 1D periodic systems, both for what concerns membrane and Silicon-on-Insulator (SOI) structures[1]. A comparison between experimental and calculated photonic band dispersion in a 1D photonic crystal slab in a SOI configuration is shown at the end of Sec. 2.1. In the last Section, 1D periodic systems in SOI configuration with localized defects will be addressed. Comparisons with preliminary experimental results on 1D systems with cavities in supercell configuration will be also presented in Sec. 2.3. The results of this study may be useful for the design of integrated 1D photonic structures with low radiative losses.

2.1 Photonic band dispersion

An important feature of photonic crystal slabs is the blue shift of the eigenmodes due to vertical confinement in the planar waveguide. This effect, which is more pronounced for slabs with strong out-of-plane refractive index contrast, implies that the energies of photonic bands and gaps depend on all parameters of the planar waveguide (layer thicknesses and refractive indices) and can differ substantially from those of the reference 1D or 2D system.

[1]Part of the results presented in these Sections have been published in Ref. [49].

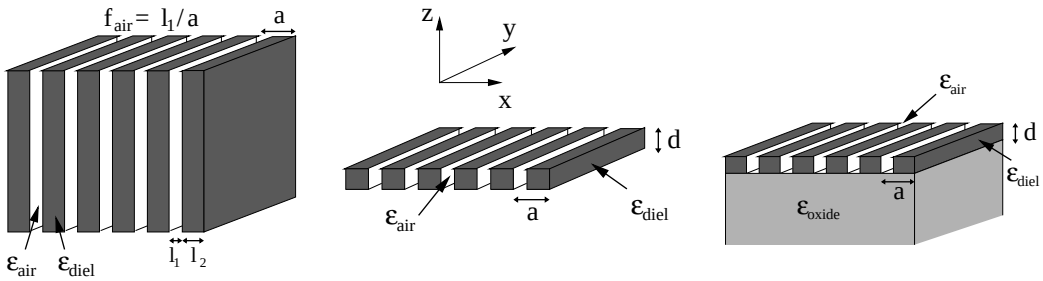

(a) Multilayer (b) Dielectric membrane (c) Asymmetric waveguide

Figure 2.1: (a) Ideal one-dimensional photonic crystal, with period a and air fraction $f_{\text{air}} = l_1/a$. (b) Photonic crystal slab consisting of a self-standing, patterned dielectric core (*air bridge* or *membrane*) of thickness d surrounded by air. (c) Photonic crystal slab, with the pattern defined in a high-index dielectric core of thickness d sandwiched between air and an insulating oxide substrate. We assume here: $\epsilon_{\text{diel}} = 12$, $\epsilon_{\text{oxide}} = 2.1$, $\epsilon_{\text{air}} = 1$.

The Guided-Mode Expansion (GME) method provides an important tool in order to account for the dependence of mode frequencies on these structural parameters by making systematic analyses. The cut-off frequency of second- and higher-order modes also depends on slab parameters and on the photonic lattice.

In this Section we present a systematic study of photonic bands and gap maps for 1D photonic crystal slabs, that is 1D photonic lattices like those of a distributed Bragg reflector (see Fig. 2.1a for the 1D reference system). These are defined in two types of waveguides with strong refractive index contrast: the self-standing membrane or *air bridge* (Fig. 2.1b) and the asymmetric photonic crystal slab in which only the core layer is patterned (Fig. 2.1c). The latter structure is typically realized with the SOI system but may also be realized with GaAs on an oxide layer. We assume the following values of the dielectric constants: $\epsilon_{\text{diel}} = 12$ for the high-index core layer (as appropriate to Si or GaAs below the band gap, and at a frequency corresponding to the typical wavelength $\lambda = 1.55$ μm), $\epsilon_{\text{air}} = 1$, and $\epsilon_{\text{oxide}} = 2.1$ (as appropriate for SiO_2 or other oxides). The periodic patterning is taken along the x direction and throughout this work we assume $k_y = 0$. The gap maps are calculated as a function of air fraction in the core layer and for different values of the core thickness, thereby exploring a wide range of parameters of experimental interest. Calculations are carried out by using a number of 31 plane waves in the finite-basis expansion for 1D periodic systems (if not otherwise specified), which is largely sufficient for convergence within percent

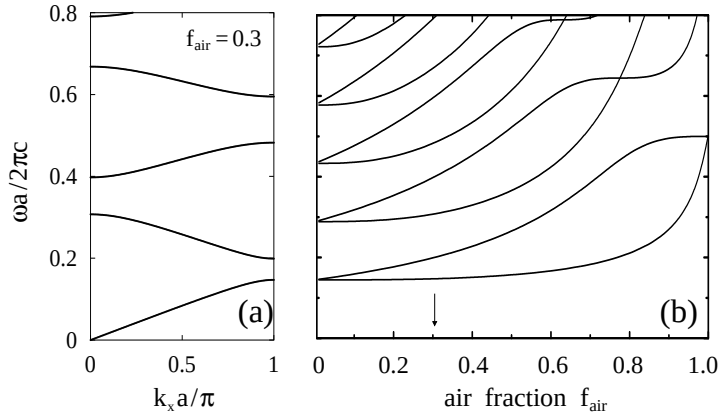

Figure 2.2: Ideal multilayer: (a) Photonic bands for $f_{\rm air} = 0.3$; TE and TM modes are exactly degenerate. (b) Gap map, i.e., band edges as a function of air fraction; the value of $f_{\rm air}$ corresponding to the calculation given in (a) is indicated by an arrow.

accuracy. The number of guided modes of the effective waveguide, α, is not found to be critical in the energy range considered, and it is usually taken to be ≤ 8.

The photonic bands and gap maps of a distributed Bragg reflector are obviously well known and are exemplified in Fig. 2.2[2]. They were calculated by simple plane wave expansion in one direction (see Sec. 1.1.1). Notice that the photonic bands of Fig. 2.2a (which refer to an air fraction $f_{\rm air} = 0.3$) as well as the gap map of Fig. 2.2b are degenerate for transverse electric (TE) and transverse magnetic (TM) polarizations with respect to the plane of incidence: this degeneracy is lifted in a waveguide because the confinement-induced shift is polarization-dependent, as was already shown experimentally by our group [19]. One of the goals of the present analysis is to establish whether a complete band gap for both polarizations can occur in a waveguide-embedded 1D photonic structure.

It is worth reminding that related concepts have already been studied in the literature in the context of dielectric waveguide gratings, also called resonant grating filters [65–77]. These kinds of diffraction gratings may support guided and leaky modes. The latter are resonantly coupled to an external light beam and give rise to narrow resonances in reflection or transmission,

[2]For $\epsilon_{\rm diel} = 12$ the $\lambda/4$ condition occurs at $f_{\rm air} = 0.776$: this corresponds to the first gap being maximum and to the vanishing of the second-order gap together with all gaps of even order.

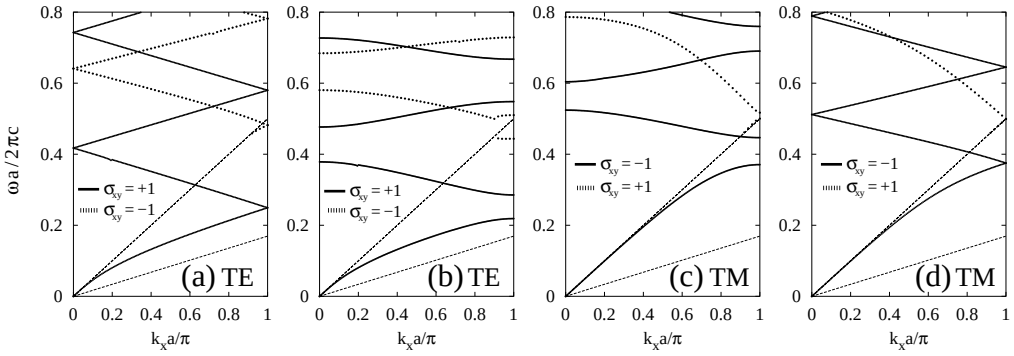

Figure 2.3: Photonic bands for the membrane structure of Fig. 2.1b. The dashed lines represent the dispersions of light in air and in the average core layer. (a) TE, (d) TM dispersion curves, folded in the first Brillouin zone, for a uniform dielectric membrane with $\epsilon_{\rm av} = 8.7$ and thickness $d/a = 0.4$; (b) TE, (c) TM photonic bands for the patterned structure with $f_{\rm air} = 0.3$, $d/a = 0.4$.

which may be used for polarization-dependent filters [65] or for enhanced nonlinear optical effects [68, 73]. Most of the research concentrated on systems with a weak dielectric modulation, e.g., surface relief gratings for filtering and distributed feedback [4, 67], waveguides with a weak refractive index contrast within the core region [66, 70] and/or which are modelled by a single Fourier component of the dielectric function [65, 71, 75]. For an extensive list of previous literature along these lines and of the different kinds of theoretical methods used we refer to the book by Loewen and Popov [69]. In all these cases, which can be treated at least qualitatively by coupled-mode theory, the dispersion of the waveguide mode is only weakly modified by the dielectric modulation and photonic bandgap effects are very small. Specific waveguide grating structures with strong refractive index modulation in the plane leading to an appreciable photonic gap have been studied in Ref. [72] for the case of TE polarization, and in Refs. [74, 77] for both TE and TM polarizations. In these strongly modulated cases a rigorous coupled-wave analysis (also called the Fourier modal method, see Sec. 2.3) is necessary and has been used. We point out that the focus of the present work is quite different from all these papers, in particular for what concerns the systematic calculation of gap maps and losses as a function of frequency and of various structure parameters.

The photonic bands of the strong confinement symmetric slab, corresponding to the system schematically shown in Fig. 2.1b, are displayed in

Fig. 2.3b and 2.3c for a core thickness $d = 0.4a$ and an air fraction $f_{\text{air}} = 0.3$. The bands are plotted by using dimensionless frequency $\omega a/(2\pi c) = a/\lambda$ as a function of in-plane wave vector $k_x a/\pi$ in the first Brillouin zone. The photonic dispersion curves of the patterned structure are compared to those of a uniform dielectric slab suspended in air (Figs. 2.3a and 2.3d) with a spatially averaged dielectric constant, given by $\epsilon_{\text{eff}} = 8.7$ in the present case. The guided modes of Figs. 2.3a and 2.3d represent the basis set for the expansion method discussed in the previous Chapter. The dispersion for the average dielectric slab is presented in the reduced zone scheme, allowing for a direct comparison with the corresponding photonic bands of the patterned waveguide. We have classified the guided modes according to mirror symmetry with respect to the plane of incidence $\mathbf{k}z \equiv xz$ (we use σ_{xz} to denote this operation) and with respect to the xy plane (σ_{xy} operation). The modes whose electric field component lies in the xy plane are referred to as TE, and are odd with respect to specular reflection through the plane of incidence ($\sigma_{xz} = -1$); the modes whose magnetic field lies in the xy plane are labelled as TM and are even with respect to mirror plane xz ($\sigma_{xz} = +1$) [34]. These modes can be classified further as even ($\sigma_{xy} = +1$) or odd ($\sigma_{xy} = -1$) with respect to specular reflection through the xy plane, thus giving four different types of guided eigenfunctions for the electromagnetic field. We can separately compare Fig. 2.3a to 2.3b and Fig. 2.3c to 2.3d. It is clearly seen that for both TE and TM modes the periodic patterning of the dielectric slab introduces band gaps around the degenerate points of the average slab dispersion curves ($k_x = 0$ and $k_x = \pm\pi/a$), owing to the off-diagonal components of the inverse dielectric tensor. There is one-to-one correspondence between average slab and 1D photonic crystal slab modes. The first-order modes (TE even and TM odd) have no cut-off frequency, as is well known for a symmetric waveguide. The second-order guided modes have a finite cut-off frequency, which is degenerate for TE and TM modes. The second-order mode, represented by dotted lines, has $\sigma_{xy} = -1$ for TE polarization, while it has $\sigma_{xy} = +1$ for TM polarization.

A second point should be remarked by comparing the photonic bands of Figs. 2.3b and 2.3c to the bands of an ideal multilayer. The first photonic band gap appears between 0.15 and 0.20 in the ideal 1D case, and between 0.22 and 0.28 for the lowest TE mode in the photonic crystal slab, due to the confinement effect along the vertical (z) direction. The gap between the first and the second band opens between 0.37 and 0.45 when considering TM modes: these values are strongly blue shifted with respect to both the multilayer and the TE modes of the photonic crystal slab. Thus the confinement effect manifests itself in the blue shift of the eigenfrequencies of the electromagnetic field with respect to the ideal multilayer, and moreover in

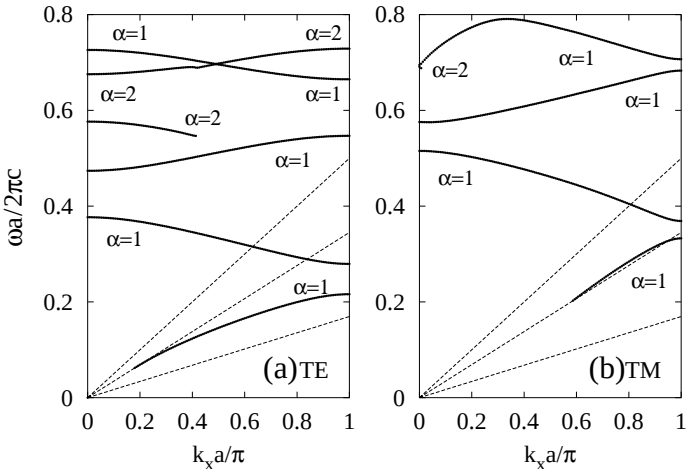

Figure 2.4: Photonic bands for the patterned dielectric-on-insulator structure of Fig. 2.1c with $f_{\text{air}} = 0.3$, $d/a = 0.4$. The dashed lines are the light dispersions in the effective core and in the upper and lower claddings; α labels the order of the guided mode. (a) TE, (b) TM modes.

the removal of degeneracy between TE and TM modes: the latter effect is due to the stronger confinement of TM compared to TE modes in the planar waveguide [4]. We also notice that all the band gaps, except for the first one, lie in the region of guided resonances, and could be experimentally tested by external reflectance measurements. The first band gap, either TE even or TM odd, is instead in the region of truly guided modes. A complete band gap common to both polarizations can also be seen around $\omega a/(2\pi c) \sim 0.4$, where the second-order TE gap overlaps the first-order TM gap. As we will see in the following, this is rather a coincidence for 1D photonic crystal slabs.

In Fig. 2.4 we display the photonic bands for the asymmetric structure represented in Fig. 2.1c. The dashed lines are the dispersions of photons in air, substrate and effective dielectric core. The parameters used in these calculations are $d/a = 0.4$, $f_{\text{air}} = 0.3$, allowing for a direct comparison with the results of Figs. 2.3b and 2.3c. Owing to the asymmetry of the vertical waveguide, σ_{xy} is no more a symmetry operation: the modes can only be classified as odd (TE, Fig. 2.4a) or even (TM, Fig. 2.4b) with respect to the plane of incidence. However, we have indicated the approximate order of the waveguide mode by the index α in Fig. 2.4 (this can be defined only when the modes are well separated in frequency, otherwise mixing and anticrossing effects occur). For an asymmetric slab there are no modes starting at $\omega = 0$ [4]. By comparing Figs. 2.3 and 2.4, we notice that the lowest TE mode of

the asymmetric 1D photonic crystal slab is in quantitative agreement with the first-order TE mode of the photonic crystal membrane; instead, the TM modes of the asymmetric slab are somewhat less confined than those of the photonic crystal membrane. It is important to stress that the modes lying between the two claddings light lines (oxide and air in this case) are evanescent in air, but leaky in the substrate. These modes have finite radiative losses, as we will see in Section 2.2. We also notice that no complete band gap is present in the asymmetric 1D photonic crystal slab, at variance with the corresponding symmetric structure. The results shown in Fig. 2.4 are conceptually similar to Brillouin diagrams calculated for TE polarization in the case of an asymmetric waveguide grating structure [72]. The described features of photonic band structures for an asymmetric 1D photonic crystal slab were experimentally verified by variable angle surface reflectance performed on SOI structures [19]. A direct comparison between measured and calculated photonic bands for SOI 1D photonic crystal slab will be shown at the end of this Section.

In Fig. 2.5 we present a complete set of gap maps for waveguide-embedded 1D photonic crystal We consider a *band gap* as a frequency region where no photonic modes exist, either truly guided or quasi-guided above the light line. We present the gap maps for modes with TE or TM polarizations, i.e., with definite parity with respect to the vertical mirror symmetry σ_{xz}: this convention applies to symmetric as well as asymmetric vertical waveguide structures. For the case of the asymmetric structure, for which the lowest-order waveguide mode has a finite cut-off, only the frequency region above the lowest-order cut-off is physically relevant.

In Fig. 2.5a,b, and c we display the calculated gap maps for the air bridge structure of Fig. 2.1b. We show the maps for three different slab thicknesses, namely $d/a = 0.2$, 0.4, and 0.8. We display in black the true complete band gap, i.e., the frequency region in which no photonic modes (or resonances) are allowed for any polarization. The gap maps are shown for air fraction varying from 0 to 0.7, which represent a realistic range for practical realization. The solid lines in Fig. 2.5 represent the cut-off frequency of the second-order waveguide mode, which is given by (see Eq. 1.48)

$$\frac{\omega_c a}{2\pi c} = \frac{a}{2d\sqrt{\epsilon_{\text{eff}} - \epsilon_{\text{air}}}} \tag{2.1}$$

and is the same for both polarizations.

An important feature that we can see from Fig. 2.5 is that for $d/a = 0.2$, the TE gap map is qualitatively similar to the ideal multilayer one (see Fig. 2.2b) with a blue shift arising from the confinement effect. The band gaps for TM modes are shifted to much higher frequencies and some complete

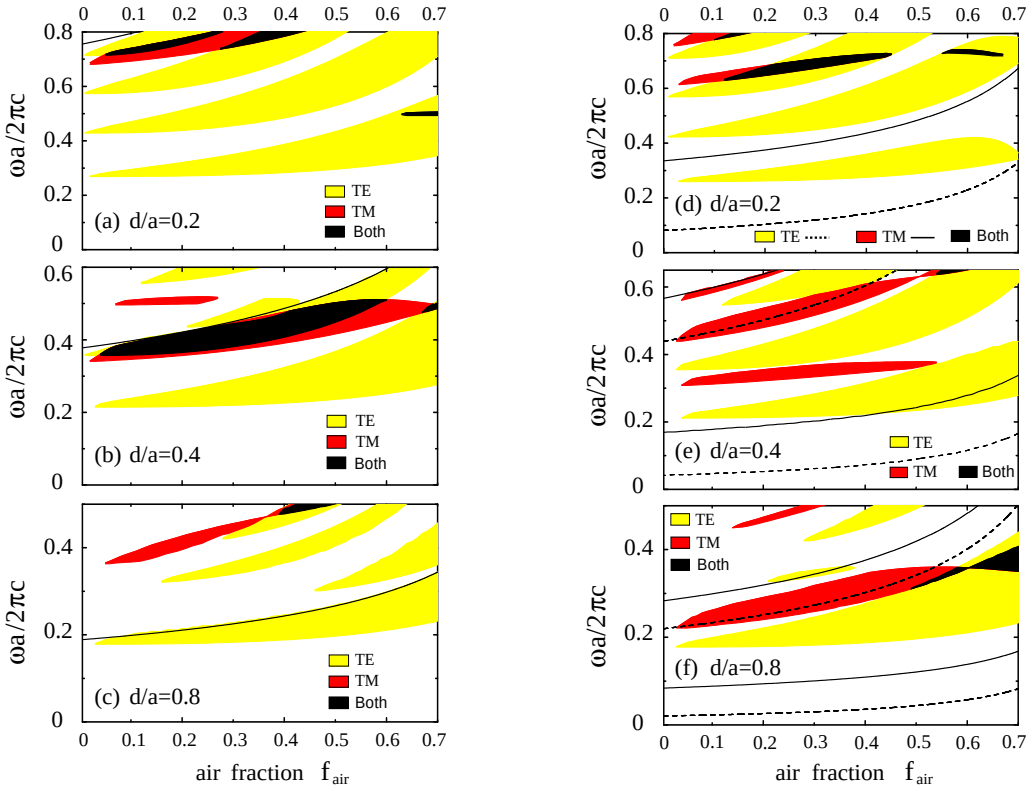

Figure 2.5: Gap maps for the membrane structure of Fig. 2.1b (left side) and the asymmetric photonic crystal slab structure of Fig. 2.1c (right side), as a function of the air fraction, $f_{\rm air} = l_1/a$. Dashed (solid) lines represent the cut-off frequencies of the first- and second-order waveguide modes for TE (TM) polarization; (a) and (d) core thickness $d/a = 0.2$, (b) and (e) $d/a = 0.4$, (c) and (f) $d/a = 0.8$.

band gaps start to appear only at $a/\lambda \sim 0.7$. The gap map is more complex for $d/a = 0.4$, due to the appearence of higher-order waveguide modes at low frequency. Nevertheless, for $a/\lambda \lesssim 0.4$ the slab is still monomode, and a large complete band gap opens in a wide range of air fractions (Fig. 2.5b). This complete gap comes from the overlap of the first TM gap (at the Brillouin zone edge, see Fig. 2.3c) and the second TE one (at the zone center, Fig. 2.3b). No complete band gap has been found for other values of d/a (calculations not shown). For $d/a = 0.8$ the photonic band structure is quite complex because the slab becomes multimode already at low frequencies. The band gap in TM modes is still present around $a/\lambda \sim 0.4$, but no complete band gap exists because of the presence of second-order TE modes. The conclusions

from these results are the following: (i) the TE gap map in a waveguide resembles the ideal 1D one only below the cut-off of second-order modes, (ii) the TM gap map is very sensitive to the structure parameters, and (iii) a complete gap for both polarizations is calculated to occur only for a core thickness around $d/a = 0.4$.

In Fig. 2.5d,e and f we show the calculated gap maps of the asymmetric 1D photonic crystal slab of Fig. 2.1c, for core thicknesses $d/a = 0.2$, 0.4, and 0.8. These gap maps show notable differences as compared to those of the photonic crystal membrane. One of the peculiarities of the asymmetric structure is the existence of a finite cut-off frequency for the lowest-order TE and TM modes, as pointed out in Sec. 1.1.2. The cut-off frequency as a function of air fraction is plotted with dashed lines for TE modes, and with solid lines for TM modes. The values for the cut-off frequencies obtained by the present approach coincide with those following from the expression (see Eqs. 1.42 and 1.43)

$$\frac{\omega_c a}{2\pi c} = \frac{a}{2d\sqrt{\epsilon_{\text{eff}} - \epsilon_{\text{oxide}}}} \left[m + \frac{1}{\pi} \arctan\left(r \frac{\sqrt{\epsilon_{\text{oxide}} - \epsilon_{\text{air}}}}{\sqrt{\epsilon_{\text{eff}} - \epsilon_{\text{oxide}}}} \right) \right] \qquad (2.2)$$

where $r = 1$ for TE modes, $r = \epsilon_{\text{eff}}/\epsilon_{\text{air}}$ for TM modes, and $m \geq 0$ is an integer.

For $d/a = 0.2$ the asymmetric 1D photonic crystal slab has only first-order TE and TM modes in the whole frequency range shown. The TE band gaps are again qualitatively similar to those of the ideal 1D multilayer, with a confinement effect which is close to that of the membrane case (Fig. 2.5a); the TM gaps are instead shifted to much higher frequencies as compared to the 1D multilayer. The first TE band gap is in a region below the cut-off of the first-order TM mode, thus it may be considered as a complete band gap. For $d/a = 0.4$ and 0.8 a second-order TE cut-off appears at frequencies around 0.44 and 0.22, respectively: the TE gap map is similar to that of the 1D multilayer only below the second-order cut-off frequency. The TM gaps are always very different from those of the ideal 1D case and also quite different from those of the photonic crystal membrane: TM modes are seen to be extremely sensitive to the structure parameters (core thickness and claddings dielectric constants). As it can be seen by comparing Figs. 2.5b and 2.5e, the complete band gap for $d/a = 0.4$ occurs for the particular case of a 1D photonic crystal membrane but not in the asymmetric photonic crystal slab. For $d/a = 0.8$ a complete band gap resulting from the overlap of the first TE and TM gaps appears around $a/\lambda \sim 0.3$ for $f_{\text{air}} \gtrsim 0.5$.

Numerical results for photonic bands and gaps previously shown relate only to the real part of the frequency and do not consider the effect of coupling

to radiative waveguide modes. Thus, the physical relevance of a photonic band dispersion is expected to decrease on increasing the frequency far from the light line. We also notice that the concept of mode cut-off for resonant modes is not clearly defined when radiative broadening is taken into account. For these reasons, the gap maps calculated here are expected to be more useful in the low frequency region, in particular for the band gaps which open below the second-order cut-off lines shown in Fig. 2.5.

Comparison with experimental data

In this paragraph a comparison between calculated and measured photonic bands is presented for asymmetric 1D photonic crystal slabs. The samples were fabricated on Silicon-on-Insulator wafers manufactured by SOITEC, in which only the core layer (260 nm thick) was patterned by electron beam lithography. Details on the fabrication process are given in Ref. [21]. As a general remark, the structural parameters are chosen in order to have a photonic band gap centered around the typical telecommunication wavelength, $\lambda = 1.5$ μm. The final structure is the realization of the schematic picture shown in Fig. 2.1c. The experimental technique employed is the variable-angle reflectance (VAR) from the slab surface [14].

As already pointed out, the resonant features seen in reflectance or transmission spectra are related to the coupling of guided modes of the photonic crystal slab to the incoming beam through the grating effect. In fact, the in-plane momentum conservation law that forbids this coupling in the case of a uniform slab is no more valid owing to the periodic patterning. A mode with in-plane momentum $\mathbf{k}$ is coupled to an external plane wave provided that its momentum is conserved modulo a reciprocal lattice vector $\mathbf{G}$. A photonic crystal slab mode with frequency ω and Bloch wave vector $\mathbf{k}$ couples, in principle, to all radiative modes with the same frequency and momentum $\mathbf{k}+\mathbf{G}$ provided that the condition $\epsilon\omega^2 - |\mathbf{k}+\mathbf{G}|^2 > 0$ is satisfied, where ϵ is the dielectric constant of the external medium in which the incoming beam is propagating (usually air, and thus $\epsilon = \epsilon_{\text{air}} = 1$). The latter condition represents a simple formulation of the *light line issue* that has been introduced in the first Chapter, which allows to discriminate between truly guided and quasi-guided modes. Out-of-plane diffraction losses in photonic crystal slabs are a natural consequence of the periodic patterning, which introduces scattering in the radiative modes if the coupling condition is satisfied. The reciprocal process is the coupling of an external wave to a quasi-guided mode. The incident plane wave has frequency ω and momentum $(\mathbf{k}, k_z)$, where k_z is its vertical component. The external wave excites the quasi-guided modes of the system before being reflected or transmitted. The anomaly in re-

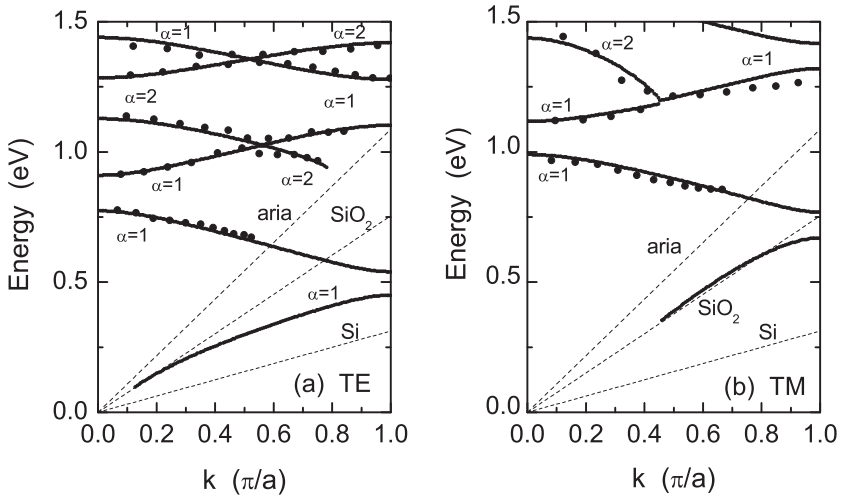

Figure 2.6: Comparison between experimental (points) data and theoretical calculations (lines). The points are extracted from angle-resolved reflectance spectra (courtesy of M. Galli); (a) TE and (b) TM modes. Parameters of calculations are taken from the nominal structural parameters of the sample, i.e. $d = 260$ nm, $a = 560$ nm, $f_{\text{air}} = 0.18$.

flectance (or transmittance) occurs when the incident wave is resonant with a quasi-guided mode in energy and in-plane momentum.

In Fig. 2.6 the comparison between calculated and measured photonic bands is shown, for both TE and TM polarized incident light. The experimental points are extracted from VAR spectra (not shown here) through the relation $\mathbf{k} = (\omega/c)\sin\theta$ between the incident angle and the in-plane wave vector component along the periodicity direction, see also App. A. The three light lines appearing in Fig. 2.6 correspond, for increasing energies, to the effective core layer with average dielectric constant ϵ_{eff}, to the uniform SiO_2 cladding and to the air light line. Calculations were carried out by using the GME method; the frequency dispersion of the dielectric constants of Si and SiO_2 was taken into account by calculating the bands in different energy ranges. In particular, considering the photonic dispersion of, e.g., TE modes (Fig. 2.6a), the bands were separately calculated from 0 to 0.76 eV, from 0.76 to 1.3 eV, and from 1.3 to 1.5. The light lines correspond to the dielectric constants values assumed in the first energy interval. A similar procedure was followed for TM modes calculations of Fig. 2.6b. There is a very good agreement between calculated and measured dispersion, for both TE and TM quasi-guided modes. This means not only that the GME is a powerful and reliable tool for calculating photonic eigenmodes of high index

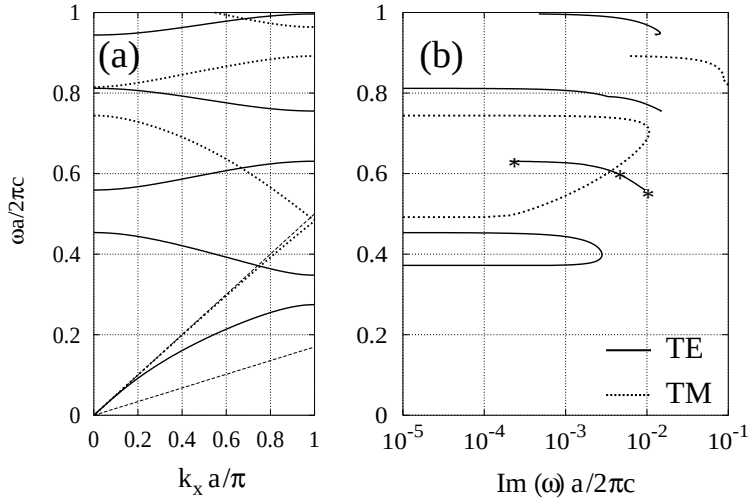

Figure 2.7: (a) Photonic bands and (b) imaginary part of frequency for a symmetric 1D photonic crystal membrane; parameters are $d/a = 0.2$, $f_{\rm air} = 0.3$. Solid (dashed) lines are TE (TM) modes.

contrast photonic crystal slabs, but also that the choice of the effective dielectric constant as spatial average is a very good approximation, for both polarizations.

2.2 Intrinsic diffraction losses

To complete our analysis of 1D photonic crystal slabs we have to address also the imaginary part of frequency, which gives information about the radiative losses due to out-of-plane diffraction. This is done by using time-dependent perturbation theory for the electromagnetic problem, as discussed in the previous Chapter. The number of plane waves and of guided modes of the effective planar waveguide are taken to be, respectively, 37 and ≤ 8 in the basis expansion. In Figs. 2.7a and 2.7b the band diagram and the corresponding imaginary part of frequencies are shown for the symmetric 1D photonic crystal slab with parameters $d/a = 0.2$ and $f_{\rm air} = 0.3$. In Fig. 2.7a the waveguide is monomode for both TE and TM polarizations. In Fig. 2.7b we show the dimensionless quantity $\mathrm{Im}(\omega)a/(2\pi c)$, corresponding to each photonic band of Fig. 2.7a, as a function of mode frequency. The imaginary part is generally much smaller than the real part, indicating the validity of the perturbative treatment adopted. The losses go to zero when the mode crosses the light

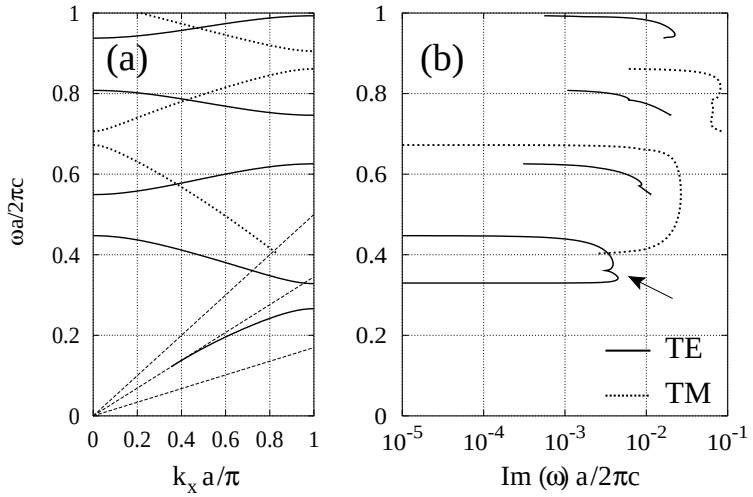

Figure 2.8: (a) photonic bands and (b) imaginary part of frequency for an asymmetric 1D photonic crystal slab; parameters are $d/a = 0.2$, $f_{\mathrm{air}} = 0.3$. Solid (dashed) lines are TE (TM) modes. The arrow in (b) denotes the cusp, which corresponds to the second TE band in (a) crossing the air light line.

line in air and becomes truly guided. It is clear from the figure that the radiative losses generally increase on increasing the photonic band index, however the behavior of the losses within a given photonic band is nontrivial and has to be studied in each specific case. The guided resonances at the Brillouin zone center present a quite interesting behavior. In fact, the second and the fourth TE bands have zero linewidth at $k_x = 0$ (their frequencies are $\omega a/(2\pi c) = 0.45$ and 0.81, respectively) while the third and the fifth band have finite radiative widths at $k_x = 0$ ($\omega a/(2\pi c) = 0.56$ and 0.94). A similar behavior holds also for TM modes. These numerical results could be probed by variable angle surface reflectance experiments made on 1D photonic crystal membranes: the imaginary part of the frequency can be extracted from the linewidth of spectral structures in reflectance that correspond to photonic modes [15, 16].

In Fig. 2.8 we show the results for an asymmetric 1D photonic crystal slab with the same thickness and air fraction[3]. The radiative losses shown in Fig. 2.8b display quite the same behavior as in the membrane case. They

[3]In Ref. [72] a Brillouin diagram for the losses is shown, i.e., the imaginary part of the wave vector is displayed as a function of frequency. The meaning of the loss diagram is therefore different from those in Figs. 2.7 and 2.8, in particular the imaginary part of the wave vector is largest in the photonic gap regions.

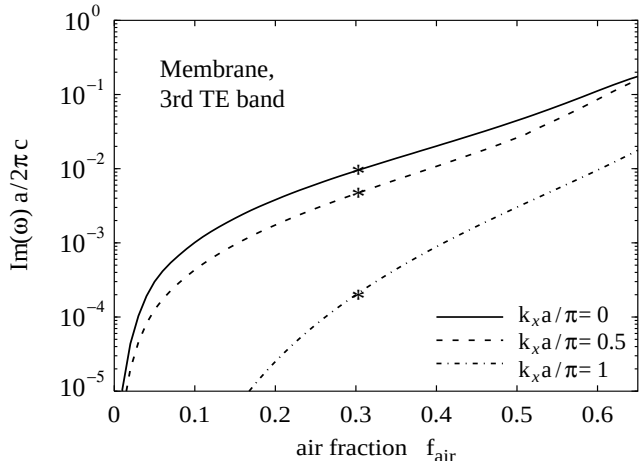

Figure 2.9: Imaginary part of photonic frequencies as a function of the air fraction for the photonic crystal membrane of thickness $d/a = 0.2$; the three curves correspond to different wave vectors ($k_x = 0$, $k_x = \pi/2a$, $k_x = \pi/a$) in the first Brillouin zone of the third TE photonic band. The three points marked on the curves correspond to the three markers of Fig. 2.7b, where $f_{air} = 0.3$.

are about two times larger than the corresponding losses of Fig. 2.7b: this is due to the asymmetry of the vertical waveguide, which implies that a quasi-guided mode above the light line is coupled to all radiative modes of the effective waveguide at the same frequency, without the parity selection rule which holds instead in the symmetric case. A similar behavior was found in the calculation of spectral properties of deep 1D gratings [38]. Moreover, the higher-order modes (either TE or TM) now have a finite $\mathrm{Im}(\omega)$ also at $k_x = 0$: this is due to the additional diffraction channels for radiative losses which are present in the asymmetric waveguide. Moreover, we notice that the modes whose frequencies lie between the light lines of air and oxide claddings are not truly guided, i.e., they are evanescent in air but leaky in the substrate. Thus, the crossing between a band and the light line in air does not cause the linewidth of the photonic resonance to go to zero: rather, $\mathrm{Im}(\omega)$ has a cusp (marked by an arrow in Fig. 2.8b) when the light line in air is crossed. Similar features can by recognized in Fig. 2.8b at higher frequencies: they arise whenever a photonic mode crosses a cladding light line folded in the first Brillouin zone. These notable features of $\mathrm{Im}(\omega)$ are not a numerical artifact, but rather they correspond physically to the opening or closing of diffraction channels for radiative losses.

We also found that the imaginary part of frequency increases on increasing the air fraction in the investigated range, as shown in Fig. 2.9, where $\mathrm{Im}(\omega)a/(2\pi c)$ is plotted for the photonic crystal membrane of thickness $d/a = 0.2$. A similar behavior is found also for the asymmetric structure (not shown here) and an increase of the photonic mode linewidth with the air fraction was already stated experimentally [19, 24]. The three curves of Fig. 2.9 correspond to the evolution of the losses for the third TE photonic band at three different points in the first Brillouin zone. When $f_{air} = 0.3$ the corresponding photonic band has frequencies around $\omega a/(2\pi c) = 0.6$ (see Fig. 2.7a), and the three points marked in Fig. 2.9 correspond to those marked in Fig. 2.7b. Notice that the losses vary in a logarithmic scale and become extremely small either towards the homogeneous waveguide limit at low air fraction or close to the Brillouin zone edge. While the filling fraction dependence of the losses is similar for all bands and polarizations, the wave vector dependence changes from band to band, as it appears from Figs. 2.7b and 2.8b. It can be concluded that for the present waveguide-embedded 1D photonic structures, the spectral linewidth of quasi-guided photonic modes can vary by several orders of magnitude and it depends in a nontrivial way on the structure parameters as well as on the angle of incidence, mode index, and polarization.

2.3 Cavity modes and quality factors

In this Section the study of defect cavities in 1D photonic crystal slabs, namely Fabry-Pérot cavities in waveguide geometry, is presented and the problem of determining the quality (Q) factor of localized cavity modes is addressed. These devices are considered as potential building blocks in SOI planar photonic integrated circuits operating at optical wavelengths for advanced telecom applications, thus we focus on SOI slab structures. The problem is tackled by three different theoretical approaches: (i) the Guided-Mode Expansion (GME) method outlined in Sec. 1.2, (ii) a calculation of surface reflectance at varying angles of incidence using grating or scattering-matrix methods (SMM), and (iii) a calculation of in-plane transmission on a finite structure employing a Fourier modal expansion (FME) method. The GME and SMM methods require that the defect cavity be repeated with supercell periodicity along the 1D axis, while the FME method deals with a finite structure. Part of this comparative theoretical analysis is the result of a collaboration with Ph. Lalanne, at the "Laboratoire Charles Fabry de l'Institut de Optique," CNRS, Orsay Cedex, France, who performed the calculations with the FME approach. The goal of this Section is twofold. First,

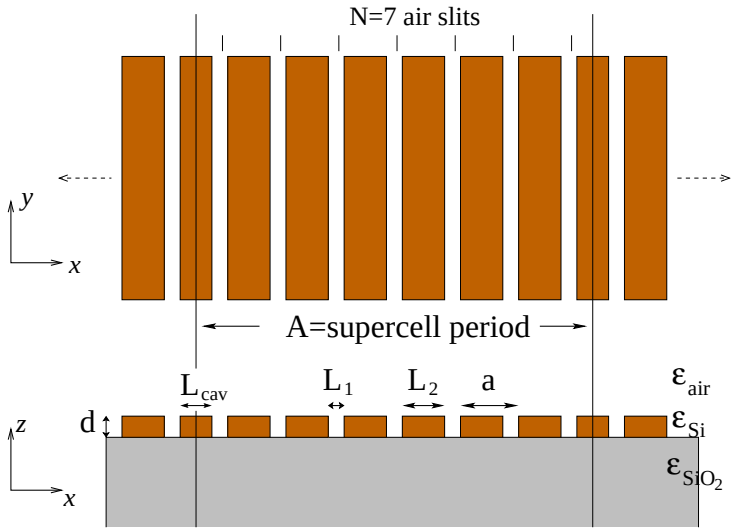

Figure 2.10: Schematic picture of the structure considered for calculations with GME and SMM approaches. Upper and lower claddings are assumed to be semi-infinite along z, and the structure is uniform along y. The main structural parameters are defined. The air fraction is $f_{\text{air}} = L_1/a$; N is the number of air slits between consecutive cavity layers.

to show that the different methods yield the same results for the Q-factors. Second, to prove that the intrinsic Q-factor of a single cavity can be determined by working on a periodic structure in a diffraction geometry, i.e., by measuring the reflectance from the surface of the sample at varying angles of incidence. A brief overview of the alternative theoretical approaches adopted is given, then numerical results will be presented. Finally, a comparison with preliminary experimental measurements will be shown.

A schematic picture of the structure considered here is shown in Fig. 2.10, where the parameters are also defined and the supercell along the direction of periodicity can be seen. The latter is used in the calculation of the photonic band dispersion by the GME method, and also of reflectance by the SMM, which will be briefly introduced in the following. These cavities were designed to have a resonant wavelength of $\lambda = 1.5\,\mu$m in a SOI slab with a Silicon layer of thickness $d = 260$ nm. Two kinds of mirrors with a mid-gap frequency equal to the resonant frequency are considered, namely first- and second-order Bragg mirrors[4]. Two physical mechanisms are responsible for the finite mode lifetime of the cavity. For first-order Bragg mirrors, the fundamental

[4]In this work only results concerning the second-order cavity modes will be shown. The same conclusions hold for the first-order one.

Bloch mode of the mirror is truly guided, and the mode lifetime is limited solely by a mode-profile mismatch problem between the fundamental guided mode of the slab waveguide (which is cycling between the mirrors) and the fundamental Bloch mode of the mirror [40]. This mismatch problem results into radiation losses in the claddings with a finite modal reflectivity of 98% at $\lambda = 1.5\,\mu$m for the fundamental guided mode impinging onto a semi-infinite mirror. The first-order gap lies fully below the cladding light lines and the intrinsic Q-factor calculated for a cavity with semi-infinite mirrors is rather high[5]. The cavity designed with second-order Bragg mirrors suffers from additional losses. In this case, the second-order photonic gap lies above the light line in air and the cavity mode has sizeable contributions from leaky Bloch modes of the mirrors. Thus as the light is reflected back from the mirrors, it is additionally radiated into the claddings. This additional source of radiation results in a lower modal reflectivity of 93.5% at mid-gap frequency and to a smaller intrinsic Q-factor.

The scattering matrix method

The Q-factor of a one-dimensional cavity can also be estimated by considering a periodic system and calculating optical spectra for light incidence on the surface of the photonic crystal slab. Illuminated by an incident plane wave, the transmission or reflection spectrum of the periodized cavity (a one-dimensional grating in fact) should present an anomaly for the resonant wavelengths. This anomaly results from a pole of the scattering matrix, which relates the Rayleigh expansion of the electromagnetic fields in the claddings [67]. The method that has been used here for the calculation of the reflection spectra is a frequency-domain method, which relies on Fourier expansion techniques for all the electromagnetic fields quantities. Because the literature on the analysis of gratings with Fourier expansion techniques is largely documented [67], the method is not detailed here. The implementation we used, which can also be applied to 2D photonic lattices, is described in [31] and will be referred to henceforth as scattering-matrix method (SMM). In the present work, all the theoretical results concerning reflectance spectra calculated within the SMM have been obtained with a numerical algorithm developed in our group in the last years. For the detailed implementation of the algorithm we refer to Ref. [44]. A brief overview of the numerical method is also given in App. B.

The geometry for the grating calculation is shown in Fig. 2.11. The light beam is incident on the surface of the structure in direction perpendicular to

[5]These calculations will not be shown here, see Ref. [54] for details.

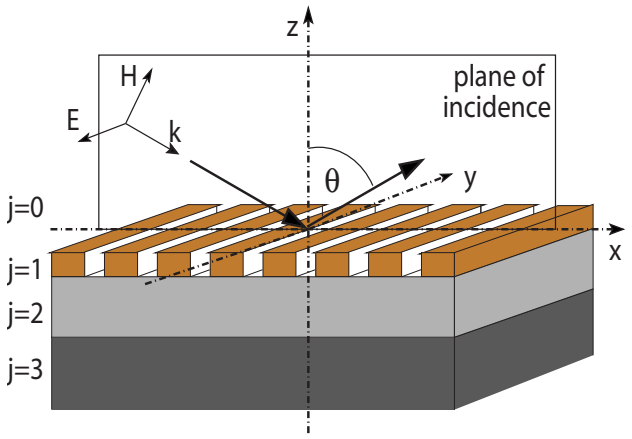

Figure 2.11: Schematic picture of geometrical structure employed in the SMM method for one-dimensional periodic lattices.

the grating, i.e., a classical (non-conical) diffraction geometry is used. The present method is the theoretical realization of the variable-angle reflectance experimental set-up described in App. A, and has been widely tested [44].

The Fourier modal expansion method

Fourier expansion methods like the rigorous coupled-wave analysis [78] or the differential method [79], which are widely used for modelling periodic structures, can also be used for modelling non-periodic systems. Such an extension has been first pointed out in Refs. [74, 76]. This approach drastically extends the domain of application of grating theories, and will be referred to henceforth as Fourier modal expansion (FME) method. Referring to Fig. 2.12, a supercell is introduced in the z-direction, perpendicular to the plane xy of the slab. The boundaries of the supercell incorporate perfectly matched layers [80] that absorb the light scattered by the corrugation. The electromagnetic fields are null on every transversal boundary and can be expanded in a Fourier series (plane-wave expansion). Radiative and guided modes are thus calculated for each uniform layer in a Fourier basis. Transmission and reflection can be evaluated by using a scattering matrix to match the field amplitudes in the different layers:

$$\begin{bmatrix} \mathbf{b}^{(i)} \\ \mathbf{f}^{(i)} \end{bmatrix} = \mathbf{S} \begin{bmatrix} \mathbf{0} \\ \mathbf{f}^{(t)} \end{bmatrix} \tag{2.3}$$

where $\mathbf{b}^{(i)}$ and $\mathbf{f}^{(i)}$ are column vectors whose elements represent the amplitudes of the backward and forward propagating modes at the input plane,

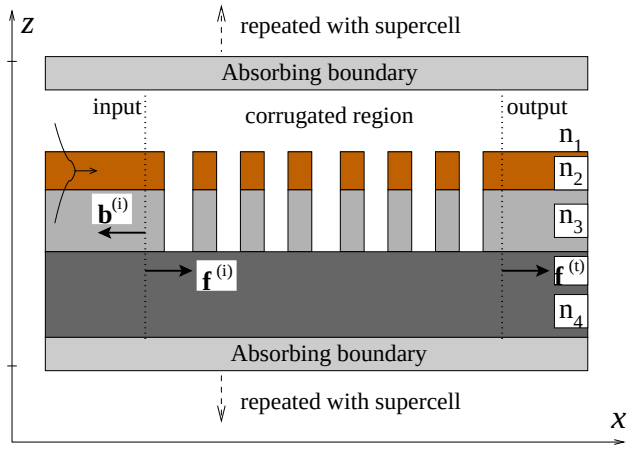

Figure 2.12: Schematic picture of geometrical structure employed in the FME method. The scattering matrix is used to relate the field amplitudes between the different layers along x, and a Fourier expansion is made along z with supercell periodicity.

and similarly $\mathbf{f}^{(t)}$ is the vector of amplitudes of the forward field at the output plane. As an example, let us consider the waveguide geometry of Fig. 2.12. If we assume to illuminate the corrugated region with the fundamental TE mode, all components of the vector $\mathbf{f}^{(i)}$ will be zero except the component $f_p^{(i)} = 1$ corresponding to that mode. The amplitudes of backward- and forward-propagating modes are then computed by using the **S**-matrix, and the reflected and transmitted intensity can be simply defined by $R = |b_p^{(i)}|^2$ and $T = |f_p^{(t)}|^2$. The Q-factor of a cavity mode can be evaluated by $Q = \mathrm{Re}(\tilde{\lambda})/[2\mathrm{Im}(\tilde{\lambda})]$, where $\tilde{\lambda}$ is the complex pole of the scattering matrix.

Numerical results and discussion

We consider here the case of a cavity surrounded by second-order Bragg mirrors. The structure has the following parameters: $d = 260$ nm, $a = 560$ nm, $L_{\mathrm{cav}} = 335$ nm, $L_1 = 100$ nm, $L_2 = 460$ nm, with an air fraction $f_{\mathrm{air}} = L_1/a = 0.1786$. In Fig. 2.13 the photonic band dispersion is shown for the ideally infinite 1D lattice as well as for the cavity structure. Only TE-polarized modes are considered here. The dielectric constants of the patterned core layer and the uniform upper and lower claddings are set to the following values: $\epsilon_{\mathrm{air}} = 1$, $\epsilon_{\mathrm{Si}} = 12.1104$, $\epsilon_{\mathrm{SiO_2}} = 2.0736$, as appropriate for these materials at $\lambda = 1.5$ μm. An effective dielectric constant given by

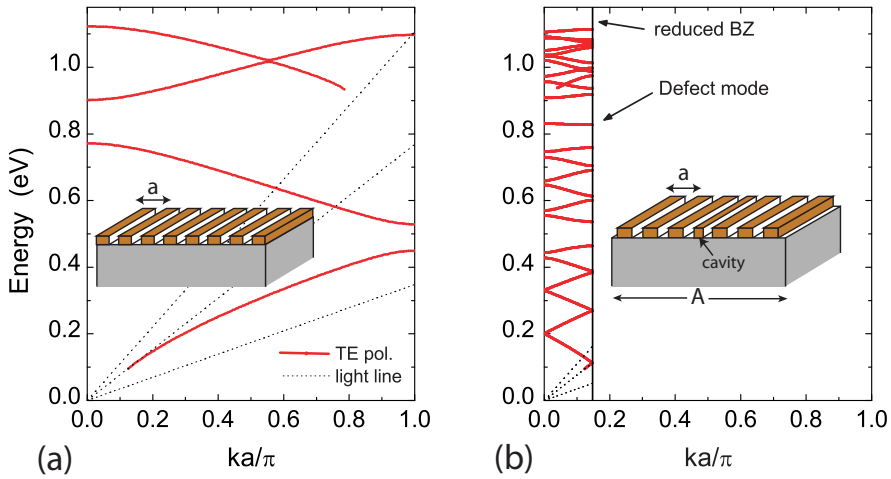

Figure 2.13: Photonic band dispersion of TE-polarized modes as a function of dimensionless wave vector for (a) 1D lattice of Silicon stripes on a SiO_2 cladding with lattice constant $a = 560$ nm, thickness $d = 260$ nm, air fraction $f_{\text{air}} = 0.1786$, and (b) 1D cavity of length $L_{\text{cav}} = 335$ nm and 7 air slits between two consecutive cavities in the supercell.

the spatial average in each layer is chosen to define the basis set for the GME method, which is a very good approximation for TE modes [49]. A number of 91 plane waves and $\alpha = 8$ guided modes of the effective planar slab are taken in the basis set for the photonic band calculations of the structure with defects.

The dispersion of the Fabry-Pérot resonator is displayed in a reduced Brillouin zone (BZ) in Fig. 2.13b, owing to the super-periodicity introduced in the calculation. The supercell period is defined as $A = NL_1 + (N-1)L_2 + L_{\text{cav}} = Na - L_2 + L_{\text{cav}}$, and it is about seven times larger than the period of the Bragg reflector, a, in this particular case; thus, the BZ is reduced by a factor of about seven. The photonic bands, folded in the reduced zone, can be recognized in Fig. 2.13b as compared to those of Fig. 2.13a. The main difference is that a defect mode appears as an almost dispersionless band within the TE band gap, at an energy $E_{\text{cav}} \simeq 0.825$ eV ($\lambda = 1.5$ μm). This defect mode lies in the radiative region of the $(\mathbf{k}, \omega)$ plane and it can be excited by light incident on the surface of the planar waveguide.

In Fig. 2.14a the band dispersion of the defect mode is displayed in the energy range between 0.7 and 1 eV, and in Fig. 2.14b the imaginary part of mode energies calculated by the perturbative approach described in the previous Chapter is also shown. The imaginary part of frequency

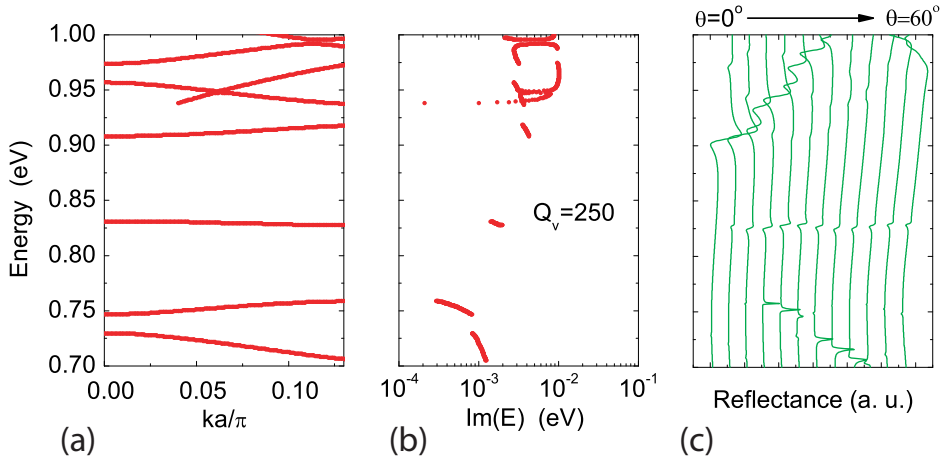

Figure 2.14: (a) Dispersion of the defect mode, (b) imaginary part of mode energy corresponding to each photonic band, and (c) surface reflectance for angles ranging from 0° to 60° in steps of 5° for classical diffraction and TE polarization (geometry of Fig. 2.11). Reflectance curves are shifted by $\Delta R = 0.5$ for clarity.

is always much smaller than the real part, thereby justifying a posteriori the perturbative treatment. In Fig. 2.14c the calculation of variable -angle reflectance by the SMM is plotted on the same energy range, in order to make a direct comparison with the dispersion of Fig. 2.14a,b. It is worth reminding that the SMM allows an exact solution of Maxwell equations for layered structures, and is in practice the theoretical realization of a VAR experiment.

The same supercell along the periodicity direction was employed for SMM calculations. As outlined in App. A, each resonance in the VAR spectrum marks a point in the $(\mathbf{k}, \omega)$ plane, and the wave vector component parallel to the surface can be extracted from the angle of incidence by the relation $k = (\omega/c)\sin\theta$. Very good agreement between GME and SMM is found in the present case, in particular concerning the energy position of the defect mode and of the band gap edges. The excitation of the cavity mode can be recognized in the reflectance spectrum as a dispersionless feature as a function of the angle of incidence. Moreover, the spectral linewidth of the structure observed in reflectance are related to the imaginary parts of Fig. 2.14b. Cavity modes of Fabry-Pérot resonators with supercell periodicity were probed with this experimental technique on GaAs-based systems [22]. A comparison with experimental data obtained on SOI samples will be given at the end of the Section. The vertical Q-factor, Q_{v}, of the cavity mode,

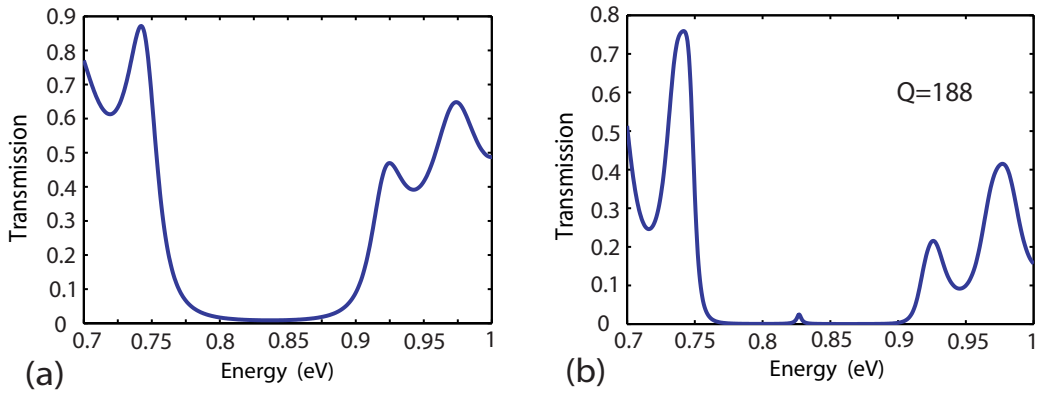

Figure 2.15: (a) Transmission through 5 air slits Bragg mirror (parameters as in Fig. 2.13); the width of the photonic band gap should be compared to calculations of Fig. 2.14a and c. (b) Transmission through a structure analogous to the one of Fig. 2.16a, with a cavity surrounded by mirrors with 5 air slits.

that is the one determined by out-of-plane losses, depends slightly on the parallel wave vector because the imaginary part of the energy does. This effect vanishes in the limit of a very large supercell. In order to smear out the effect of a finite supercell width and to get a single number for the Q_{v}-factor from the calculations of Figs. 2.14a and b, the mode energy and the corresponding imaginary part are averaged over the first BZ and then the following definition is applied: $Q_{\mathrm{v}} = E_{\mathrm{av}}/[2\mathrm{Im}(E)]_{\mathrm{av}}$. Thus, a Q_{v} of 250 is obtained for such a structure, which is in favorably good agreement with the Q-factors estimated from the resonant features in reflectance spectra. This value slightly depends on the number of air slits in the mirrors around the cavity layer and is already converged for $N = 7$.

In Fig. 2.15 transmission calculations by the FME method are shown for a 1D photonic crystal slab of finite length (Fig. 2.15a), and for a cavity between two mirrors with the same number of slits (Fig. 2.15b). The mirrors are composed of 5 air slits in both cases. The same structure parameters as in the previous calculations are used. The reflection and transmission coefficients are calculated after excitation with the fundamental TE guided mode of the initial planar waveguide. The band gap is clearly seen to be in good quantitative agreement with both GME calculation of Fig. 2.14a and SMM calculations of Fig. 2.14c, between 0.75 and 0.9 eV. The cavity mode produces a Lorentzian peak in the transmission spectrum, which is displayed in Fig. 2.15b, with a calculated Q-factor of 188. The total Q of such a system

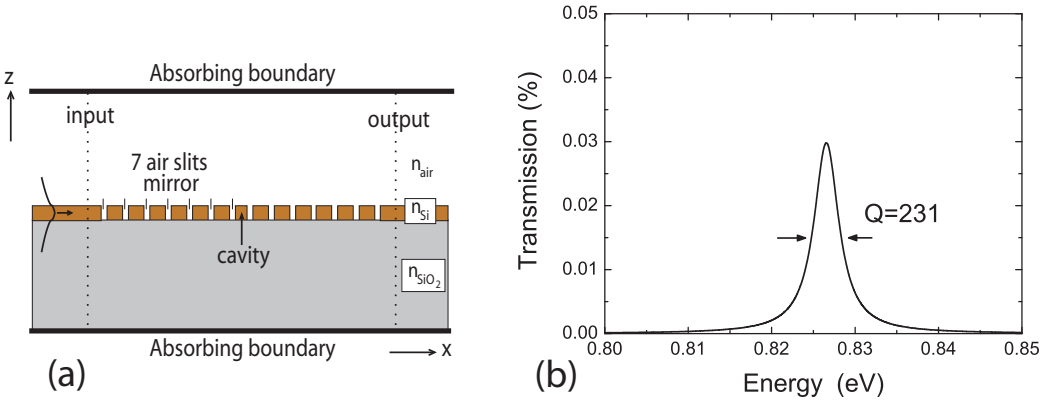

Figure 2.16: (a) Schematic picture of the geometry employed for the FME calculation; (b) Transmission of the fundamental TE mode through the structures displayed in (a), with parameters as in Fig. 2.13.

can be expressed as [81]

$$Q = \frac{Q_{\mathrm{p}} Q_{\mathrm{v}}}{Q_{\mathrm{p}} + Q_{\mathrm{v}}} \tag{2.4}$$

where Q_{p} is the planar Q-factor due to the confinement induced by the mirrors. The resonant transmission in the cavity mode is very low in this case, owing to reflection and diffraction losses over the length of the structure (calculations not shown).

In order to make a direct comparison with the calculations of Fig. 2.14, a detailed view of the transmission peak for the structure represented in Fig. 2.16a is shown. The cavity layer is inserted between two Bragg mirrors with 7 air slits each. The calculated total Q-factor for this structure is $Q = 231$, as indicated in Fig. 2.16b. This value is in good quantitative agreement with the one obtained by the calculation of Q_{v} from either the GME or the SMM methods in Fig. 2.14. This means that with 7 air slits in the mirrors Q_{p} is much larger than Q_{v}, and thus $Q \simeq Q_{\mathrm{v}}$.

In table 2.1 the calculated Q-factors and the maxima of the transmission peaks for different numbers of air slits in the mirrors are shown. On increasing the number of periods in the mirrors surrounding the cavity, it is clear that the total Q-factor tends to Q_{v}. Thus we confirm that all theoretical methods adopted here lead to the same value for the vertical Q-factor. Also, we conclude that the Q-factor can be determined by measuring the radiative coupling between a plane wave incident from the surface and the cavity mode with supercell repetition, as described by the calculations of Fig. 2.14. This may be more convenient than measuring the in-plane modal transmission:

Table 2.1: Quality factors and transmission peaks calculated with the FME method. Parameters of the structure as in Fig. 2.13, but with increasing number of air slits per mirror.

Number of slits	Q-factor	T_{peak} (%)
3	71	45
4	150	15
5	188	2.5
6	220	0.3
7	231	0.03

indeed, when the mirrors have many periods the total structure is longer in length and the transmission in the cavity mode is low, because of reflection and diffraction losses, thus making the measurement a difficult one. We notice that no optimization of the structure was made to reach a high Q-factor as done, e.g., in [82]. Higher Q-factors can be obtained in a natural way by using first-order Bragg mirrors, i.e., with a photonic gap at the border of the BZ in the region below the cladding light lines [54].

In conclusion, numerical results for cavity modes in 1D photonic crystal slabs based on Silicon-on-Insulator technology have been presented. The three methods employed, namely guided-mode expansion, scattering-matrix method, and Fourier modal expansion have been shown to lead to the same values for the cavity Q-factors. The GME and SMM methods treat systems with a periodic repetition of the cavity along the 1D axis and infinite extension in the vertical direction, while the FME method deals with a finite structure along the 1D axis and perfectly matched layers in the vertical direction. The Q-factors obtained by the FME method increase with the number of periods in the Bragg mirrors and tend to the vertical Q determined by GME or SMM methods when the effect of escape in the finite 1D structure is negligible. Thus, the Q-factor of cavity modes can be obtained from experiments by coupling from the surface of the waveguide and measuring the reflectance of a periodized cavity system. The cavity mode in reflectance spectra is more easily detectable close to grazing (normal) incidence for structures with first- (second-) order mirrors. This may be advantageous over transmission measurements that are made difficult by the length of the structure, when the transmission in the cavity mode is very low owing to diffraction losses.

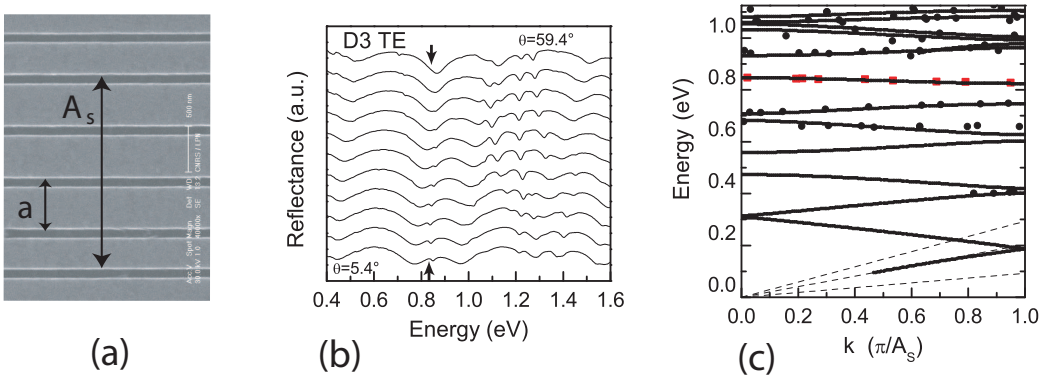

Figure 2.17: (a) SEM image of the defect cavity between 2nd order Bragg mirrors, top view (courtesy of M. Belotti). (b) Experimental variable-angle reflectance spectra on the sample D3 (courtesy of M. Galli); the dispersionless feature marked by the arrows indicates the excitation of the cavity mode. (c) Comparison between calculated bands and experimental points extracted from the VAR spectrum in (b).

Preliminary experimental results

In this brief paragraph, a comparison between GME calculations and preliminary experimental data obtained from SOI 1D photonic crystal slabs with cavities repeated with supercell periodicity is presented. Analogous experiments have been performed in Ref. [22] on GaAs-based systems. The samples are fabricated by increasing or decreasing the Silicon stripe width in one unit of the supercell lattice. The energy position of the cavity mode is sensible to the structural parameters, and thus the fabrication step is a very important one in order to get reliable results. The samples were designed to obtain cavity modes within both first- and second- order Bragg mirrors. Samples with different supercell periodicities (4, 5 and 6 air slits per mirror between two consecutive cavities) have been fabricated.

In Fig. 2.17a a SEM image of one of the measured samples is shown, in particular the sample named D3, with 4 air slits between cavities. The supercell period between the two cavities is indicated and compared to the small period of the surrounding Bragg mirrors. The Bragg mirrors have the same parameters as the 1D photonic crystal slabs whose band dispersion is displayed in Fig. 2.6. Thus, $d = 260$ nm, $a = 560$ nm, air slits width $L_1 = 100$ nm, cavity width $L_{\text{cav}} = 335$ nm. A cavity mode within the second-order band gap is clearly seen in the measured VAR spectrum shown in Fig. 2.17b as a dispersionless anomaly. By extracting the dispersion of

the quasi-guided modes in the $(\mathbf{k}, E)$ plane, a very good agreement between the calculated bands and the measured ones can be observed in Fig. 2.17c. The calculations are made by using the expansion in the guided modes of the effective waveguide with the nominal parameters of the sample. In particular, the energy position of the cavity mode is exactly predicted by our method. Notice that the bands are folded in the reduced Brillouin zone of the superlattice. The fundamental mode of the 1D photonic crystal slab forms small gaps at the zone boundaries and becomes observable in reflectance, while in the periodic system it should lie below the light line and could not be excited by an external beam. This preliminary study is very useful for the design of such cavities also on other materials. A study on the Q-factor of the cavity modes, in particular on the experimental confirmation of the conclusions reported in this Section, is still being completed.

Chapter 3

Two-dimensional photonic crystal slabs

This Chapter deals with the theoretical investigation of two-dimensional (2D) photonic crystal slabs, which are of primary importance for prospective applications of photonic crystals as components of future all-optical integrated circuits. The 2D pattern and the additional confinement provided on the electromagnetic field by the dielectric mismatch along the third direction allow for a complete three dimensional control of light propagation. The great advantage with respect to fully three-dimensionally periodic systems is that 2D photonic crystal slabs exploit the current fabrication technology of Silicon-based integrated circuits. In this work only systems with strong refractive index contrast, such as membrane photonic crystal slabs or SOI structures, are considered. The theoretical approach adopted relies on the Guided-Mode Expansion (GME) method outlined in Sec. 1.2. In the first two Sections the photonic band dispersion of guided and quasi-guided modes in 2D photonic crystal slabs, also with linear defects, will be shown. In Sec. 3.2 comparisons between theoretical calculations and experimental data on linear waveguides in SOI photonic crystal slabs with supercell configuration will be described[1]. These two Sections should be considered as an introduction to Sec. 3.3, in which the systematic study of propagation and out-of-plane diffraction losses of defect modes in 2D photonic crystal slabs with line defects will be presented[2].

[1]Part of these results have been presented in Ref. [53].

[2]Most of the results discussed here have been published partly in Ref. [50] and partly in Ref. [52].

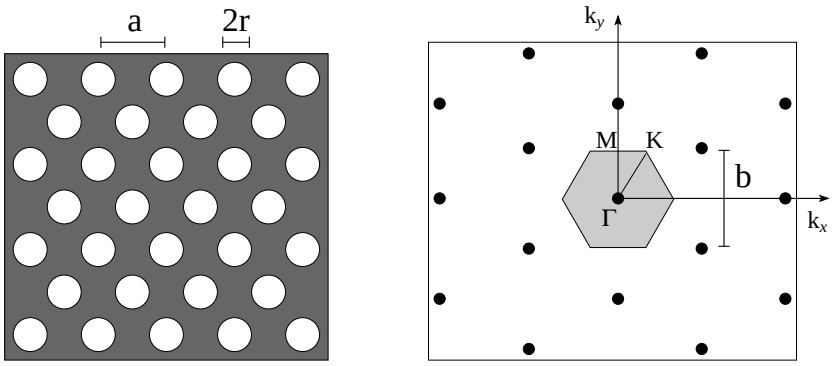

Figure 3.1: (a) Direct and (b) reciprocal lattices for the 2D photonic crystal with a triangular pattern. The dark grey material is assumed to have dielectric constant $\epsilon_{\text{diel}} = 12$, while the white material is air. The shaded region in (b) is the Brillouin zone. The main symmetry points in the irreducible Brillouin zone are also indicated.

3.1 Photonic bands of triangular lattice

The most commonly studied 2D photonic crystal structure is the triangular lattice of air holes, after pioneering papers of the beginning of nineties in which a complete photonic band gap was predicted for in-plane propagation [83, 84]. It should be pointed out that a complete band gap disappears for the analogous waveguide-embedded structure, as discussed in Ref. [46]. In this Section, the dispersion properties of 2D photonic crystal slabs with triangular lattice of air holes are summarized by showing calculations for guided and quasi-guided modes, both in membrane and SOI structures. The present theoretical approach allows for a quick and clear understanding of the dispersion properties, in particular for what concerns the calculation of quasi-guided modes. Theoretical calculations of the whole energy spectrum, that is both below and above the light line, in triangular lattice of air holes of high index contrast planar slabs can be performed by exact methods (but also computationally heavy) such as FDTD [6]. The GME approach has the great advantage of being a plane wave-based method, with a relatively low computational effort required also for more complicated systems. On the other hand, as pointed out in Sec. 1.2, the method is approximate because the basis set chosen for the expansion is not complete. In the calculations shown in this section, convergence was checked and a number of 109 plane waves and 4 guided modes for each parity in the basis set are found to give

stable numerical results in the frequency range considered. The convergence is less accurate when the waveguide is thicker, owing to the presence of many guided modes in the effective slab.

Figure 3.1a displays a top view of the photonic crystal structure considered. In real space, the periodic pattern is defined by a triangular lattice of air holes with lattice constant a and hole radii r. The background dielectric constant is set to the value $\epsilon_{\text{diel}} = 12$, as appropriate for Silicon or GaAs at optical wavelengths. The choice for the primitive lattice vectors is to take $\mathbf{a}_1 = a(1, 0)$ and $\mathbf{a}_2 = a/2(1, \sqrt{3})$, from which the unit cell area is $A_c = a^2\sqrt{3}/2$ and the air fraction $f_{\text{air}} = \pi r^2/A_c = 2\pi r^2/(\sqrt{3}a^2)$. The primitive vectors of the reciprocal lattice can be easily found from Eq. 1.14, resulting in $\mathbf{b}_1 = 2\pi/a(1, -1/\sqrt{3})$ and $\mathbf{b}_2 = 2\pi/a(0, 2/\sqrt{3})$. The reciprocal lattice is displayed in Fig. 3.1b. The shaded area represents the Brillouin zone, reflecting the hexagonal symmetry of the lattice. The main symmetry directions are also indicated. Correspondingly, in real space the ΓK direction is along x and the ΓM is along y.

In Fig. 3.2 a comparison between photonic mode dispersions in the effective uniform slab (Fig. 3.2a), in the 2D photonic crystal membrane (Fig. 3.2b) and in the ideal 2D photonic crystal (Fig. 3.2c) is shown. The main purpose of Fig. 3.2 is to illustrate the differences between the eigenmodes of 2D photonic crystal slabs and the corresponding modes in the two limiting systems, namely a planar waveguide without patterning and a 2D photonic crystal with the same parameters but infinitely extended along the vertical direction. In this case, contrary to 1D photonic crystal slabs, the modes cannot be classified according to mirror symmetry with respect to the plane of incidence, because there are different symmetry directions owing to the 2D pattern. The only symmetry operation (in the case of symmetric planar slab, like the suspended membrane here considered) remains the reflection with respect to the horizontal plane (x, y) bisecting the waveguide. The same symmetry holds for the ideal 2D case considering only in-plane propagation, where the even solutions ($\sigma_{xy} = +1$) are referred to as H-modes (having non-vanishing field components H_z, E_x, E_y) and the odd ($\sigma_{xy} = -1$) are called E-modes (non-vanishing components E_z, H_x, H_y)[3]. In 2D photonic crystal of finite height the modes cannot be classified anymore as purely H or E, because the fields are functions also of the z-coordinate and the eigenmodes generally possess all their vectorial components. However, it makes still sense to define H-like modes and E-like modes the even and odd modes of a 2D photonic crystal slab, respectively. For a more general analysis of

[3]In literature alternative definitions can be found, such as: TE for H-modes and TM for E-modes [5], or p-polarization for H-modes and s-polarization for E-modes.

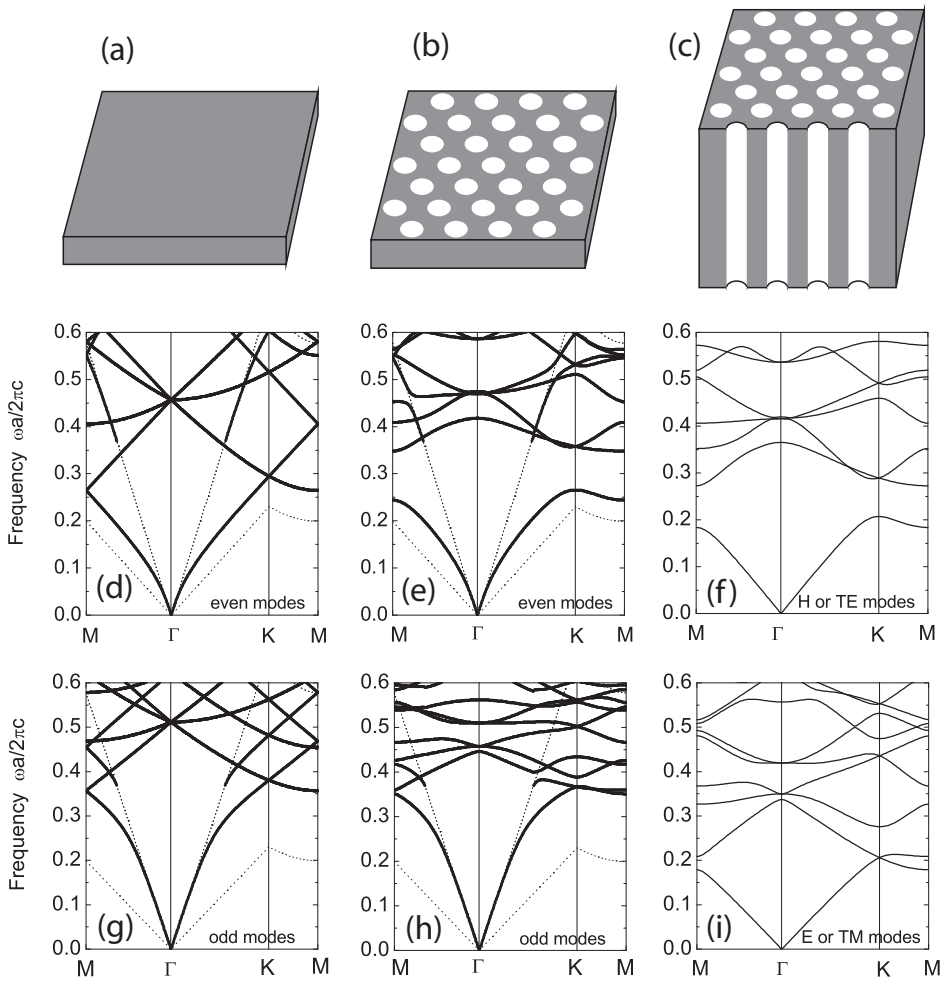

Figure 3.2: Upper panels: schematic pictures of the structures, i.e. (a) uniform planar waveguide suspended in air, (b) 2D photonic crystal membrane with triangular lattice of air holes, and (c) ideal 2D photonic crystal with the same lattice as in (b). (d) Even and (g) odd photonic modes for the uniform slab with effective dielectric constant $\epsilon_{\text{eff}} = 8.4$ and thickness $d/a = 0.5$. Truly guided modes are folded in the BZ of the triangular lattice of air holes assuming a lattice constant a. (e) Even and (h) odd guided and quasi-guided photonic modes for the membrane photonic crystal slab with $r/a = 0.3$ and $d/a = 0.5$. Light lines are represented by dotted lines. (f) H- (even) and (i) E-modes (odd) for a 2D photonic crystal infinitely extended along the vertical direction with $r/a = 0.3$.

2D photonic crystal slabs based on the group theoretical formulation and on the symmetry aspects see Ref. [34].

In Figs. 3.2d (modes with $\sigma_{xy} = +1$) and 3.2g ($\sigma_{xy} = -1$) the dispersion of the guided modes of the uniform planar slab with effective dielectric constant $\epsilon_{\text{eff}} = 8.4$ and thickness $d/a = 0.5$ are plotted in the first Brillouin zone of the triangular lattice with lattice constant a. This is done to understand the origins of quasi-guided modes in a photonic crystal slab. Studying the guided modes of the uniform slab folded in the first Brillouin can also be useful for understanding the symmetry of the resonances excited, e.g., with variable-angle reflectance (VAR) or transmittance. It should be noted that these modes constitute the basis set for the expansion in guided modes of the uniform slab, as it can be recognized by the coincidence of the second-order modes cut-offs in Figs. 3.2d and e and in Figs. 3.2g and h. Because of the use of the reduced zone scheme, some of the folded modes in Figs. 3.2d and g fall above the light cone. These modes, of course, have no radiative linewidth in the homogeneous slab, because the coupling to radiative modes is still forbidden by the continuous translational invariance in the plane of the waveguide. The photonic band dispersion of the photonic crystal membrane (Figs. 3.2e and h) with $r/a = 0.3$ and $d/a = 0.5$ shows notable differences as compared to the effective waveguide. In particular, it displays the opening of band gaps at the main symmetry points, which is more pronounced for even than for odd modes. This is similar to what previously shown for 1D photonic crystal slabs (Sec. 2.1). It is important to consider both guided and quasi-guided modes for the definition of a photonic band gap, as already anticipated in the previous Chapter. A wide band gap is present for even modes, because this allows to obtain defect modes within the gap of a given parity, as it will be described in the next Section.

The photonic bands of the ideal 2D triangular lattice photonic crystal are plotted in Figs. 3.2f and i; they are calculated by using the plane wave expansion method described in Sec. 1.1. They display well known features, such as a photonic band gap between the first and the second band of even (H) modes [5]. A complete band gap for all polarization forms in this 2D photonic crystal for $r/a > 0.4$. As already pointed out, no complete band gap forms in the corresponding finite height system [46]. The main difference as compared to the dispersion of Figs. 3.2e and h is that the bands are lower in energy. In particular, the blue shift of the photonic crystal slab modes, due to the dielectric confinement, is more pronounced for odd modes (this is analogous to 1D systems). The presence of higher order mode cut-offs represents a further important difference of the finite height system as compared to the ideal reference one. It should be noted that the dispersion of photonic crystal slab modes presents, both for even and odd bands,

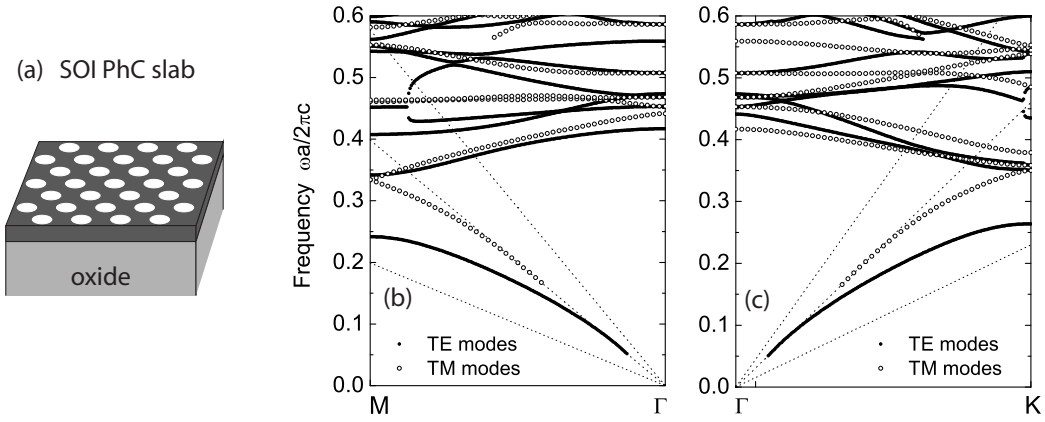

Figure 3.3: (a) Schematic picture of a SOI 2D photonic crystal slab, and photonic band dispersion along the main symmetry directions (b) ΓM and (c) ΓK for a structure with $d/a = 0.5$ and $r/a = 0.3$. For each direction, the modes can be classified as odd ($\sigma_{\mathbf{k}z} = -1$, excited by TE incident light) or even ($\sigma_{\mathbf{k}z} = +1$, excited by TM light) with respect to the vertical plane of incidence. The dielectric constant of the semi-infinite oxide cladding is assumed to be $\epsilon_{\text{oxide}} = 2.1$.

anti-crossings and mini-gaps forming when two photonic modes of different parities are resonantly coupled by the inverse dielectric tensor. Examples of these anti-crossings can be seen, e.g., in Fig. 3.2e when the second-order mode is coupled to a first-order photonic band. The one-to-one correspondence at low frequency between the fundamental mode and the photonic bands of the ideal 2D photonic crystal allows to confirm the H-like (E-like) nature of even (odd) modes in 2D photonic crystal slabs. It is worth reminding, anyway, that the calculations shown in Figs. 3.2e and h come from a 3D formulation, while the ones in Figs. 3.2f and i are 2D. For a thorough analysis of intrinsic diffraction losses of quasi-guided modes in 2D photonic crystal membranes the reader is referred to Ref. [47]. As a final remark, it should be noted that 2D photonic crystal membranes have been fabricated both in Silicon and GaAs layers [12, 24], but mainly for purposes concerning in-plane transmission experiments, owing to the difficulty in fabricating suspended membranes of sufficiently large area. Experiments of variable angle reflectance on 2D photonic crystal membranes have not yet been published, up to now.

In Fig. 3.3 the photonic band dispersion of a SOI photonic crystal slab with analogous parameters as the membrane structure of Fig. 3.2b is presented. The main difference with respect to the photonic band structure

of the symmetric system is that the reflection with respect to the xy plane parallel to the waveguide is no more a symmetry operation of the system (see Fig. 3.3a for a schematic representation of the 2D photonic crystal slab structure). This implies that all the transverse components of the electric and magnetic fields have to be included in the basis set for the solution of the master equation. The only symmetry separation that still holds is the reflection with respect to the plane of incidence, when this is fixed by the specified direction of the exciting plane wave in real space. In this case the photonic modes can be classified as even ($\sigma_{\mathbf{k}z} = +1$) or odd ($\sigma_{\mathbf{k}z} = -1$) with respect to this plane. As these modes are excited, e.g. in a VAR experiment, by TM- or TE-polarized incident beam[4], respectively, this is also the definition used sometimes to classify the modes of 2D asymmetric photonic crystal in literature. Here, the photonic bands are separately calculated for the two symmetry directions ΓM and ΓK (see Fig. 3.1). Even if the SOI structure is not so different from the membrane one, in the sense that there is not much difference between the dielectric constants of air and oxide claddings, the photonic band structure of Fig. 3.3 is very different from Figs. 3.2e and h. The most notable difference is the finite cut-off frequency for the fundamental modes and the removal of degeneracy between odd and even modes cut-offs, in analogy to what previously shown for asymmetric 1D systems. It is worth noting the presence of a wide band gap for both directions in the $\sigma_{kz} = -1$ modes. Defect photonic states can be present in SOI 2D photonic crystal slabs, as it will be shown in the next Section. Finally, it can be seen that some modes change their parity with respect to the plane of incidence on changing the symmetry direction. This is due to the change in the vertical plane of symmetry for the dominant field components of the mode.

3.2 Linear waveguides in triangular lattices

Linear waveguides in photonic crystal slabs are an attractive candidate for the realization of integrated optical interconnects and other photonic devices. Indeed, one of the most attractive features of photonic band gap properties in the last two decades has been the possibility to guide light and to control its propagation properties, besides the control of spontaneous emission first proposed by Yablonovitch [2]. In particular, light propagation can be tailored through the design of defects in the otherwise periodic structure, thereby creating defect states within the photonic band gap. As light confined by

[4]The TE-polarized light beam has its electric field linearly polarized perpendicularly to the vertical plane of incidence, while the TM-polarized one has the electric field in the plane of incidence.

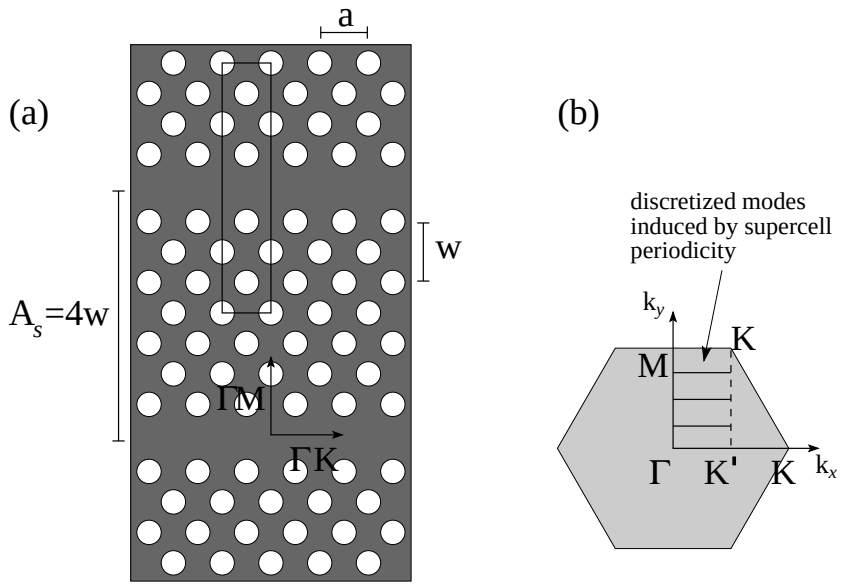

Figure 3.4: (a) Schematic picture of the supercell lattice used for the defect modes calculations. The supercell period along ΓM, the channel width and the elementary cell repeated with supercell periodicity are defined; (b) Brillouin zone of the 2D structure, with the projection and folding induced by the linear defect with supercell repetition.

the gap is not subject (at least in principle) to total internal reflection constrictions, high transmission through sharp bends and very low propagation losses should be achievable in such systems. A linear defect in a 2D periodic systems acts like a waveguide for the electromagnetic field, and it is potentially the basic element of photonic integrated circuits. Such linear defects preserve the periodicity of the 2D pattern only along one direction, yielding a one-dimensional Bloch wave vector. A dispersion relation for these defect states can be calculated within the GME approach, by defining a supercell in the plane of the waveguide. We consider in this section one of the most studied waveguide structure in photonic crystal slabs, namely the one created by filling up a single row of holes along the ΓK direction in a triangular lattice of air holes. We consider both symmetric (membrane) and asymmetric (SOI) slab structures. Comparisons with measured photonic band dispersions will be shown for SOI waveguides.

In Fig. 3.4a a schematic view of the supercell considered for calculations is shown. The waveguide is defined by removing a row of holes, the channel width is $w = w_0 = \sqrt{3}a$, that is the distance between the centers of two holes placed at the channel sides. This system is typically called a *W1 waveguide*.

The presence of the waveguide breaks the periodicity along the ΓM direction, but the system is clearly periodic (with lattice constant a) along the waveguide channel. The spacing between two consecutive channels in the super-lattice is defined by the supercell period A_s. Since a guided mode has exponentially decaying (evanescent) fields in the direction perpendicular to its Bloch wave vector, no overlap occurs between the guided modes of adjacent waveguides if A_s is sufficiently large. This way, the calculated dispersion of the guided mode will coincide to the one of a single linear waveguide. A similar principle has been used for the calculations of defect modes in 1D photonic crystal slabs in the previous Chapter[5]. Considering the elementary cell defined in Fig. 3.4a, this is repeated with a periodic rectangular lattice of primitive vectors $\mathbf{a}_1 = a(1,0)$ and $\mathbf{a}_2 = A_s(0,1)$. The dielectric matrix in Fourier space can be obtained by the Fourier transformation of a single hole multiplied by a structure factor, which depends on the elementary cell (see appendix for the Fourier transform of the linear defect). The Brillouin zone of the lattice of Fig. 3.4a is displayed in Fig. 3.4b. Owing to the supercell periodicity along ΓM, the reciprocal lattice is projected onto ΓK. Thus, K′ becomes the boundary of the first Brillouin zone in the projected lattice. The number of discretized bulk modes that are folded in the ΓK′ direction depends, of course, on the supercell period A_s[6]. In the limit of very large A_s the projected bands tend to a continuum of modes, which represent also the continuum of folded modes for a single, isolated linear defect. For this reason these modes are usually represented by a shaded area in the first Brillouin zone of the defect lattice. The length of the ΓK′ direction is π/a.

After the definition of direct and reciprocal lattices and the calculation of the Fourier transform of the dielectric function for the elementary cell of Fig. 3.4a, the GME method can be easily applied to calculate the dispersion relation of the defect modes along ΓK′. In Fig. 3.5 the photonic band structure for a W1 linear waveguide in a membrane 2D photonic crystal slab is shown. The slab thickness is $d/a = 0.5$ and the hole radius is $r/a = 0.3$. Since the waveguide is symmetric with respect to its vertical axis, that is with respect to the plane of incidence (x, z), the guided modes can be classified as even ($\sigma_{kz} = +1$) of odd ($\sigma_{kz} = -1$) with respect to this plane. Moreover, owing to the symmetry of the waveguide with respect to the horizontal midplane, the modes can also be classified as even or odd with respect to $\hat{\sigma}_{xy}$ symmetry operation. We consider here only guided modes of the even $\hat{\sigma}_{xy}$ parity, because

[5]Normally, in the calculations shown here a supercell period $A_s = 5w_0$ is largely sufficient to recover the correct dispersion relation for the guided modes.

[6]This phenomenon is conceptually similar to the formation of sub-bands in solid state superlattices for what concerns electronic energy states, or to the folding of acoustic phonons in semiconductor superlattices that makes them visible in optical spectra.

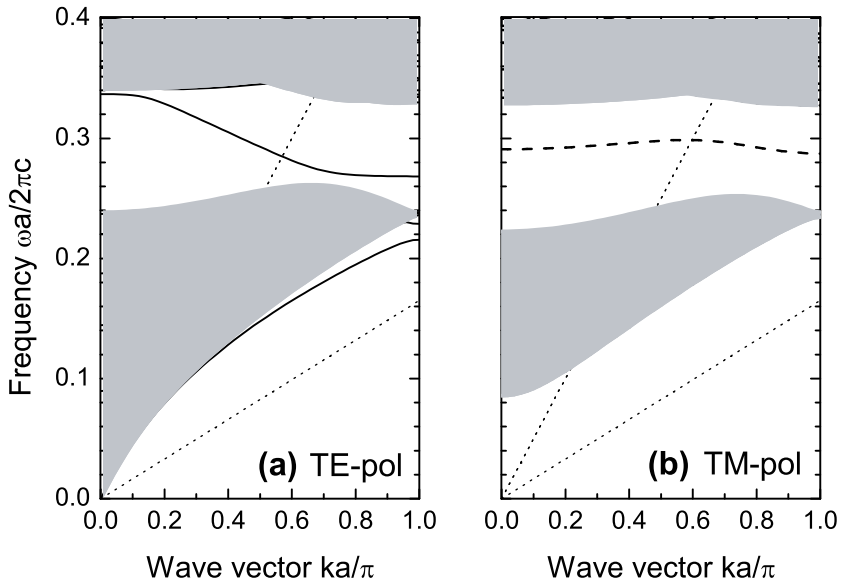

Figure 3.5: Photonic dispersion of (a) odd ($\sigma_{kz} = -1$) and (b) even ($\sigma_{kz} = +1$) modes for a W1 linear waveguide in a membrane of thickness $d/a = 0.5$. The hole radius is $r/a = 0.3$. Only even modes with respect to the slab plane are considered ($\sigma_{xy} = +1$). The grey areas correspond to folded modes of the triangular lattice.

the corresponding photonic band dispersion for the triangular lattice has a complete band gap (see, e.g., Fig. 3.2e). In Fig. 3.5 the dispersions of odd (a) and even (b) modes with respect to the plane of incidence are plotted[7]. The shaded regions represent the photonic modes of the triangular lattice of air holes projected in the Brillouin zone of the defect lattice (see Fig. 3.4b). For these calculations, a supercell period $A_s = 4\sqrt{3}a$ along ΓM has been used, and 181 plane waves that are largely sufficient for convergence. The discretized bands have been obscured in order to represent the dispersion of a single linear defect. The width of the band gap is the one of the corresponding triangular lattice. The guided modes display known features and will not be commented extensively here [29, 44]. It should be noted, however, that two kinds of guided modes can be present in a line-defect photonic crystal slab, namely *index confined* and *gap confined* modes. The latter can exist

[7]The defect mode shown in Fig. 3.5a is globally odd ($\sigma_{kz} = -1$), but its dominant field components are spatially even with respect to the vertical midplane kz bisecting the waveguide channel. That is why in the literature it is sometimes indicated as the *even* mode. The definition discussed in the text is considered the most appropriate here, from the point of view of parity symmetry.

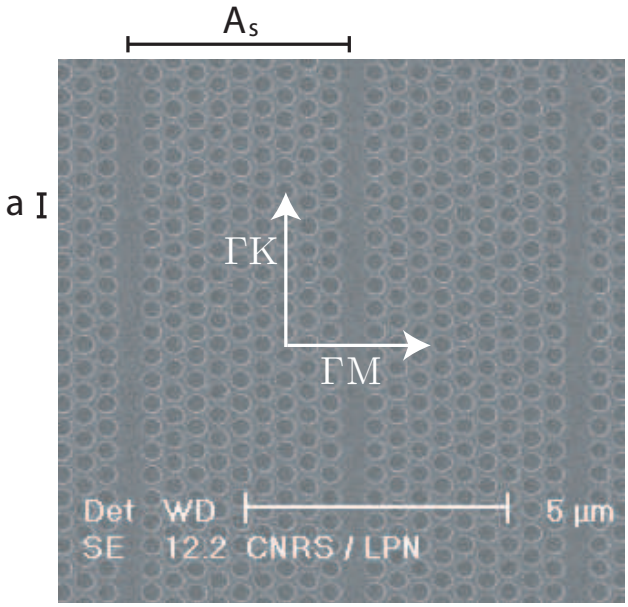

Figure 3.6: SEM image of one of the measured samples, in particular the one with supercell period $A_s = 5\sqrt{3}a$ along ΓM (courtesy of M. Belotti). Nominal parameters of the sample are: $d = 260$ nm, $a = 500$ nm, $r/a = 0.35$.

only as a consequence of the photonic band gap properties of the surrounding periodic lattice. Referring to Fig. 3.5, the TE defect mode within the band gap is partly index confined (high group velocity region) and partly gap confined (final region below the light line), while the TM mode is a gap confined one. Notice also that as the waveguide is symmetric the fundamental guided mode has no cut-off, and thus its dispersion starts at $\omega = 0$ (see Fig. 3.5a). Moreover it lies below the 2D lattice projected modes before being folded back at the Brillouin zone edge, because it starts as an index confined mode and it is guided in a region of higher dielectric constant than the effective planar waveguide. For experimental results concerning guided modes in 2D photonic crystal Silicon membranes we refer to Refs. [25, 85], and in GaAs membranes to Ref. [86].

Silicon-on-Insulator systems represent the most valid proposal for prospective applications of photonic crystal waveguides in integrated optics. For this reason W1 waveguides in SOI slabs have been the subject of intensive both theoretical [30, 87] and experimental [88] works. In order to illustrate here the dispersion properties of SOI-based 2D photonic crystal slabs with linear defects, a comparison between experiments realized at the optical spectroscopy laboratory of the Department of Physics "Alessandro Volta," University of

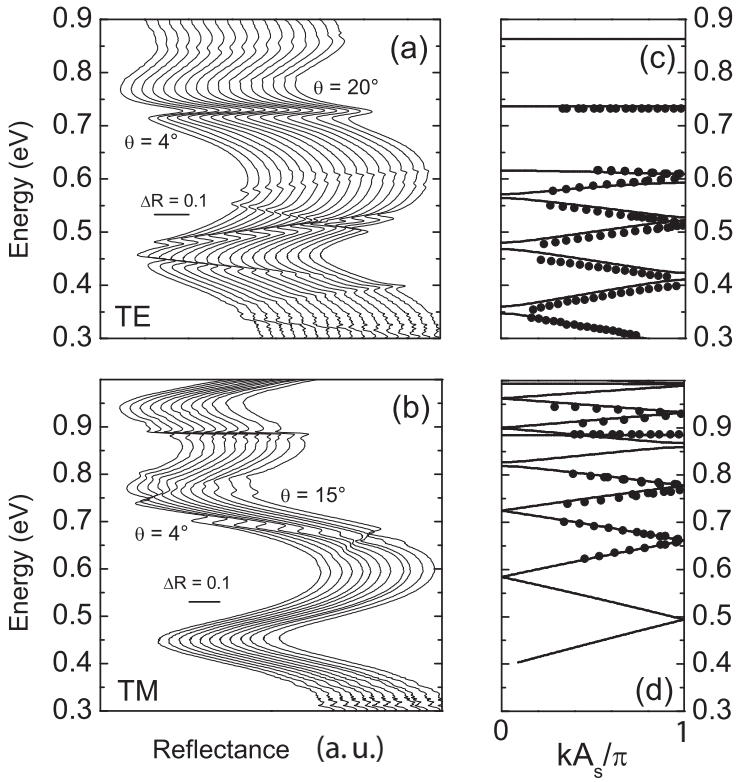

Figure 3.7: VAR spectra along ΓM for (a) TE and (b) TM-polarization on the sample of Fig. 3.6. The curves are slightly shifted for clarity. (c) and (d) corresponding photonic bands folded in a reduced Brillouin zone due to supercell periodicity: experiment (points) and GME calculations (lines).

Pavia, and theoretical calculations by the GME method is presented. Patterned waveguides containing W1 linear defects repeated with supercell periodicities $A_s = m\sqrt{3}a$ (with $m = 4, 5, 6$) were fabricated at the "Laboratoire de Photonique et Nanostructure," of the CNRS, Paris-Marcoussis, France. Here we consider the sample with $A_s = 5\sqrt{3}a$, whose picture is shown in Fig. 3.6. Details on the fabrication procedure (namely electron beam lithography and reactive ion etching) are given elsewhere [21]. The supercell structure of the samples has allowed for the first time the experimental determination of the photonic band dispersion in linear defect waveguides on SOI slabs by using the VAR technique, see also Ref. [53].

In Figs. 3.7 the reflectance spectra along the ΓM orientation of the sample of Fig. 3.6, that is perpendicular to the line-defect, are shown for (a) TE- and (b) TM-polarized incident light. The well defined resonant features

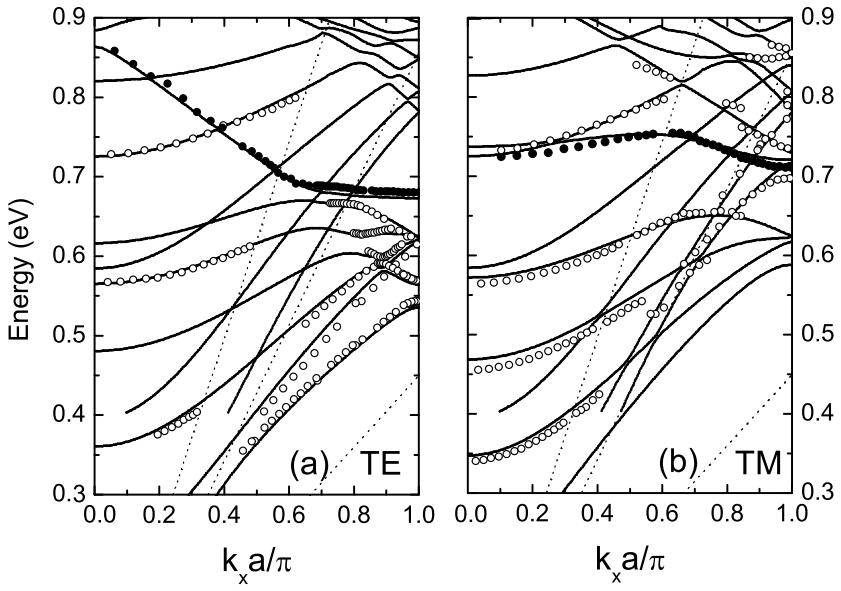

Figure 3.8: (a) TE- and (b) TM-polarized photonic modes measured (closed points for the defect modes, open circles for the 2D photonic crystal bands) on the sample of Fig. 3.6 along the ΓK orientation. Calculated data (lines) are obtained by the GME approach.

in the spectra mark the excitation of quasi-guided modes of the patterned waveguide. The dispersion of such modes is extracted from these spectra and compared to theoretical calculations in Figs. 3.7c and d. The excitation of cavity modes at 0.73 and 0.89 eV respectively for (c) TE- and (d) TM-polarized modes is evidenced by a flat dispersion, while the bulk photonic crystal modes are characterized by a much stronger dispersion as a function of the wave vector in units of the supercell period π/A_s. The results shown in Fig. 3.7 are similar to those of Fig. 2.17. The supercell along ΓM act as a repetition of Fabry-Pérot cavities in waveguide geometry, very much like the systems studied in Sec. 2.4. Very good agreement between measured and calculated photonic bands is found, in particular for what concerns the defect mode energy. The fundamental mode of the 2D photonic crystal slab forms small gaps at the zone edges and becomes observable in reflectance. Mini-gaps of ~ 0.01 eV are predicted by the theory and actually observed in the experiment.

The photonic band dispersion of the photonic crystal waveguide along the ΓK direction is shown in Fig. 3.8a and b for TE and TM polarization, respectively. It should be noted that the wave vector range of measured data

has been greatly increased in this case, thanks to the use of both VAR and ATR techniques [53], see also App. A. The data plotted in Figs. 3.7 and 3.8 represent a complete experimental characterization of W1 defect modes over the whole irreducible Brillouin zone, which has been obtained thanks to the combination of VAR and ATR spectra (not shown here). The agreement between measured data and theoretical calculations is very satisfactory, both for truly guided and quasi-guided photonic modes. The photonic modes of the bulk 2D triangular lattice discretized and folded in the reduced Brillouin zone due to periodic repetition of the W1 defect along ΓM are clearly visible in the experimental spectra (not shown) and compare favorably well with calculations. Owing to the asymmetry of the system, all photonic modes are present and no complete band gap is found. Contrary to W1 waveguides in photonic crystal membranes, the region of the $(\mathbf{k}, E)$ plane of mono-mode propagation for the defect mode is limited to a small area below the SiO_2 light line (e.g. the region around 0.7 eV at large wave vectors in Fig. 3.8a). This is one of the main limitations to prospective applications of these interesting systems. Another drawback is the problem of diffraction losses, which is a very important one and will be addressed in the next Section. As a final comment, it is worth reminding that the theoretical calculations shown in Figs. 3.7 and 3.8 have been carried out by using nominal parameters of the measured sample. Moreover, in order to better reproduce experimental data, the radius of the holes adjacent to the waveguide channel has been reduced by 10%. In particular, the lattice constant was precisely measured with diffraction techniques and gave a value of $a = 502 \pm 1$ nm. The slab thickness was set to the value $d/a = 0.52$, the hole radius was taken as $r/a = 0.34$, and the adjacent holes radii $r'/a = 0.306$. A number of 193 plane waves and 8 guided modes were taken in the basis set for the GME calculations of photonic modes. This model takes into account that in the electron beam lithography process the holes adjacent to the W1 channel receive a lower dose of electrons, and thus their radius should result reduced of about 6-10%[8]. The theoretical model reproduces very well experimental data for both polarizations by using the following values for the dielectric constants of Si and SiO_2: $\epsilon_{Si} = 12$, $\epsilon_{SiO_2} = 2.1$. These values are valid for the corresponding materials at wavelengths around 1.5 μm, close to the defect mode dispersion. Anyway, the whole energy spectrum seems to be reproduced very well. The very small remaining discrepancies (~ 0.008 eV) should be attributed to the energy dispersion of the dielectric constants, which was not included in these calculations.

[8] M. Belotti, private communication.

3.3 Disorder-induced losses in photonic crystal waveguides

In photonic crystal slabs with strong refractive index contrast, like the suspended membrane or *air bridge* and the SOI system, the defect mode associated with the linear waveguide may lie partly below the cladding light line in the ($\mathbf{k}$,ω) plane, as shown in the previous Section. In this case the mode is truly guided with no intrinsic diffraction loss (unlike modes above the light line, which are subject to intrinsic out-of-plane losses). In such a situation, the propagation loss of a guided mode depends exclusively on the presence of structural imperfections. The *role of disorder* on propagation losses is therefore a crucial issue for prospective applications of linear photonic crystal waveguides to integrated optics. The main question that has been arising among researchers in the last few years concerns the effective advantages brought by the photonic crystal waveguides over common strip dielectric waveguides (that is rectangular waveguides of Silicon stripes on SiO_2 substrates), in which propagation losses of the order of 0.1 dB/mm or less have been demonstrated for transmitting wavelengths at the micron scale [89, 90, 91]. Experimental losses measured in W1 waveguides on membrane structures are still too large as compared to these values, even if the fabrication steps have reached a high level of accuracy nowadays [25, 85, 86]. Until now, however, no theoretical approach has been able to produce predictive results to study this crucial issue, even by using exact numerical methods such as the 3D FDTD. A reliable theoretical tool would be able to predict if structures with losses comparable to strip waveguides could be fabricated in photonic crystal slab waveguides, in particular estimating the role of fabrication inaccuracy on the scattering losses. The present Section is a first important step towards the answer to this question.

A systematic theoretical analysis of the effects of disorder on propagation losses in 2D photonic crystal slabs with line defects is presented here. We focus on the W1 waveguide. The main purpose is to quantify the trends of disorder-induced losses as a function of various structure parameters and to analyze the differences between air bridge and SOI photonic crystal slabs. Previous studies of disorder phenomena in photonic crystal slabs concentrated on the effects on the photonic gap [92] or on the consequences of a non-vertical shape of the holes for propagation losses [93]. Recently, the effects of scattering at sidewall roughness in photonic crystal slabs were studied in a two dimensional model [94]. In this work we consider the variation of hole radii as the main disorder effect. It should be noted that the present fully 3D results extend those of Ref. [48], where only intrinsic losses above

the light line were calculated and the effect of disorder was not included. After discussing the numerical results, we compare with recent experimental measurements of losses below the light line made on Silicon W1 waveguides in an membrane structure [85].

We consider a W1 waveguide in a photonic crystal membrane structure. After the calculation of photonic eigenmodes (see last Section), the coupling to radiative modes of the effective waveguide is taken into account by time-dependent perturbation theory, as described in Sec. 1.2. The effects of disorder are accounted for by defining a large supercell in the direction parallel to the line defect, in which the hole radii are randomly distributed with Gaussian probability around an average value r, as discussed in details in paragraph 1.2.2. The root mean square deviation Δr of the hole radius is taken as disorder parameter. As previously pointed out, the random variation of the hole size changes the dielectric modulation to $\epsilon_{\text{dis}}(\mathbf{r})$, and gives rise to a perturbation $\Delta\epsilon(\mathbf{r})$ that couples guided and radiative eigenmodes and leads to a finite $\text{Im}(\omega)$ also for truly guided modes. The supercell along ΓK used to model the disorder has typically a size of $39a$. It is worth noting that the use of this supercell does not require increasing the number of plane waves in the basis set for the expansion, since disorder-induced scattering is treated by perturbation theory. We typically use up to 461 plane waves and two guided modes in the basis set for air bridge structures, taking advantage of horizontal mirror symmetry of the slab. The number of guided modes is doubled in the case of SOI. The calculations employ a supercell in the direction ΓM perpendicular to the line defect and an average over the results with supercell widths from $3w_0 + w$ up to $8w_0 + w$ is taken in order to smooth out finite supercell effects, like in Ref. [48]. Moreover, all loss results presented here include an average over calculations with six different random distributions corresponding to the same disorder parameter $\Delta r/a$, that is different Gaussian distributions with the same r.m.s. deviation. The propagation losses are obtained as

$$\alpha(\mathbf{k}) = 2\,\text{Im}(\mathbf{k}) = 2\,\text{Im}(\omega_{\mathbf{k}})/v_g \ , \tag{3.1}$$

where

$$v_g = |\mathbf{v}_g(\mathbf{k})| = |\nabla_{\mathbf{k}}\omega_{\mathbf{k}}| \tag{3.2}$$

is the modulus of the group velocity at the corresponding wave vector and frequency. The losses in dB are given by $4.34 \cdot 2\text{Im}(\mathbf{k})$.

In Fig. 3.9 the dispersion, the imaginary part of frequency and the propagation losses of the defect mode are plotted for different values of $\Delta r/a$ and frequencies within the photonic band gap. Parameters of the structure are summarized in the caption. Only the defect mode that is even with respect

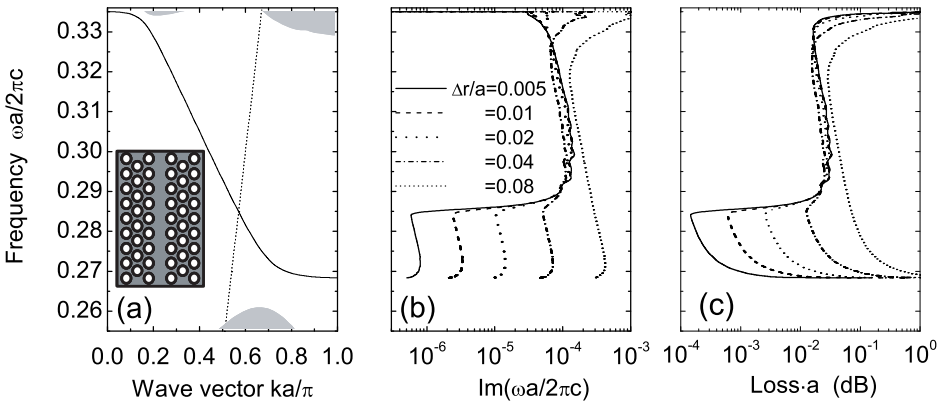

Figure 3.9: (a) Dispersion of the defect mode, (b) group velocity, and (c) propagation loss for different values of the disorder parameter, $\Delta r/a$. Parameters of the W1 air bridge structure are: $r/a = 0.28$, $d/a = 0.5$, $\epsilon = 12$. Shaded regions in (a) represent the modes of the bulk lattice.

to the horizontal midplane ($\sigma_{xy} = +1$) and odd with respect to the plane of incidence ($\sigma_{kz} = -1$, i.e. excited by TE-polarized light) is considered. The shaded regions in Fig. 3.9a represent the bulk photonic crystal modes, as explained in the previous Section. As it can be seen from Figs. 3.9b and c, the defect mode is subject mainly to intrinsic losses when its dispersion falls above the air light line [48]. When the mode crosses the light line, $\mathrm{Im}(\omega a/2\pi c)$ has a sudden decrease towards finite values, due to the disorder-induced losses. The imaginary part of mode frequency depends strongly on the disorder parameter of the structure. In particular, it is found to grow almost quadratically with Δr, as appropriate for a Rayleigh scattering mechanism, that is an elastic scattering mechanism in the perturbative limit. The same quadratic behavior is reflected by the losses in dB, whose divergence at low frequency is determined by the group velocity of the defect mode that tends to zero at the zone edge. The propagation losses are minimal at the crossing between the defect mode an the air light line, where the group velocity is still high, and increase very rapidly on decreasing frequency. The extrinsic losses become important also above the light line for sufficiently high values of the disorder parameter ($\Delta r/a = 0.08$ in this case), or in the energy window of low group velocity, i.e. for $\omega a/2\pi c > 0.33$ in the Figure. The conclusion from Fig. 3.9 is that small advances in the fabrication accuracy could lead to sensible lowering of these losses, owing to their quadratic dependence on the degree of disorder.

In Fig. 3.10 the dependence of the extrinsic losses as a function of the

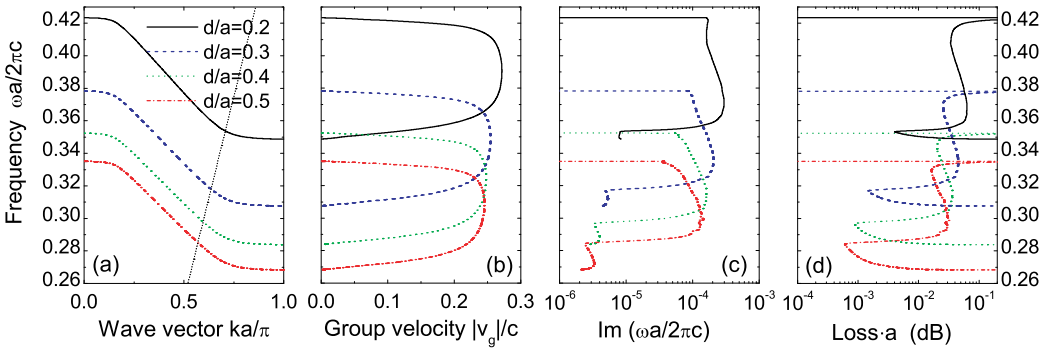

Figure 3.10: (a) Dispersion of the defect mode, (b) group velocity, (c) imaginary part of frequency, (d) propagation loss for different values of the slab thickness, d/a. Structural parameters of the W1 waveguide are: $r/a = 0.28$, $\Delta r/a = 0.01$, $\epsilon = 12$.

core thickness d/a is displayed for $r/a = 0.28$ and $\Delta r/a = 0.01$, which is a typical value in realistic structures. In Fig. 3.10a the dispersion of the defect mode is plotted over the whole Brillouin zone for different values of the slab thicknesses, and it is seen that increasing the confinement of the field in the high dielectric region the frequency of the mode decreases. The dispersion of the mode itself is red-shifted remaining almost unchanged, as it can be seen also from the curves of the group velocity in Fig. 3.10b. The red-shift causes the defect mode to lie below the air light line for a larger frequency window, and particularly to cross the light line with higher group velocity. This is important not only because of the larger band-width accessible for guiding signals, but also because the higher is the group velocity the lower is the propagation loss. This is confirmed by the results shown in Figs. 3.10c and d. It is known that the increased confinement of the field within the high dielectric region coming from an increasing of the core thickness d leads to a decrease of the imaginary part of mode frequency, as first pointed out in Ref. [48]. This behavior is seen to hold for what concerns both intrinsic and extrinsic losses from Fig. 3.10c. In Fig. 3.10d the propagation losses in dB confirm the trend previously outlined; in particular, is important to see that the $d/a = 0.5$ W1 waveguide is preferable not only for the lowest losses, but also for the largest transmission band-width. As a final remark concerning this Figure, it is worth noting that the imaginary part (and the losses, too) go to zero at the Γ point, that is at $\mathbf{k} = 0$.

In Fig. 3.11 the dispersion, the group velocity, the imaginary part and the propagation losses are plotted for frequencies within the photonic band

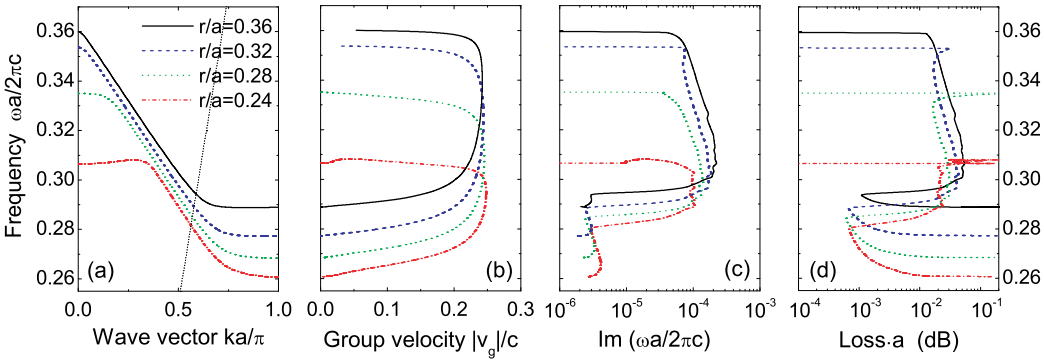

Figure 3.11: (a) Dispersion of the defect mode, (b) group velocity, (c) imaginary part of frequency, (d) propagation loss for different values of the hole radii r/a. Structural parameters of the W1 waveguide are: $d/a = 0.5$, $\Delta r/a = 0.01$, $\epsilon = 12$.

gap with decreasing values of the hole radius, and $d/a = 0.5$. The disorder parameter is again assumed to the value $\Delta r/a = 0.01$. The mode frequencies decrease on decreasing the hole radius, because of the reduced air fraction in the effective planar slab. Compared to Fig. 3.10a the dispersion curves plotted in Fig. 3.11a show notable changes on changing the hole radius. In fact, decreasing the air fraction higher order modes fall within the band gap, and the defect mode is mixed to other modes within the band gap. Our analysis can be limited, in the present case, to the part of the defect mode lying below the light line, which is the most interesting region for prospective applications. Again, on decreasing the mode frequency, a wider band falls below the air light line. It is surprising to see from the results of Figs. 3.11c and d that the lower air fraction does not always implies lower imaginary part and extrinsic losses for the defect mode, as it would have been expected from previous analysis. In fact, the intrinsic losses above the light line increase on increasing the hole radius, as recently reported in Ref. [48], while the extrinsic ones are $\sim 3 \cdot 10^{-6}$ and have a much weaker dependence on this parameter. These numerical results can be explained by considering that extrinsic losses depend mainly on $\Delta r/a$, while intrinsic out-of-plane diffraction of quasi-guided modes is determined by the leakage of the field. It is not intuitive, in this context, that disorder-induced losses have a weaker dependence on the air fraction than intrinsic ones. In Fig. 3.11d the propagation loss in dB is plotted, which displays the expected behavior of decreasing for decreasing hole radius in the frequency region of truly guided photonic modes. This behavior is mainly determined by the corresponding

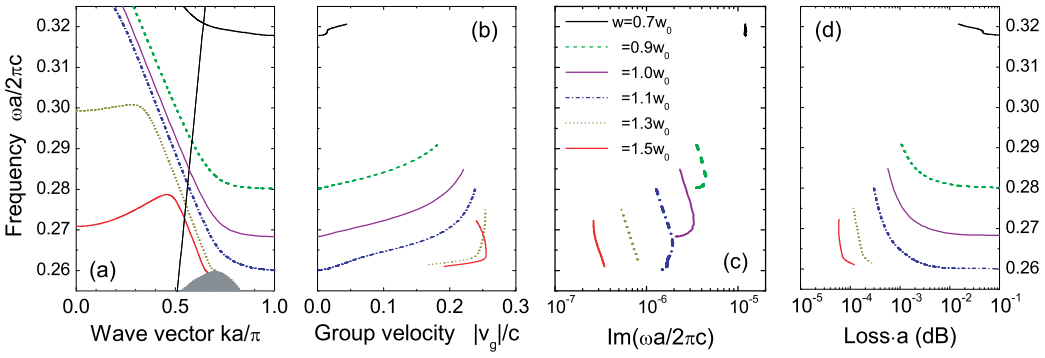

Figure 3.12: (a) Dispersion of the defect mode, (b) group velocity, (c) imaginary part of frequency, (d) propagation loss for different values of the channel width w. Structural parameters of the 2D photonic crystal air bridge are as in Fig. 3.9, $\Delta r/a = 0.01$. The results are shown only between the lower band edge and the crossing with the light line.

group velocity (see Fig. 3.11b), which is higher at the crossing point between the defect modes and the air light line when the air fraction is decreased.

In Fig. 3.12 we show the defect mode dispersion, group velocity, imaginary part of frequency and propagation losses for waveguides with channel thickness w ranging from $0.7w_0$ to $1.5w_0$. The channel width w equals $w_0 \equiv \sqrt{3}a$ if the positions of the surroundings holes are fixed to those of the triangular lattice, but waveguides with reduced or increased channel widths have also been realized and tested [25, 88]. The frequencies of the defect mode decrease on increasing the channel width: moreover, the dispersion is modified in such a way that the group velocity at the crossing point with the light line increases and takes a maximum value close to $c/n \simeq 0.25$ for waveguides with the largest values of w[9]. The results of Fig. 3.12c and d, which assume a disorder parameter $\Delta r = 0.01a$, can be scaled to other values of Δr by using the quadratic dependence previously discussed. The imaginary part of the frequency shown in Fig. 3.12c decreases rapidly for increasing channel thickness: this behavior, which is similar to the one occurring above the light line for the intrinsic out-of-plane losses [48], follows from increasing localization of the electromagnetic field in the dielectric (channel) region where it is less affected by fluctuations of the hole diameter. As a consequence of both the lower $\mathrm{Im}(\omega)$ and the higher v_g, the propagation loss shown in Fig.

[9]Reduced-width waveguides with large group velocity have been demonstrated [25]: however, the mode considered in Ref. [25] is not the one shown in Fig. 3.12, but rather a lower one at frequencies lying close to the band edge.

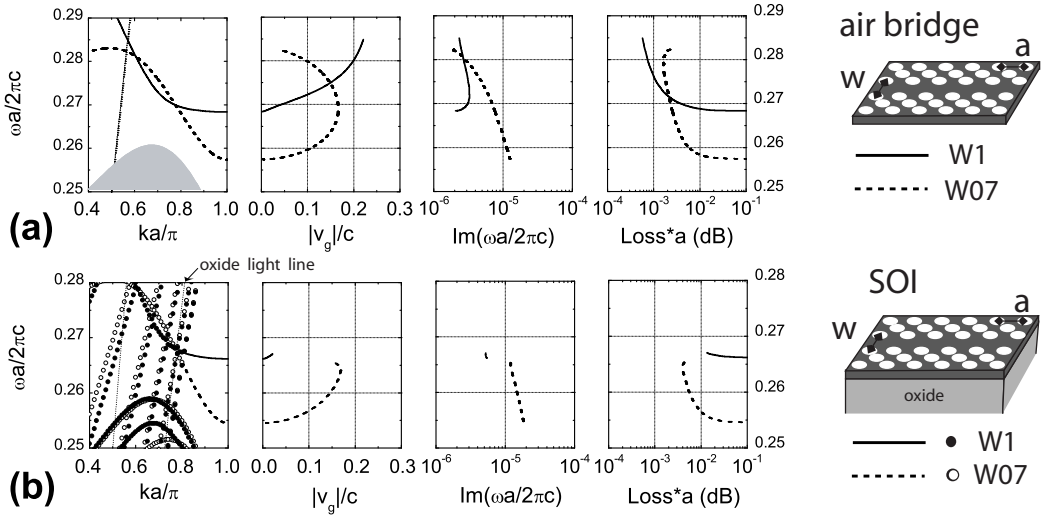

Figure 3.13: Comparison between W1 (full lines and solid circles) and W07 (dashed lines and open circles) linear waveguides in membrane and SOI structures, respectively. (a) Dispersion of the defect mode, group velocity, imaginary part of frequency and losses (dimensionless losses, $\alpha \cdot a$ in dB or α in dB per lattice constant) for an air bridge photonic crystal waveguide with $r/a = 0.28$, $d/a = 0.5$, $\Delta r/a = 0.01$; (b) same quantities for a SOI-based photonic crystal waveguide with identical structure parameters. A dielectric constant $\epsilon_{\text{oxide}} = 2.1$ was used for the SiO_2 substrate. The results for group velocity, imaginary part of frequency and losses are plotted only in the energy range for which the defect mode lies below the light line (or below the parity mixing region, for SOI).

3.12d is minimum for channel thickness $w = 1.5w_0$. By considering also the spatially odd defect mode (calculations not shown here), it can be shown that the waveguide with $w = 1.5$ is truly monomode. The minimum loss $\sim 6 \cdot 10^{-5}$ in dimensionless units becomes about 0.15 dB/mm when divided by a lattice constant $a = 420$ nm (for a working wavelength $\lambda = 1.55\,\mu$m). Thus, we predict that propagation losses ~ 0.15 dB/mm can be obtained in waveguides with state-of-the-art values for the roughness ($\Delta r = 4$ nm), by increasing the channel thickness to $w = 1.5w_0$. We notice that such losses are comparable to those of Silicon wires in the monomode region [91].

Finally, in Fig. 3.13 we show a comparative analysis of mode dispersion, group velocity, imaginary part of frequency and losses below the light line both in air bridge and SOI configurations, for channel widths $w = w_0$ (W1) and $w = 0.7w_0$ (W07 waveguide). Again, only modes with $\sigma_{xy} = +1$ and

$\sigma_{kz} = -1$ symmetries are considered for the air bridge. For SOI systems, the reflection through the plane xy is not a symmetry operation, and thus both parities must be considered in the basis set. Nevertheless, there is a region below the light line in the k-ω plane where no parity mixing occurs [30, 87, 93]. We can see from Fig. 3.13 that $\mathrm{Im}(\omega a/2\pi c)$ is generally larger in SOI systems, due to the asymmetric slab configuration. Looking at the dependence on channel width, the out-of-plane losses are lower for W1 than for W07 in air bridge structures, while in SOI the W07 waveguide has lower losses owing to the larger group velocity of the mode at the crossing point with the SiO_2 light line [87]. This explains the experimental situation according to which W1 waveguides are commonly addressed in Silicon membranes [85], while W07 waveguides have lower propagation losses in SOI structures [88]. The parameters used in these calculations are close to the ones of SOI structures fabricated and studied in Ref. [88]. By using $a = 390$ nm and $\Delta r \simeq 4$ nm, the present results (minimum loss around 9 dB/mm for W07 SOI waveguides, see last panel in Fig. 3.13b) agree well with the experimental value of 6 dB/mm [88].

It is worth concluding this paragraph with some final comments about the numerical results shown. The dependence of extrinsic losses on the main structural parameters can be summarized in the fact that the channel width is the main tuning length allowing for a reduction of propagation losses by orders of magnitude, at fixed disorder parameter (i.e. fabrication accuracy). Thus, the main conclusion is that propagation losses comparable to state-of-art strip waveguides are theoretically achievable with increased width photonic crystal waveguides. Finally, the comparison between membrane and SOI structures has shown that increased width waveguides display the lowest losses for symmetric structures, while reduced-width channels should give better performances for asymmetric structures like SOI.

Comparison with available experiments

In this paragraph the theoretical model proposed for disorder-induced losses in photonic crystal waveguides is put on a solid basis by comparing with recent experimental results obtained on W1 waveguides in Si membranes [85]. Experimental determinations of propagation losses in photonic crystal waveguides are very difficult, especially on a membrane structure. The main difficulty, besides the fabrication step, is the coupling of incident light to the channel in photonic crystal waveguide. The most recent published results concern the use of the so called *cut-back* method to determine the value of the losses (with about 10% accuracy) in photonic crystal slab with line defects in Silicon [85] and GaAs [86] air bridges. Briefly, the cut-back technique

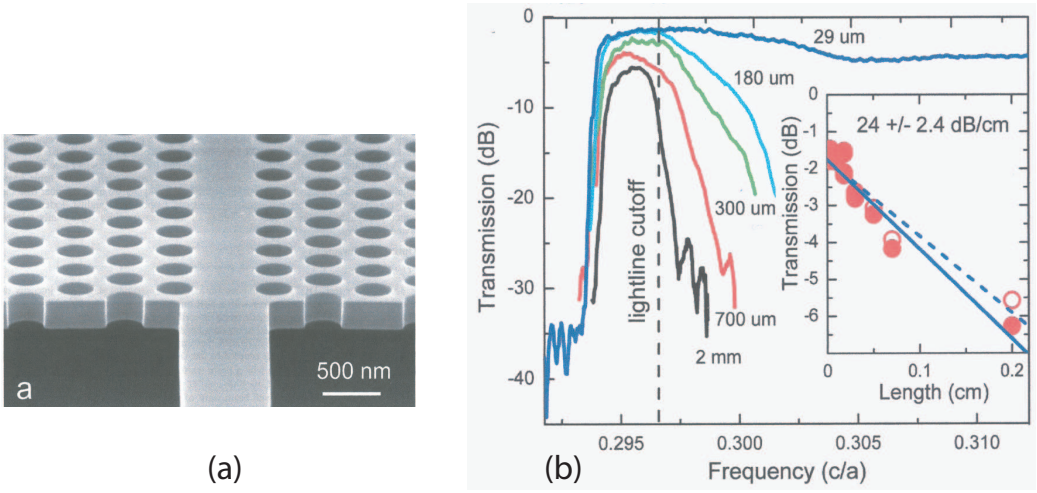

Figure 3.14: (a) SEM image of a photonic crystal membrane and (b) experimental transmission spectra for TE polarization of photonic crystal waveguides with different lengths. The inset shows the cut-back method. These figures are taken from Ref. [85]. Nominal sample parameters are $d = 220$ nm, $a = 445$ nm, $r/a = 0.37$, $\Delta r = 5$ nm.

consists in measuring transmission spectra (normalized to a reference frame) in samples of different lengths, and extracting the losses in dB/mm from the interpolation of measured data.

In Fig. 3.14a an example of a high-quality sample measured in Ref. [85] is shown. It consists of a linear W1 defect in a triangular lattice of air holes with $r/a = 0.37$ and $a = 445$ nm, patterned on a Silicon suspended membrane of thickness $d = 220$ nm. The quoted sidewall surface roughness in the paper by McNab *et al.* is of the order of 5 nm, and it is considered the main source of scattering loss of the propagating Bloch wave below the light line. This is, as previously explained, a crucial issue to obtain very low values for the losses. In Fig. 3.14b the measured transmission spectra on the different length samples is shown (taken from Ref. [85]). The incoming beam is TE-polarized in the experiment, and the spectral range covers the width of the guided mode of the photonic crystal waveguide. In the inset the corresponding attenuation of the light intensity at 1505 nm is displayed for the different length samples. From this experimental analysis a value of 2.4 dB/mm has been extracted with 10% error accuracy. For details concerning fabrication process, experimental set-up, and analytical models used to extract the propagation losses the reader is referred to Ref. [85].

In Fig. 3.15 the theoretical results obtained by assuming the experimen-

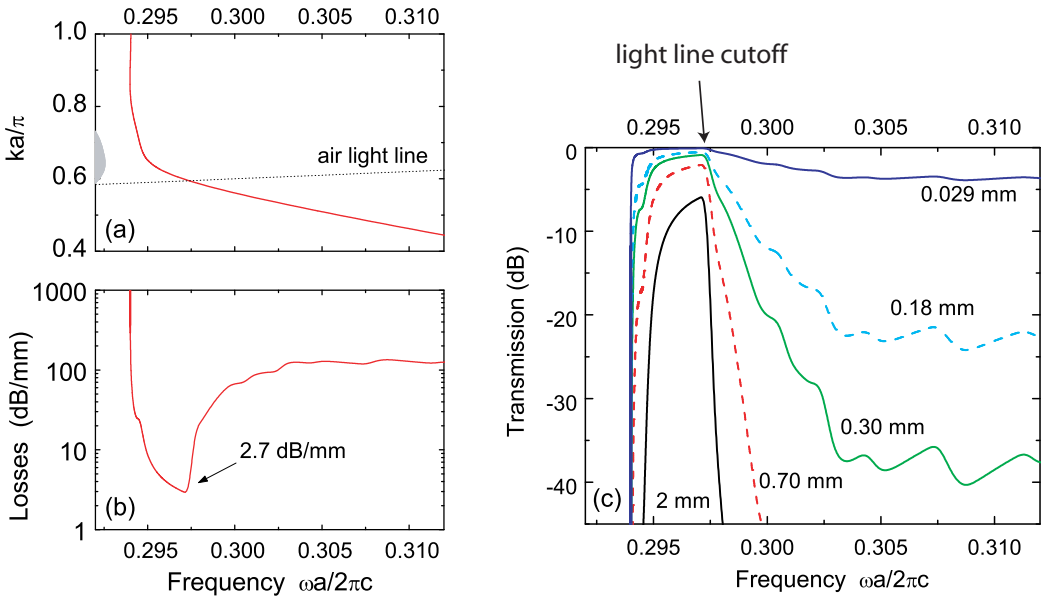

Figure 3.15: (a) Dispersion of the defect mode, (b) propagation loss, (c) transmission spectra with the parameters of the experiment of Ref. [85]. Parameters used in the calculations are as in the caption of Fig. 3.14: $r/a = 0.37$, $d/a = 0.5$, $\Delta r/a = 0.011$, $a = 445$ nm, $\epsilon = 12$. Transmission spectra in (c) should be directly compared to Fig. 3.14b.

tal structure and the quoted disorder parameter are shown. The defect mode is guided for frequencies below $\omega a/(2\pi c) = 0.297$ (Fig. 3.15a). The propagation loss in Fig. 3.15b has a minimum of 2.7 dB/mm when the defect mode crosses the light line: this result is in amazingly good agreement with the experimental value of 2.4 dB/mm. The losses increase rapidly both below the light line, due to the decreased group velocity of the defect mode, and above the light line because of the onset of intrinsic losses. Propagation loss shown in Fig. 3.15b has been obtained by the calculated dimensionless loss $\alpha \cdot a$ by dividing for the corresponding lattice constant, which is $a = 445$ nm in this case. Thus, propagation loss in dB/mm units are obtained and directly compared to the value extracted from experimental data. Finally, in order to recover the transmission spectra for different sample lengths, the curve plotted in Fig. 3.15b is multiplied by the length of the sample. This gives the transmission (in dB) for different lengths of the photonic crystal waveguides, as shown in Fig. 3.15c and directly compared to experimental spectra. The comparison with the measured data reported in Fig. 3.14b is very satisfactory and almost surprising. Besides a small discrepancy coming

from experimental inaccuracy of the reference frame to which the spectra are normalized, our theoretical model seems able to reproduce all the qualitative and quantitative features of experimental data. It is worth reminding that all theoretical results shown in Fig. 3.15 have been obtained without adjustable parameters, and thus it can be concluded that the present model gives an adequate account of disorder-induced losses in W1 waveguides, when state-of-art values for the roughness are assumed. In particular, it appears to be confirmed that the main source of scattering loss for truly guided modes relies on disorder effects induced by the random distribution of variable hole radii. This indicates also that further improvements in fabrication should concentrate in this aspect in order to reduce propagation losses in these systems and make them really appealing for future all-optical circuits applications.

In our theoretical model, no disorder-induced scattering into the counter-propagating defect mode has been considered, like, e.g., in Ref. [95]. The fair agreement between calculated and measured values for the losses below the light line that has been shown here seems to prove that out-of-plane scattering into the leaky waveguide modes is, indeed, the dominant loss mechanism for the high contrast photonic crystal slabs considered in this work. As a final remark, it should be pointed out that in a more advanced model the variation of the hole radius could take place within the same hole, i.e. microroughness of the side-walls could be included in the present theoretical approach.

Chapter 4

Quantum theory of radiation-matter interaction

Up to this point, the physics of photonic crystal slabs has been considered mostly for what concerns the "optical" point of view, that is studying the dispersion and propagation properties of light in periodic dielectric media. This is also what is commonly found in the existing literature, where the original proposal to exploit photonic band gap materials in order to modify the radiation-matter interaction properties has been only partly studied in the last years, while research efforts mostly concentrated on understanding their optical properties in view of applications to integrated optics.

In this Chapter we analyze the radiation-matter interaction in photonic crystal slabs, by considering the effects of the interplay between the electromagnetic field and semiconductor material excitations that give rise to the manifestation of so-called *polaritonic* effects. Generally speaking, *polaritons* are the mixed states resulting from the interaction between the retarded part of the electromagnetic field and dipole-active quasi-particles in solids (phonons, excitons, etc.). An overview of the main physical concepts within the exciton and polariton pictures in Semiconductor physics will be given as an introduction for the non-specialized reader. The purpose of the present study is twofold. On one side we would like to introduce the concept of strong radiation-matter coupling and that of *polariton* state in the context of photonic crystal research. This is also a way for going back to the original interest that motivated the growth of this fruitful research field, i.e. understanding the consequences of photonic band gap properties on the radiation-matter interaction. On the other hand, we want to emphasize, in the framework of polariton research, the great possibilities offered by photonic crystals for the tailoring of strong coupling regime between electromagnetic field and semiconductor exciton states. The first study of radiation-matter interaction of

periodic arrangements of quantum wells traces back to the theoretical work of Ref. [96]. Up to now, very few papers appeared regarding this interesting topic, the most important ones concerning the experimental [13] and theoretical [97, 98] investigation of strong coupling regime in organic-based systems. Exciton polaritons in one-dimensional photonic crystals (ideal Bragg mirrors) in which one of the constituent media has a strong excitonic character were studied in Refs. [99, 100] by using a classical approach. Other works concentrated on studying some physical properties of so called phonon-polaritonic photonic crystals, in which one of the materials constituting the photonic band gap structure has an intrinsic phononic character [101, 102]. The influence of quantum well excitons on the longitudinal part of the electromagnetic field, which produces a shift of photonic modes, has been studied in Ref. [103] for deeply patterned photonic crystals with an unpatterned quantum well below the photonic crystal region. Effects of polarizable media infiltrated in opal-based three dimensional photonic crystals have been also studied both experimentally [104, 105] and theoretically [106]. Systems like the ones studied in the present work have not been addressed, up to now, in the existing literature, neither theoretically nor experimentally.

In the present study, we consider as our model system a photonic crystal membrane made of a semiconductor material (usually GaAs) with a quantum well (QW) of a compatible crystalline structure (usually InGaAs) grown in its core layer and patterned with the same periodic lattice. The QW is chosen as the reference active material providing the electronic excitations with which the electromagnetic eigenmodes can interact. The problem of radiation-matter interaction in photonic crystal slabs is tackled by using a pure quantum mechanical formalism. A second-quantized theory has been developed and will be described in detail; our theoretical approach leads to a clear and rigorous description of the problem. The main results of the present analysis show that polaritonic effects could be present in photonic crystal slabs, provided that the exciton-photon coupling energy is larger than the intrinsic radiative linewidth of a quasi-guided photonic mode. The new quasi-particles arising from this strong coupling between photons and QW excitons in the photonic crystal slab are called *photonic crystal polaritons*. The comparison between our quantum formalism and a semiclassical treatment of the optical properties via the scattering matrix method (extended here to treat frequency dispersive dielectric materials, as the QW layer) shows a favorably good agreement. These interesting results pave the way for new exciting developments in the investigation of hybrid semiconductor structures exhibiting both photonic and electronic band gap characteristics, besides the same physical dimensionality underlying both photon and electron confinement. Some of these new lines of research will be pointed out at the end of

the present work.

4.1 Overview of exciton and polariton physics

Before starting the description of our quantum theory of photonic crystal polaritons, it is useful to recall the generalities of exciton and polariton concepts in Solid State Physics. These are well established physical topics, treated also in some textbooks at undergraduate level [8, 107, 108] and in some more advanced monographs [109, 110].

Excitons are the bound states of electron-hole pairs in a semiconductor or insulator crystal, and thus they present a discrete spectrum in emission or absorption of light. They can be described as elementary excitations, or quasi-particles, even if their physics goes beyond the one-electron picture in electronic band theory. It is very interesting that absorption lines due to excitonic transitions in bulk semiconductors present a hydrogen-like spectrum with very narrow linewidths. In the weak excitation regime, these quasi-particles obey a Bose-Einstein statistics and can be effectively considered as bosons. From a theoretical point of view, in semiconductor crystals the Coulomb interaction between an electron in the conduction band and a hole in the valence band is screened by the high-value dielectric constant of the material, and are usually called *shallow* or weakly bound. As such, they are very well described by an effective mass approximation. In the single-particle picture, we write the crystal ground state as a Slater determinant in which all Bloch states within the valence band are filled

$$\Psi_0 = \mathcal{A}\{\psi_{\mathrm{v}\mathbf{k}_1}(\mathbf{r}_1), \psi_{\mathrm{v}\mathbf{k}_2}(\mathbf{r}_2), ..., \psi_{\mathrm{v}\mathbf{k}_N}(\mathbf{r}_N)\} \tag{4.1}$$

where the symbol $\mathcal{A}$ indicates the antisymmetric product of states, and N is the total number of electrons in the crystal. When an electron is excited to a conduction band Bloch state, the crystal state in the one-electron scheme is given by

$$\Psi_{\mathrm{c}\mathbf{k}_\mathrm{c},\mathrm{v}\mathbf{k}_\mathrm{v}} = \mathcal{A}\{\psi_{\mathrm{v}\mathbf{k}_1}(\mathbf{r}_1), \psi_{\mathrm{v}\mathbf{k}_2}(\mathbf{r}_2), ...\psi_{\mathrm{c}\mathbf{k}_\mathrm{c}}(\mathbf{r}_i)..., \psi_{\mathrm{v}\mathbf{k}_N}(\mathbf{r}_N)\} \tag{4.2}$$

where the valence function $\psi_{\mathrm{v}\mathbf{k}_\mathrm{v}}$ has been replaced by the conduction function $\psi_{\mathrm{c}\mathbf{k}_\mathrm{c}}$ for the i-th electron. The explicit, single-particle Bloch states are generally given by

$$\psi_{n\mathbf{k}}(\mathbf{r}) = e^{i\mathbf{k}\cdot\mathbf{r}} u_{n\mathbf{k}}(\mathbf{r}), \qquad u_{n\mathbf{k}}(\mathbf{r}) = u_{n\mathbf{k}}(\mathbf{r}+\mathbf{R}) \tag{4.3}$$

satisfying the Bloch theorem [8], $\forall\ \mathbf{R}$ of the direct crystal lattice. We expand the general exciton wavefunction on the states of the form 4.2 as

$$\Psi_{\mathrm{exc}} = \sum_{\mathbf{k}_\mathrm{c},\mathbf{k}_\mathrm{v}} A(\mathbf{k}_\mathrm{c}, \mathbf{k}_\mathrm{v})\, \Psi_{\mathrm{c}\mathbf{k}_\mathrm{c},\mathrm{v}\mathbf{k}_\mathrm{v}}, \tag{4.4}$$

where $A(\mathbf{k}_\mathrm{c}, \mathbf{k}_\mathrm{v})$ is an envelope function in reciprocal space. We can define an exciton wave vector $\mathbf{K}_\mathrm{ex} = \mathbf{k}_\mathrm{c} - \mathbf{k}_\mathrm{v}$. For shallow excitons, like the ones usually present in semiconductors, the Schrödinger equation obtained by calculating the matrix elements of the all-electron Hamiltonian between states of the form 4.2 can be written as [109]

$$\left[E_\mathrm{c}(-i\nabla_\mathrm{e}) - E_\mathrm{v}(-i\nabla_\mathrm{h}) - \frac{e^2}{\epsilon_\mathrm{diel}|\mathbf{r}_\mathrm{e} - \mathbf{r}_\mathrm{h}|} + J_\mathrm{cv}\,\delta(\mathbf{r}_\mathrm{e} - \mathbf{r}_\mathrm{h}) - E\right] F(\mathbf{r}_\mathrm{e}, \mathbf{r}_\mathrm{h}) = 0, \tag{4.5}$$

where the exciton envelope function normalized to the crystal volume in real space is

$$F(\mathbf{r}_\mathrm{e}, \mathbf{r}_\mathrm{h}) = \frac{1}{\sqrt{V}} \sum_{\mathbf{k}_\mathrm{c}, \mathbf{k}_\mathrm{v}} A(\mathbf{k}_\mathrm{c}, \mathbf{k}_\mathrm{v}) e^{i(\mathbf{k}_\mathrm{c}\cdot\mathbf{r}_\mathrm{e} - \mathbf{k}_\mathrm{v}\cdot\mathbf{r}_\mathrm{h})}. \tag{4.6}$$

The energies $E_\mathrm{c}(\mathbf{k})$ and $E_\mathrm{v}(\mathbf{k})$ are the conduction and valence band dispersions, schematically represented in Fig. 4.1a. The background dielectric constant of the semiconductor material, ϵ_diel, screens the attractive Coulomb interaction between electron and hole, and J_cv is the electron-hole exchange interaction. The solution of Eq. 4.5 yields the following energy spectrum

$$E_n(\mathbf{K}_\mathrm{ex}) = E_g - \frac{R^*}{n^2} + \frac{\hbar^2|\mathbf{K}_\mathrm{ex}|^2}{2M}, \qquad n = 1, 2, 3, ... \tag{4.7}$$

where the effective Rydberg (in analogy with atomic transitions in alkali atoms) is defined as $R^* = \hbar^2/(2\mu a_B^2)$. In the last expressions, $\mu^{-1} = (m_\mathrm{e}^*)^{-1} + (m_\mathrm{h}^*)^{-1}$ is the inverse of the reduced effective mass and $M = m_\mathrm{e}^* + m_\mathrm{h}^*$ is the total effective mass of the two-particle system; the exciton Bohr radius is defined as $a_B = \hbar^2\epsilon_\mathrm{diel}/(\mu e^2)$, which is about two orders of magnitude larger than the atomic Bohr radius ($\sim$ 0.053 nm) owing to the large dielectric constant and small effective mass. The exciton quasi-particle and its energy spectrum are schematically illustrated in Figs. 4.1b and c.

In order to treat optical properties connected with excitonic transitions in semiconductors, it is useful to introduce the concept of *oscillator strength*. This quantity is defined as

$$f_{\hat{\mathbf{e}}} = \frac{2}{m\hbar\omega} \left| \langle \Psi_\mathrm{exc} | \hat{\mathbf{e}} \cdot \sum_{i=1}^{N} \mathbf{p}_i | \Psi_0 \rangle \right|^2 \tag{4.8}$$

where $\hbar\omega = E_\mathrm{exc} - E_0$ is the transition energy, m is the free electron mass, $\mathbf{p}_i$ are the electrons momentum operators, and $\hat{\mathbf{e}}$ is the polarization vector of the electromagnetic field, the sum is over all the electrons of the system, and the 2 factor comes from the spin degree of freedom. It can be shown [110] that in the case of 3D excitons in bulk semiconductors the oscillator strength is proportional to the crystal volume and is calculated analytically as

$$f_{\hat{\mathbf{e}}} = g\frac{2}{m\hbar\omega} |\hat{\mathbf{e}} \cdot \mathbf{p}_\mathrm{cv}|^2\, 2V |F(\mathbf{r} = 0)|^2 \delta_{\mathbf{K}_\mathrm{ex}, 0}, \tag{4.9}$$

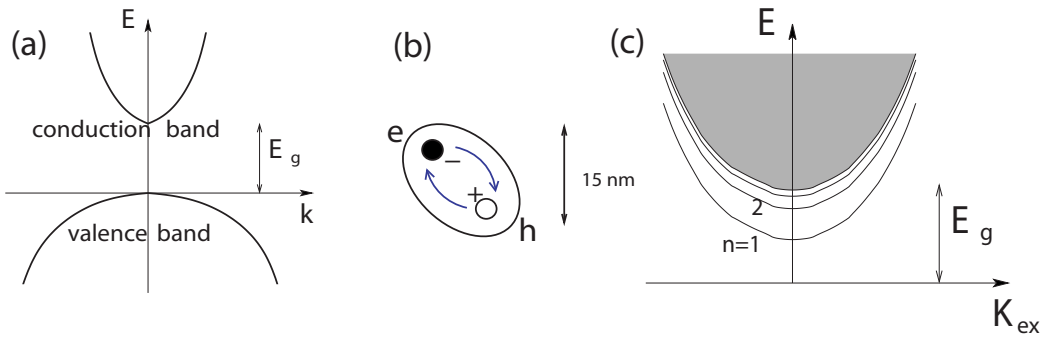

Figure 4.1: Schematic illustration of the exciton concept: (a) Electronic band structure in a single-particle picture. Taking into account the Coulomb interaction of an electron in the conduction band and a hole in the valence band, which give rise to (b) electron-hole pairs with discrete hydrogen-like energy spectrum, the two-particle band structure represented in (c) can be obtained.

where the factor g is the the spin-orbit factor of the exciton transition (which takes into account the structure of the valence band), and the single-electron interband momentum matrix element is defined as $\mathbf{p}_{\mathrm{cv}} = \langle u_{\mathrm{c0}}|\mathbf{p}|u_{\mathrm{v0}}\rangle$. In order to obtain Eq. 4.9, the momentum matrix element of Eq. 4.8 must be evaluated in the effective mass approximation, expressing the exciton envelope function in terms of relative and center-of-mass coordinates, $F = F(\mathbf{r}, \mathbf{r}_{\mathrm{cm}})$, which are defined as usual by the expressions

$$\mathbf{r} = \mathbf{r}_{\mathrm{e}} - \mathbf{r}_{\mathrm{h}}\,, \qquad \mathbf{r}_{\mathrm{cm}} = \frac{m_{\mathrm{e}}^{*}\mathbf{r}_{\mathrm{e}} + m_{\mathrm{h}}^{*}\mathbf{r}_{\mathrm{h}}}{M}\,. \tag{4.10}$$

For free excitons we can safely assume that

$$F(\mathbf{r}, \mathbf{r}_{\mathrm{cm}}) = e^{i\mathbf{K}_{\mathrm{ex}}\cdot\mathbf{r}_{\mathrm{cm}}}\, F(\mathbf{r}), \tag{4.11}$$

which explains the function $F(\mathbf{r} = 0)$ in Eq. 4.9.
When polaritonic effects can be neglected, the oscillator strength of the exciton transition is related to the absorption lineshape by

$$\int_{\mathrm{line}} \alpha(\omega)\mathrm{d}\omega = \frac{2\pi^2 e^2}{n_{\mathrm{diel}} mc}\,\frac{f}{V}, \tag{4.12}$$

where the absortpion coefficient $\alpha(\omega)$ is integrated over the exciton transition peak in the absorption spectrum. This allows the experimental determination of the oscillator strength.

Polaritons are the mixed states that form when the radiation-matter interaction is stronger than the intrinsic decoherence mechanisms of both excitons and photons in a semiconductor material. Generally speaking, optical absorption of exciton states is conceptually different from that of electron-hole pairs. The exciton absorption process implies the absorption of a single photon with defined wave vector (see Eqs. 4.9 and 4.12), where the energy and momentum conservation laws require that the interaction takes place when the two dispersion relations (that of excitons and that of photons in the material) intersect. The exciton-photon interaction implies that the final state is a linear combination of exciton and photon eigenfunctions. These states are called exciton-polaritons. Schematically, in the polariton picture the absorption process of light in a bulk semiconductor material is not due to the direct absorption of photons, but it is the result of polariton scattering with other dissipative excitations, such as lattice vibrations. Ideally, at $T \to 0$ and in a very pure crystal, a photon enters the material, produces an exciton, and viceversa until the photon escapes the material out of the following interface. It has been proven experimentally that Eq. 4.12 is valid at high temperature, when the lattice vibrations dominate and polaritonic effects are negligible, while at very low temperature the polariton picture dominates and the physics of polariton coherence within the crystal has to be taken into account. For a thorough discussion on the concepts of temporal and spatial coherence of polaritons in bulk semiconductors we refer to Refs. [109, 110]. The schematic transfer of energy and momentum between exciton and photon is schematically shown in Fig. 4.2a. The mechanical analog of this physical process is constituted by the problem of two coupled harmonic oscillators, as displayed in Fig. 4.2b.

A classical theory of polaritons was developed in the early fifties by Huang [111] in the context of the interaction of the electromagnetic radiation with long-wavelength lattice vibrations in ionic crystals. An analogous treatment can be done for exciton-polaritons. In the semi-classical approach, a frequency dispersive dielectric constant is assumed, in which the exciton resonance ω_0 is a pole for $\epsilon(\omega)$. The solution of Maxwell's equations with the constitutive relation $\mathbf{D} = \epsilon(\omega)\mathbf{E}$ yields two distinct equations, one for the transverse modes, $\epsilon(\omega) = c^2k^2/\omega^2$, and the other for longitudinal modes, $\epsilon(\omega) = 0$. The solutions of these equations give the dispersion relation schematically shown in Fig. 4.2c. The transverse modes display upper and lower polariton branches, which anticross in correspondence of the frequency/momentum resonance with the photon dispersion in the material, $\omega = ck/n$. Two important parameters characterize the polariton dispersion as obtained from the classical theory of Maxwell's equations: (a) the *longitudinal-transverse* (LT) splitting $\omega_{\mathrm{LT}} = \omega_{\mathrm{L}} - \omega_{\mathrm{T}}$, and the *polariton* splitting $2\omega_c = (2\omega_0\omega_{\mathrm{LT}})^{1/2}$,

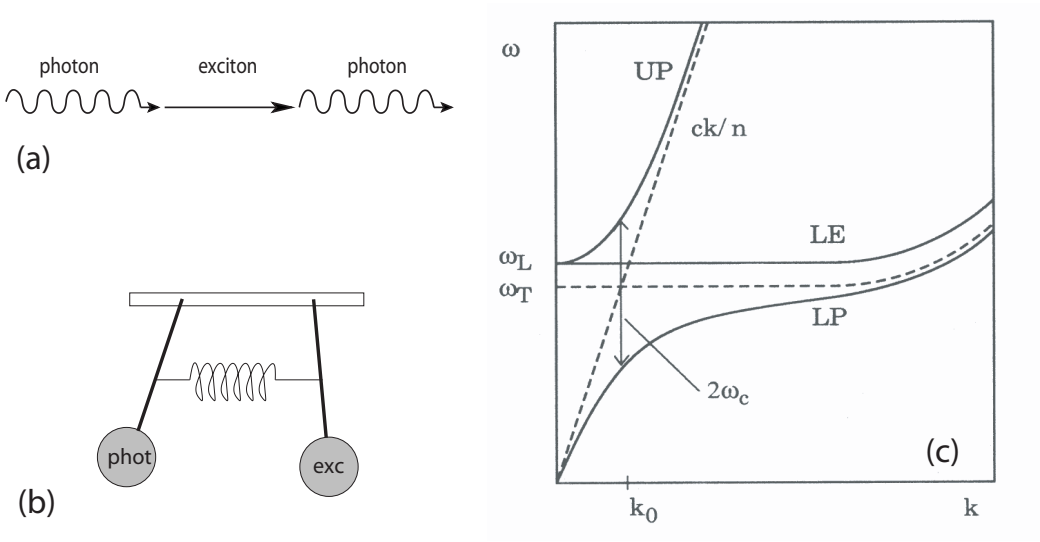

Figure 4.2: (a) Schematic illustration of stationary polariton states in a bulk semiconductor, in which photon and exciton mutually exchange energy and momentum, and (b) mechanical analog given by two coupled harmonic oscillators; in (c) the typical dispersion curves of upper and lower polariton branches and the uncoupled longitudinal exciton (full lines) is shown together with the bare exciton and photon dispersions (dashed lines).

which basically is a measure of the interaction between material excitations and the retarded electromagnetic field. It can be seen that the polariton dispersion turns upwards at large wave vectors, due to the spatial dispersion of exciton center of mass (see Eq. 4.7). The meaning of Fig. 4.2c is that it is the dispersion of polaritons, and not that of excitons, which is measured in good semiconductor crystals at low temperature, as described, e.g., in [107].

Even if the polariton dispersion can be obtained by a semi-classical treatment of the electromagnetic problem, it is only through a pure quantum approach that the physical nature of the polaritonic quasi-particles can be understood. A quantum theory of exciton-polaritons in bulk semiconductors was developed in the late fifties by Hopfield [112, 113] and Agranovich [114]. This theoretical approach basically relies on describing exciton and photon fields within a second-quantization formalism, in which creation and annihilation operators of field quanta are defined and the proper commutation relations are satisfied. Neglecting non-quadratic terms in the bosonic operators yields a second-quantized Hamiltonian corresponding to a generalized coupled oscillators model (see Fig. 4.2b). The results are stationary states whose dispersion relation coincides with the one found from the semi-classical

treatment (see Fig. 4.2c) [112], in which the LT splitting

$$\omega_{\rm LT} = \frac{2\pi\, e^2}{4\pi\epsilon_0\epsilon_{\rm diel}\, m\omega_0}\frac{f}{V}\,, \tag{4.13}$$

and the exciton-photon coupling

$$\omega_c = \left(\frac{\omega_0\omega_{\rm LT}}{2}\right)^{1/2} = \left(\frac{\pi e^2}{4\pi\epsilon_0\epsilon_{\rm diel} m}\frac{f}{V}\right)^{1/2}, \tag{4.14}$$

are now expressed in terms of the microscopic quantities, such as the oscillator strength per unit volume [109]. A proper generalization of this procedure has been followed to develop the quantum mechanical theory of photonic crystal polaritons described in the next Section. It is worth pointing out that Eqs. 4.13 and 4.14 are given in M.K.S. units. In order to write the corresponding expressions in Gaussian units, the substitution $e^2(4\pi\epsilon_0)^{-1} \rightarrow e^2$ should be made.

Excitons in quantum wells and microcavity polaritons

A *quantum well* is a thin layer of a semiconductor material sandwiched between thicker layers of a different semiconductor material with wider electronic band gap. The band discontinuity created at the hetero-interfaces of the different materials between conduction and valence band edges is commonly known as *band offset*. This variation of band edges from one material to the other acts as an effective confining potential for electrons and holes. We assume in the following that electrons and holes are confined in the same layer[1]. The envelope function approximation allows for an accurate treatment of electronic states in heterostructures such as quantum wells, superlattices and lower dimensionality systems as quantum wires and dots [115]. A QW is the physical realization in a solid-state system of the typical quantum mechanical particle-in-a-box problem. If the z coordinate corresponds to the growth direction, the motion of the particles is quantized along z but it is free in the plane (x, y). Thus, exciton energy spectrum is characterized by two-dimensional *subbands* $E_n(\mathbf{k}_\parallel)$ as a function of the in-plane exciton wave vector[2]. Excitons envelope eigenfunctions in a QW can be generally written as

$$F(\mathbf{r}_{\rm e}, \mathbf{r}_{\rm h}) = e^{i\mathbf{K}_{\rm ex}\cdot\mathbf{r}_{\rm cm\parallel}}\, F(\mathbf{r}_\parallel, z_{\rm e}, z_{\rm h}), \tag{4.15}$$

where $\mathbf{K}_{\rm ex}$ indicates now the in-plane exciton center-of-mass wave vector, while $\mathbf{r}_\parallel$ is the in-plane relative coordinate. The function $F(\mathbf{r}_\parallel, z_{\rm e}, z_{\rm h})$ depends

[1] This kind of hetero-structures is usually called of the type-I.

[2] It should be noted the analogy of exciton confinement in QWs with the photonic confinement in planar dielectric waveguides, which can be viewed as the optical analog of the particle-in-a-box problem.

on the solution of the Schrödinger equation for the z degree of freedom, with appropriate confining potentials for electrons and holes. Different regimes can be obtained, depending on the strength of the confining potential and on the QW width [109].

The characterizing quantity for absorption processes of QW excitons is the oscillator strength per unit area, which from Eqs. 4.8 and 4.15 becomes

$$\frac{f_{\hat{\mathbf{e}}}}{S} = g\frac{2}{m\hbar\omega}|\hat{\mathbf{e}}\cdot\mathbf{p}_{\mathrm{cv}}|^2\left|\int F(\mathbf{r}_{\parallel}=0,z,z)\mathrm{d}z\right|^2, \tag{4.16}$$

and which can be measured from the absorption probability (dimensionless quantity) integrated over the excitonic absorption peak through a relation similar to Eq. 4.12.

The great progress in nanofabrication technology and growth techniques over the last 25 years has brought a new boost on the study of the optical properties of quantum confined systems. In particular, one of the most interesting aspects for the control of photonic states is to study phenomena connected with the interaction between confined photonic modes and material excitations. In this sense, planar microcavities with embedded various active media like QWs or dots offered an important benchmark for studying polaritonic effects in low dimensional systems. In a planar microcavity (also known as Fabry-Pérot resonator), the electromagnetic field is confined in a central cavity layer of width L_{cav} surrounded by two Bragg mirrors on both sides of the cavity. The strong coupling regime of radiation-matter coupling in planar microcavities with embedded QWs has been observed in the beginning of nineties [116, 117], manifesting itself with a splitting of coupled exciton-photon modes when the resonance condition is satisfied. The energy separation at resonance is called *vacuum-field Rabi* splitting, which is the 2D analog of the polariton anticrossing in the dispersion of 3D mixed exciton-photon states (Fig. 4.2c). These 2D mixed exciton-photon modes are called *cavity polaritons*, and have been a very fruitful research field in the last ten years. For reviews on the last developments see Ref. [118]. From a theoretical point of view, the dynamics of coupled exciton-photon states in microcavities has been studied with a pure quantum mechanical formalism [119] and with a semiclassical treatment of light-matter coupling made with a transfer matrix formalism [120]. The crossover between weak and strong coupling regimes can be studied also by taking into account the damping of the Fabry-Pérot mode and of the excitonic transition by defining imaginary parts, γ_{ph} and γ_{ex}, of the respective mode energies, E_{ph} and E_{ex}, in the framework of a simple two-oscillator model

$$\hat{H} = \begin{bmatrix} E_{\mathrm{ex}} - i\gamma_{\mathrm{ex}} & V \\ V & E_{\mathrm{ph}} - i\gamma_{\mathrm{ph}} \end{bmatrix}, \tag{4.17}$$

where the exciton-photon coupling energy is given by

$$V = \left(\frac{2\pi\hbar^2 e^2}{4\pi\epsilon_0 \epsilon_{\rm cav}\, m L_{\rm eff}} \frac{f}{S} \right)^{1/2} . \tag{4.18}$$

The effective cavity length $L_{\rm eff} = L_{\rm cav} + L_{\rm DBR}$ takes into account the penetration of the photonic confined mode into the Bragg mirrors. Within this simple model, the crossover from the weak to the strong coupling regime occurs for $V > |\gamma_{\rm ex} - \gamma_{\rm ph}|/4$; the vacuum field Rabi splitting at resonance is $2\hbar\omega_c = 2V$. The polariton splitting is reduced in microcavities with respect to the bulk, even when the microcavities contain several QWs[3], as it can be estimated by comparing Eqs. 4.14 and 4.18 with parameters taken from the literature [110]. Very recently, cavity polaritons have been receiving much attention thanks to the discovery of amplified stimulated polariton scattering [121], which paves the way for the possible polariton-based laser, or *p-laser*.

4.2 Second quantization in photonic crystal slabs

We want to extend the study of radiation-matter interaction in quantum confined electron and photon systems to QWs embedded in a photonic crystal slab. The systems attracting our attention in the present work are schematically drawn in Figs. 4.3a and b for the one- and two-dimensional periodic lattices, respectively. They are basically composed by photonic crystal slabs of a high refractive index material, in which one or more QWs of a compatible material are grown within the core layer. The dielectric material constituting the photonic crystal slab acts also as barrier material for the carriers (electrons and holes) confined in the thin QW layer. Typical thickness values of the QW layer are of the order of 10 nm, while the dielectric core layer is between 100 and 200 nm thick. We thus assume that the confining dielectric constant for bare photonic eigenmodes in the unpatterned planar waveguide is constituted by $\epsilon = \epsilon_{\rm diel}$, i.e. the dielectric constant of the core layer, neglecting the dielectric constant of the QW layer that is much thinner. The QW is periodically patterned with the same lattice as the photonic crystal structure. Thus, exciton center-of-mass eigenfunctions are not free as in usual QWs, but are subject to a further confining potential provided by the etched air regions. As a general remark, it is clear that exciton and photon wavefunctions are vertically confined and they are subject to effective potentials

[3]Typical values are 16 meV for bulk polaritons in GaAs, against a few meV in GaAs-based microcavities.

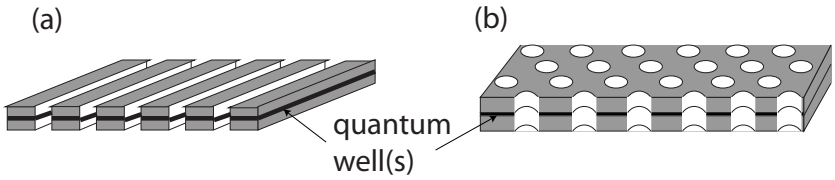

Figure 4.3: Schematic view of the systems considered in this Section: (a) one- and (b) two-dimensional (triangular lattice of air holes) photonic crystal membranes of dielectric constant $\epsilon = \epsilon_{\rm diel}$ with a QW grown in the middle of the core layer and patterned with the same lattice as the photonic structure.

in the plane having the same spatial periodicity. Roughly speaking, we could say that confined excitons and photons display the same dimensionality in this problem.

In the present Section we describe the quantum theory of the coupling between QW excitons and radiation modes in photonic crystal slabs starting from the second quantization of bare exciton and photon fields. It is worth noting that a similar formalism has been used in the literature to study, e.g., QW exciton-polaritons in planar microcavities [119], in which both photons and excitons are one-dimensionally confined, and in cylindrical semiconductor cavities, which display 3D confined photons versus the 1D exciton confinement [122]. From a theoretical point of view, the main difficulty of the present approach with respect to previously published works is that the second-quantized theory has to take into account the non-trivial spatial dependence of $\epsilon(\mathbf{r})$ for the quantization procedure of the electromagnetic field. The purpose is to construct a second-quantized total Hamiltonian for the exciton-photon coupled states, and then diagonalize it exactly to obtain eigenenergies of the mixed modes. Starting from the general formalism, in order to describe bare exciton and photon fields we have to solve the classical wave equations and then reformulate the solutions in terms of normal degrees of freedom, or normal vibrating modes, by introducing creation and annihilation operators for the field quanta, and verifying that the commutation relations are satisfied. The total Hamiltonian of an interacting radiation and matter system is generally of the form

$$\hat{H}_{\rm tot} = \hat{H}_{\rm ph} + \hat{H}_{\rm mat} + \hat{H}_{\rm I} \tag{4.19}$$

where $\hat{H}_{\rm ph}$, $\hat{H}_{\rm mat}$ and $\hat{H}_{\rm I}$ are the radiation, matter and interaction Hamiltonians, respectively. We separately consider these contributions to the total energy of the system.

The classical electromagnetic problem in photonic crystal slabs is solved by employing the GME method. Thus, the quantum numbers for photonic

eigenmodes (for each polarization and parity) are $\mathbf{k}$ and n, where $\mathbf{k}$ is taken in the first Brillouin zone, and n generically labels the band number or the order of the guided mode in the effective planar waveguide. For convenience of notation we can group these indices by defining $\mu = (\mathbf{k}, n)$. The following expressions are given in M.K.S. units, as in the previous Section, but they can be easily converted to Gaussian units by imposing $4\pi\epsilon_0$ as unity. The fields can generally be expressed as a linear combination of normal modes of the system after the solution of GME equations

$$\mathbf{E}(\mathbf{r},t) = \sum_{\mu} \left(\frac{2\pi\hbar\omega_\mu}{4\pi\epsilon_0 V}\right)^{1/2} \left[\hat{a}_\mu \mathbf{E}_\mu(\mathbf{r}) e^{-i\omega_\mu t} + \hat{a}_\mu^\dagger \mathbf{E}_\mu^*(\mathbf{r}) e^{i\omega_\mu t}\right] \tag{4.20}$$

$$\mathbf{H}(\mathbf{r},t) = \sum_{\mu} \left(\frac{2\pi\hbar\omega_\mu}{4\pi\epsilon_0 V}\right)^{1/2} \left[\hat{a}_\mu \mathbf{H}_\mu(\mathbf{r}) e^{-i\omega_\mu t} + \hat{a}_\mu^\dagger \mathbf{H}_\mu^*(\mathbf{r}) e^{i\omega_\mu t}\right] \tag{4.21}$$

where $\hat{a}_\mu^\dagger$ ($\hat{a}_\mu$) are creation (destruction) operators of field quanta, and verify the following commutation relations (in the Coulomb gauge)

$$\left[\hat{a}_\mu, \hat{a}_{\mu'}\right] = \left[\hat{a}_\mu^\dagger, \hat{a}_{\mu'}^\dagger\right] = 0 \qquad \left[\hat{a}_\mu, \hat{a}_{\mu'}^\dagger\right] = \delta_{\mu,\mu'} \,. \tag{4.22}$$

The fields are normalized as

$$\int_V \epsilon(\mathbf{r}) \mathbf{E}_\mu(\mathbf{r}) \mathbf{E}_{\mu'}^*(\mathbf{r}) \mathrm{d}\mathbf{r} = \delta_{\mu\mu'} \tag{4.23}$$

$$\int_V \mathbf{H}_\mu(\mathbf{r}) \mathbf{H}_{\mu'}^*(\mathbf{r}) \mathrm{d}\mathbf{r} = \delta_{\mu\mu'} \,, \tag{4.24}$$

and they satisfy Maxwell's equations with periodic dielectric constant, Eqs. 1.6 and 1.7. The electromagnetic Hamiltonian can be obtained by the classical expression of the electromagnetic energy

$$\mathcal{H}_{\text{e.m.}} = \frac{1}{2} \int_V \left[\epsilon_0 \mathbf{E}(\mathbf{r},t) \cdot \mathbf{D}(\mathbf{r},t) + \mu_0 |\mathbf{H}(\mathbf{r},t)|^2\right] \mathrm{d}\mathbf{r} \,, \tag{4.25}$$

which in Gaussian units reads

$$[\mathcal{H}_{\text{e.m.}}]_{gauss} = \frac{1}{8\pi} \int_V \left[\mathbf{E}(\mathbf{r},t) \cdot \mathbf{D}(\mathbf{r},t) + |\mathbf{H}(\mathbf{r},t)|^2\right] \mathrm{d}\mathbf{r} \,. \tag{4.26}$$

After the expansion of the electric and magnetic fields in terms of creation and annihilation operators, Eq. 4.25 can be rewritten in the very intuitive and compact form

$$\hat{H}_{\text{ph}} = \sum_{\mu} \hbar\omega_\mu \left(\hat{a}_\mu^\dagger \hat{a}_\mu + \frac{1}{2}\right) \,. \tag{4.27}$$

In the second-quantized form, the electromagnetic energy stored in the system is seen as a sum over photons occupying the normal modes.

The matter Hamiltonian for a QW has been partially solved in the previous Section. It has been shown that the Schrödinger equation describing the elementary excitations of a semiconductor crystal can be written in terms of an effective Hamiltonian for the exciton center-of-mass envelope function. We thus treat the exciton as an elementary bosonic quasi-particle[4], whose dynamics is described by a wave function given by Eq. 4.15, which leads to a second-quantized exciton Hamiltonian of the form

$$\hat{H}_{\rm ex} = \sum_{\sigma} \hbar\Omega_{\sigma} \left(\hat{b}_{\sigma}^{\dagger} \hat{b}_{\sigma} + \frac{1}{2} \right) \tag{4.28}$$

where the exciton creation and destruction operators satisfy bosonic commutation relations analogous to Eq. 4.22, and the index σ generically labels the normal modes. The exciton spectrum $\hbar\Omega_{\sigma}$ in the periodically patterned QW structure is obtained by solving the single-particle Schrödinger equation

$$\left[-\frac{\hbar^2}{2M_{\rm ex}} \nabla^2 + V(x,y) \right] F(x,y) = (\hbar\Omega_{\rm ex})\, F(x,y)\,, \tag{4.29}$$

where the effective potential $V_{xy} = \infty$ in air regions, while it is $V_{xy} = 0$ in the non-patterned surface of the QW. It is basically the quantum problem of a particle in a periodic potential with infinite height barriers. For simplicity, we have assumed to decouple vertical and planar dynamics, by considering only the fundamental exciton state for confinement along z and taking into account only the planar degree of freedom. It should be noted that the periodicity of V_{xy} allows to classify exciton center-of-mass eigenmodes by the same quantum numbers used for the photonic problem, namely $\mathbf{k} = \mathbf{K}_{\rm ex}$ in the first Brillouin zone and $\mathbf{G}$ belonging to the same periodic lattice. In general, we can label exciton modes by the indices $(\mathbf{k}, \nu)$, where ν is an integer labelling the exciton band number at fixed $\mathbf{k}$ in the irreducible Brillouin zone. Expanding both potential and envelope functions in Fourier series, Eq. 4.29 can be written in the form

$$\sum_{\mathbf{G}'} \left[\frac{\hbar^2}{2M_{\rm ex}} |\mathbf{k} + \mathbf{G}'|^2\, \delta_{\mathbf{G},\mathbf{G}'} + V(\mathbf{G} - \mathbf{G}') \right] F_{\sigma}(\mathbf{G}') = \hbar\Omega_{\sigma}\, F_{\sigma}(\mathbf{G})\,, \tag{4.30}$$

which can be easily solved by using, for the matrix $V(\mathbf{G} - \mathbf{G}')$, the same Fourier expression as the one used in the photonic problem for $\epsilon(\mathbf{G} - \mathbf{G}')$. The numerical diagonalization of Eq. 4.30 as a linear eigenvalue problem yields the exciton spectrum $\hbar\Omega_{\sigma}$.

In order to recover the exciton-photon coupling Hamiltonian, one has to start from the usual radiation-matter coupling described by the interaction

[4] In our model we neglect light-hole/heavy-hole mixing effects [109], thus considering only heavy-hole exciton levels in-plane polarized.

Hamiltonian [in Gaussian units the first and second term on the right hand side are multiplied by $1/c$ and $1/c^2$, respectively]

$$\mathcal{H}_{\rm I} = -\frac{e}{m}\sum_{j=1}^{N}\mathbf{A}(\mathbf{r}_j)\cdot\mathbf{p}_j + \frac{e^2}{2m}\sum_{j=1}^{N}|\mathbf{A}(\mathbf{r}_j)|^2\,. \tag{4.31}$$

Equation 4.31 can be expressed in a second-quantized form by following mutatis mutandis the general procedure outlined in Ref. [119], which after lengthy calculations leads to the expression

$$\hat{H}_{\rm I} = i\sum_{\mu\sigma}C_{\mu\sigma}(\hat{a}_{\mu}+\hat{a}^{\dagger}_{-\mu})(\hat{b}^{\dagger}_{\sigma}-\hat{b}_{-\sigma}) + \sum_{\sigma}\sum_{\mu,\mu'}D_{\mu\mu'\sigma}(\hat{a}_{-\mu}+\hat{a}^{\dagger}_{\mu})(\hat{a}_{\mu'}+\hat{a}^{\dagger}_{-\mu'}), \tag{4.32}$$

where $D_{\mu\mu'\sigma} = C^{*}_{\mu\sigma}C_{\mu'\sigma}/\hbar\Omega_{\sigma}$. The photon self-interaction term coming from the second term of Eq. 4.31 is generally small, anyway we include it in the diagonalization of the total Hamiltonian. The exciton-photon coupling matrix elements are generally described by the relation

$$C_{\mu\sigma} = \left(\frac{2\pi e^2\hbar\Omega_{\sigma}^2}{4\pi\epsilon_0\omega_{\mu}}\right)^{1/2}\langle\Psi^{(exc)}_{\sigma}|\sum_{j}\mathbf{E}_{\mu}(\mathbf{r}_j)\cdot\mathbf{r}_j|0\rangle\,, \tag{4.33}$$

in which $\Psi^{(exc)}_{\sigma}$ is the all-electron exciton wavefunction corresponding to the exciton envelope eigenfunction F_{σ}, $\mathbf{E}_{\mu}$ is the electric field profile for the photonic mode at frequency ω_{μ} in the PC slab (see Eq. 4.20), and the sum is over all the QW electrons. It should be noted that Eq. 4.32 represents the generalization to the present problem of the exciton-photon interaction quantum Hamiltonian first introduced by Hopfield [112].

Finally, the second-quantized total Hamiltonian of the system considered is given by

$$\begin{aligned}\hat{H}_{\rm tot} &= \sum_{\mathbf{k},n}\hbar\omega_{\mathbf{k}n}\hat{a}^{\dagger}_{\mathbf{k}n}\hat{a}_{\mathbf{k}n} + \sum_{\mathbf{k},\nu}\hbar\Omega_{\mathbf{k}\nu}\hat{b}^{\dagger}_{\mathbf{k}\nu}\hat{b}_{\mathbf{k}\nu} + i\sum_{\mathbf{k},n,\nu}C_{\mathbf{k}n\nu}(\hat{a}_{\mathbf{k}n}+\hat{a}^{\dagger}_{-\mathbf{k}n})(\hat{b}^{\dagger}_{\mathbf{k}\nu}-\hat{b}_{-\mathbf{k}\nu})\\ &+ \sum_{\mathbf{k},\nu}\sum_{n_1,n_2}\frac{C^{*}_{\mathbf{k}n_1\nu}C_{\mathbf{k}n_2\nu}}{\hbar\Omega_{\mathbf{k}\nu}}(\hat{a}_{-\mathbf{k}n_1}+\hat{a}^{\dagger}_{\mathbf{k}n_1})(\hat{a}_{\mathbf{k}n_2}+\hat{a}^{\dagger}_{-\mathbf{k}n_2})\,.\end{aligned} \tag{4.34}$$

In Eq. (4.34), the first term indicates the photonic band dispersion (real part of the complex eigenenergies), $\hat{a}_{\mathbf{k}n}$ ($\hat{a}^{\dagger}_{\mathbf{k}n}$) being the destruction (creation) operators of a photon with wave vector $\mathbf{k}$ and band number n (labelling either the guided mode order or the band index). The second term represents the dispersion of exciton center-of-mass eigenmodes, whose solutions are given by Eq. 4.29. The ground state energy has been omitted from the free fields

Hamiltonians. In order to explicitly obtain the exciton-photon coupling matrix elements, $C_{\mathbf{k}n\nu}$, we have to express $\Psi^{(exc)}_{\mathbf{k}\nu}$ in the effective mass approximation in Eq. 4.33, after which we get

$$C_{\mathbf{k}n\nu} = \left(\frac{2\pi e^2 \hbar \Omega^2_{\mathbf{k}\nu}}{4\pi\epsilon_0 \omega_{\mathbf{k}n}}\right)^{1/2} \mathbf{r}_{\mathrm{cv}} \cdot \int \mathbf{E}_{\mathbf{k}n}(\mathbf{r}) F_{\mathbf{k}\nu}(\mathbf{r}, \mathbf{r}_{\mathrm{cm}})\, \mathrm{d}\mathbf{r}\,, \tag{4.35}$$

where $\mathbf{r}_{\mathrm{cv}} = \langle u_{\mathrm{c}0}|\mathbf{r}|u_{\mathrm{v}0}\rangle$. The electric field can be expanded in terms of its Fourier components, $c_{\mathbf{k}n}(\mathbf{G})$, as well as the exciton envelope function, owing to the spatial periodicity in the plane of the waveguide. Thus, factorizing the vertical and planar dynamics, we obtain

$$C_{\mathbf{k}n\nu} = \left(\frac{2\pi e^2 \hbar \Omega^2_{\mathbf{k}\nu}}{4\pi\epsilon_0 \omega_{\mathbf{k}n}}\right)^{1/2} \left(\sum_{\mathbf{G}} c_{\mathbf{k}n}(\mathbf{G}) F_{\mathbf{k}\nu}(\mathbf{G})\right) \mathbf{r}_{\mathrm{cv}} \cdot \int \mathbf{E}(z) F(\mathbf{r}_{\parallel} = 0, z, z)\, \mathrm{d}z\,, \tag{4.36}$$

and by assuming a constant electric field across the QW width, through Eq. 4.16 we obtain

$$C_{\mathbf{k}n\nu} \simeq \hbar \left(\frac{\pi e^2}{4\pi\epsilon_0 m} \frac{f}{S}\right)^{1/2} \hat{\mathbf{e}} \cdot \mathbf{E}(z_{\mathrm{QW}}) \sum_{\mathbf{G}} c_{\mathbf{k}n}(\mathbf{G}) F_{\mathbf{k}\nu}(\mathbf{G})\,, \tag{4.37}$$

where z_{QW} is the QW position along the vertical direction (in our reference frame, $z_{\mathrm{QW}} = 0$ corresponds to a QW placed at the center of the photonic crystal slab core layer). Thus, the coupling energy results to be proportional to $(f/S)^{1/2}$, which is analogous to the result of Eq. 4.18.

The total Hamiltonian, Eq. 4.34, is diagonalized by using a generalized Hopfield transformation [113, 122]. New destruction (creation) operators $\hat{P}_{\mathbf{k}}$ ($\hat{P}^{\dagger}_{\mathbf{k}}$) are defined as a linear combination of $\hat{a}_{\mathbf{k}n}$ ($\hat{a}^{\dagger}_{\mathbf{k}n}$) and $\hat{b}_{\mathbf{k}\nu}$ ($\hat{b}^{\dagger}_{\mathbf{k}\nu}$)

$$\hat{P}_{\mathbf{k}} = \sum_n W_{\mathbf{k}n} a_{-\mathbf{k}n} + \sum_{\nu} X_{\mathbf{k}\nu} b_{-\mathbf{k}\nu} + \sum_n Y_{\mathbf{k}n} a^{\dagger}_{\mathbf{k}n} + \sum_{\nu} Z_{\mathbf{k}\nu} b^{\dagger}_{\mathbf{k}\nu}\,. \tag{4.38}$$

In order to find the eigenenergies of the coupled exciton-photon modes, the condition

$$[\hat{P}_{\mathbf{k}}, \hat{H}_{\mathrm{tot}}] = E_{\mathbf{k}} \hat{P}_{\mathbf{k}} \tag{4.39}$$

is imposed. By explicitly calculating this expression, i.e. substituting in Eq. 4.39 the second-quantized expressions of Eqs. 4.34 and 4.38, after lengthy calculations a non-hermitian eigenvalue problem is obtained. The diagonalization of the resulting matrix, which is called *Hopfield matrix*, yields the eigenenergies $E_{\mathbf{k}}$ of the coupled system. The sums in Eq. 4.38 have to be truncated in order to deal with finite matrices. If $n_{\max}$ photonic bands and $\nu_{\max}$ excitonic levels at fixed $\mathbf{k}$ are retained in the basis set, the Hopfield matrix has dimensions $2(n_{\max} + \nu_{\max}) \times 2(n_{\max} + \nu_{\max})$, by considering both

positive- and negative-defined exciton and photon energy eigenvalues. After diagonalizing the full matrix, only eigenvalues with positive real part are taken.
In order to include the radiation damping of excitonic and photonic oscillators, we assume complex energy values for the bare exciton ($\hbar\Omega_{\mathbf{k}\nu}$) and photon ($\hbar\omega_{\mathbf{k}n}$) dispersions. This model is conceptually similar to Eq. 4.17 for the two oscillators. The imaginary part of photonic modes is calculated by the perturbative theory described in Sec. 1.2, while the intrinsic radiative damping of the exciton resonance is assumed as an input parameter, characteristic of the QW considered. It is worth stressing that with respect to previous diagonalization approaches we diagonalize the Hopfield matrix directly. Within our formalism, the diagonalization of the complex Hopfield matrix directly yields the complex dispersion of mixed states of radiation and material excitations. In particular, the real part of the eigenenergies $E_{\mathbf{k}}$ should correspond to the photonic crystal polariton states, when the system is in the strong coupling regime. On the contrary, in the weak coupling regime the fundamental properties of bare exciton and photon dispersions should be recovered after the diagonalization. The imaginary part of $E_{\mathbf{k}}$, as a consequence, directly gives the radiative linewidth of the coupled modes.

4.3 Photonic crystal polaritons

In this Section, results of the radiation-matter interaction effects are shown for the systems schematically displayed in Fig. 4.3[5]. We start from one-dimensional periodic structures, i.e. one-dimensional photonic crystal membranes with a QW at the center of the core layer. The structure parameters chosen for these calculations are: $d/a = 0.2$, $f_{\text{air}} = 0.3$, lattice constant $a = 350$ nm. The material constituting the patterned core layer of the photonic crystal membrane is assumed to have a dielectric constant $\epsilon_{\text{diel}} = 12.15$, as appropriate, e.g., for GaAs at optical wavelengths. The photonic band dispersion, i.e. real part of energy, for this structure is calculated by using the GME method (see Sec. 1.2) with 37 plane waves and 4 guided modes in the basis set. Results in the energy range 1.1-1.7 eV are shown in Fig. 4.4a. In Fig. 1b we display the corresponding imaginary part as a function of the wave vector, which shows a maximum at about 1.4 eV. The imaginary part goes to zero at $k_x = 0$, that is at normal incidence, and when the mode crosses the air light line, for which the photonic mode becomes truly guided and stationary. The complex photonic dispersion of the systems displays features already discussed in Chapter 2.

[5]Similar results have been published in Refs. [51, 52].

We are now interested in the system with embedded QW. This problem is treated by two different approaches: diagonalization of the pure quantum mechanical Hamiltonian (Eq. 4.34) and semiclassical solution of Maxwell's equations by the scattering matrix method. Within our quantum treatment, we assume that the QW exciton transition has an intrinsic linewidth $\Gamma_{\rm ex} = 0.1$ meV, and that the QW has the typical[6] oscillator strength per unit surface of $f/S = 8.4 \times 10^{12}$ cm^{-2}. These, besides the exciton fundamental energy resonance, are the only input parameters of the theory before diagonalizing the generalized Hopfield matrix.

If the photonic imaginary part is larger than the exciton-photon coupling matrix element (which is of the order of a few meV in this case), a QW placed at the center of the PC slab does not produce any important change in the photonic band dispersion. Indeed, this result is shown in Figs. 4.4c and d, in which the real and imaginary parts of the complex exciton-photon coupled eigenmodes are shown, with the fundamental excitonic resonance placed at $\hbar\Omega_0 = 1.42$ eV. In this *weak coupling* regime the photon and the exciton are almost uncoupled, as it can be seen from the crossing of the two dispersion relations in Fig. 4.4c. The imaginary part of the exciton increases by an order of magnitude correspondingly to the crossing point, but this has a negligible effect on the photonic radiative linewidth, which is still an order of magnitude larger than the excitonic one (see Fig. 4.4d). This situation is similar to the weak coupling regime in bulk or in planar microcavities. In this case the exciton photon coupling can be treated by Fermi's Golden Rule, giving rise to a radiative decay of the exciton.

In Fig. 4.4e the classical calculation of variable-angle surface reflectance is shown. The scattering matrix method, already employed for comparison with the GME method in the present work (see, e.g., Sec. 2.3), has been extended in this case in order to treat frequency dispersive dielectric layers [97]. In particular, the complex dielectric function of the QW layer assumed in our semi-classical model is

$$\epsilon(\omega) = \epsilon_\infty \left(1 + \frac{\hbar\omega_{\rm LT}}{\hbar(\Omega_0 - \omega) - i\Gamma_{\rm ex}} \right) , \tag{4.40}$$

where ϵ_∞ is the background dielectric constant of the QW material, $\hbar\Omega_0$ and $\Gamma_{\rm ex}$ are the same as in the quantum calculation, and the classical LT energy splitting can be expressed as (see Eq. 4.13)

$$\hbar\omega_{\rm LT} = \frac{2\pi\hbar\, e^2}{4\pi\epsilon_0\epsilon_\infty\, m\Omega_0\, L_{\rm QW}} \frac{f}{S} . \tag{4.41}$$

[6]These values are appropriate, e.g., for InGaAs QWs between GaAs barriers, and can be found in literature.

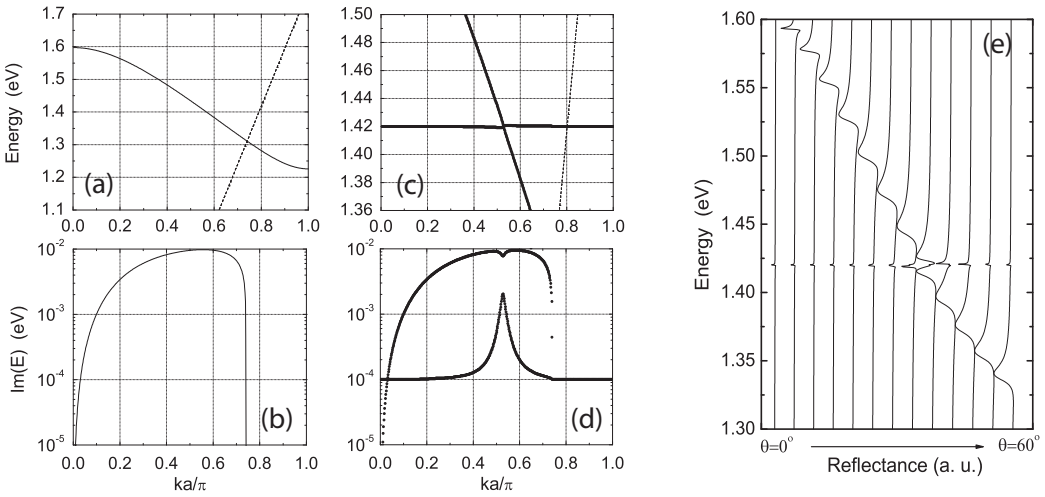

Figure 4.4: (a) Real and (b) imaginary parts of the complex photonic energies for the fundamental TE mode ($\sigma_{xy} = +1$,$\sigma_{kz} = -1$) as a function of the wave vector in the first Brillouin zone, for the 1D lattice without excitonic resonance (no QW); (c) real and (d) imaginary parts for the same structure with a QW at the center of the dielectric core, with an excitonic resonance at $\hbar\Omega_0 = 1.42$ eV. (e) Calculated variable-angle reflectance spectra by the scattering matrix method, for the same structure as in (c) and (d).

The last formula allows to put in one-to-one correspondence the two theoretical approaches. To an oscillator strength f/S assumed in the quantum treatment of radiation-matter coupling, a QW layer of width $L_{\rm QW}$ and a LT splitting $\omega_{\rm LT}$ obtained by Eq. 4.41 corresponds in the semi-classical theory. Thus, in order to make a direct comparison between our complementary theoretical methods, we assume $L_{\rm QW} = 8$ nm and $\hbar\omega_{\rm LT} \simeq 0.42$ meV in the scattering matrix calculation, which roughly correspond to the value of f/S given above. Moreover, the same exciton radiative damping of $\Gamma_{\rm ex} = 0.1$ meV has been used in the frequency dependent QW dielectric constant expression. Finally, the two theoretical approaches calculate the physical quantities for the same structure, without adjustable parameters. The results of Fig. 4.4e clearly confirm the ones of Fig. 4.4c, i.e. the system is in the weak coupling regime with the parameters assumed.

In order to observe the *strong coupling* regime, the energy of the excitonic resonance has to lie where the imaginary part of the photonic mode is smaller than the exciton-photon coupling matrix element. This consideration is similar to the argument given in the previous section for what concerns the weak/strong coupling crossover in planar microcavities with embedded QWs.

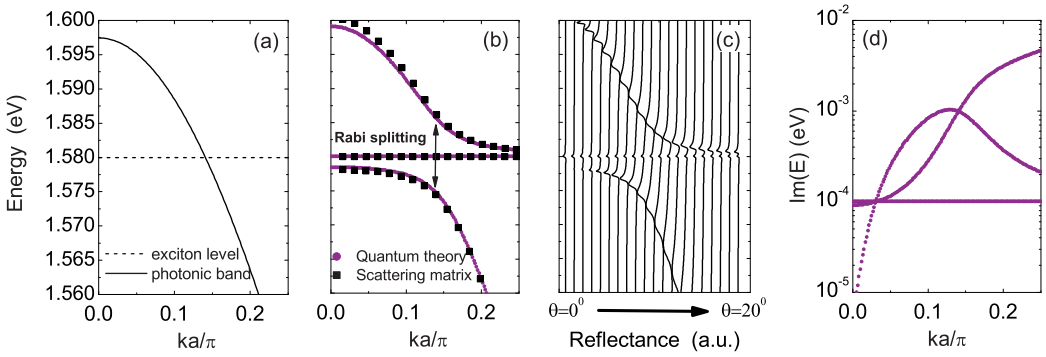

Figure 4.5: (a) Bare exciton and photon modes in the absence of interaction, for an exciton resonance $\hbar\Omega_0 = 1.58$ eV. (b) Real part of complex photonic crystal polaritons eigenenergies (points) calculated with the quantum theory, and dispersion of excited modes [squares, from (c)]; the vacuum field Rabi splitting is shown by an arrow. (c) Calculated variable-angle reflectance for the same structure as in (b), with semi-classical treatment of the QW layer. (d) Imaginary part of photonic crystal polaritons eigenenergies.

From Figs. 4.4a and b we see that for $\hbar\Omega_0 = 1.58$ eV the imaginary part of the photonic quasi-guided mode is about $\mathrm{Im}(\hbar\omega) = 10^{-3}$ eV. We thus assume to tune the exciton resonance to $\hbar\Omega_0 = 1.58$ eV, as shown in Fig. 4.5a. The results obtained by diagonalizing the full quantum Hamiltonian of the system are shown in Fig. 4.5b (points), where this time the photonic band dispersion is strongly modified by the effects of the non-perturbative exciton-photon coupling. Only two exciton center-of-mass quantized modes are taken in the basis set, which are largely sufficient in this case because the coupling with the photonic mode is mostly given by the lowest excitonic resonances. The results of our quantum theory are confirmed by comparison with scattering matrix calculations (squares) of the mode dispersion, extracted from the variable-angle reflectance spectra of Fig. 4.5c. As already pointed out in previous sections and in App. A, the sharp features appearing in the reflectance spectrum correspond to the excitation of quasi-guided modes above the light line, thus giving a point $(\mathbf{k}, \omega)$ of the corresponding band dispersion through the relation $k = (\omega/c)\sin\theta$. As it can be seen from Fig. 4.5b, the quantum theory is in excellent agreement with the classical approach, without adjustable parameters[7]. In particular, both theories confirm the anticrossing

[7]In this case, for a QW width $L_{\mathrm{QW}} = 8$ nm and a fundamental exciton energy $\hbar\Omega_0 = 1.58$ eV, a LT energy splitting $\hbar\omega_{\mathrm{LT}} \simeq 0.38$ meV has been used in the scattering matrix calculation.

behavior of exciton and photon modes, which is a clear effect of the strong coupling regime. The resonant features in reflectance spectra correspond to the excitation of new eigenstates of the system, which are mixed modes of photonic and excitonic eigenfunctions. We call these modes *photonic crystal polaritons*. With the parameters used in this work, the polariton splitting is as high as 10 meV at the anticrossing point, $k_x \simeq 0.14$, as shown in Fig. 2b. This splitting is found to be slightly larger than in semiconductor-based microcavities [116, 117, 118], see also previous Section. This is interpreted as follows. In a Fabry-Pérot cavity with embedded QWs, the exciton-photon coupling is well described by Eq. 4.18, in which the effective extension of the field L_{eff} is usually large due to the field penetration in the Bragg mirrors. In the systems we are considering, the coupling is mainly determined by the overlap integral of exciton center of mass envelope function and the spatial electric field profile (see Eq. 4.35). In particular, owing to the approximation made in Eq. 4.37, the value of the electric field at the QW position is determinant. In photonic crystal membranes the electromagnetic field of a quasi-guided mode is strongly confined within the core region, and thus the field-maximum at the core center increase by a factor of ~ 3 the strength of the coupling. We thus predict a larger vacuum-field Rabi splitting for photonic crystal polaritons, which is almost of the order of the bulk values typical of GaAs crystals (~ 16 eV) and it is larger than for cavity polaritons.

In Fig. 4.5d, finally, the imaginary part of the PCPs complex eigenenergies is shown. At $k_x \simeq 0.14$ the imaginary parts of the upper and lower polariton branches become equal to the same value $\text{Im}(E) = 10^{-3}$ eV, thereby indicating that mixed states of radiation and matter form in the PC slab. The dispersionless curve at $\text{Im}(E) = 10^{-4}$ eV in Fig. 2c corresponds to the uncoupled excitonic modes. Plotting the imaginary part of the complex polariton eigenenergies can be useful to clearly identify the point of exciton-photon resonance within the Brillouin zone, corresponding to the point in which upper and lower polariton modes have the same linewidth.

We now turn to two-dimensional periodic systems. We consider as a model system a photonic crystal membrane of GaAs patterned with a triangular lattice of air holes, with a InGaAs QW grown at the center of the core layer. The main physical properties of photonic eigenmodes in such systems have been clarified in Sec. 3.1. Only photonic modes that are even with respect to horizontal plane mirror symmetry ($\sigma_{xy} = +1$) are considered here, because they couple with the fundamental exciton eigenmode of a QW placed at the center of the core layer (antinode position for the electric field). For what concerns the QW, we assume the same parameters used for the one-dimensional case, but the fundamental exciton resonance is chosen to be

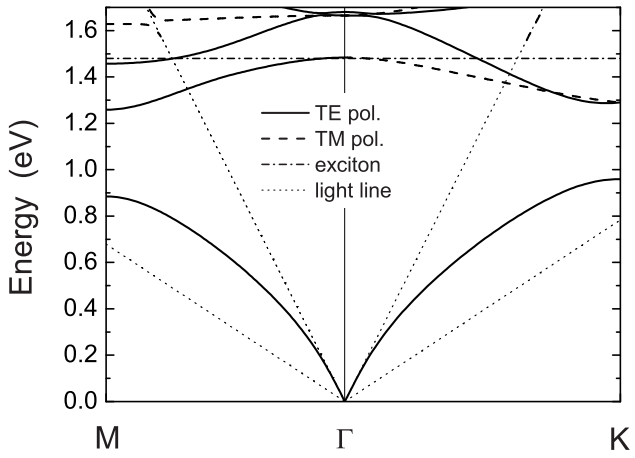

Figure 4.6: Photonic band dispersion for a 2D lattice of air holes in a dielectric membrane with parameters: $d/a = 0.4$, $r/a = 0.3$, $a = 350$ nm. The exciton fundamental level at 1.48 eV is also plotted (in absence of interaction). Only even modes with respect to the horizontal midplane ($\sigma_{xy} = +1$) are shown, and for each symmetry direction the modes are classified as odd (full lines) or even (dashed lines) with respect to the corresponding plane of incidence.

$\hbar\Omega_0 = 1.48$ eV[8]. In particular, the fundamental exciton linewidth and the oscillator strength per unit area are set to $\Gamma_{\rm ex} = 0.1$ meV and $f/S = 8.4 \times 10^{12}$ cm^{-2}, respectively. Parameters of the membrane periodic patterning are: $d/a = 0.4$, $r/a = 0.3$, $a = 350$ nm. In order to make a realistic calculation, the dielectric constant of the GaAs core layer has been set to the value $\epsilon_{\rm diel} = 12.95$, which is appropriate for GaAs at low temperature ($T \to 0$) and around the operation energy 1.48 eV. The actual observability of polaritonic effects requires, in fact, the low temperature experimental conditions. A number of 109 plane waves and 4 guided modes were taken in the basis set for the GME calculation.

The photonic band dispersion calculated along the main symmetry directions (ΓM and ΓK) for this structure is shown in Fig. 4.6, where only $\sigma_{xy} = +1$ modes are considered. The modes are further classified with respect to the symmetry operation $\hat{\sigma}_{\mathbf{k}z}$, i.e. they can be even ($\sigma_{\mathbf{k}z} = +1$) or odd ($\sigma_{\mathbf{k}z} = -1$) for mirror symmetry with respect to a given plane of incidence, identified by the symmetry direction. In Fig. 4.6 these modes are called TE-

[8]It is worth noting that the fundamental exciton resonance in, e.g., $In_xGa_{1-x}As$ QWs can vary almost continuously from 1.3 to 1.7 eV depending on the stoichiometric concentration, x, or on the doping of semiconductor materials.

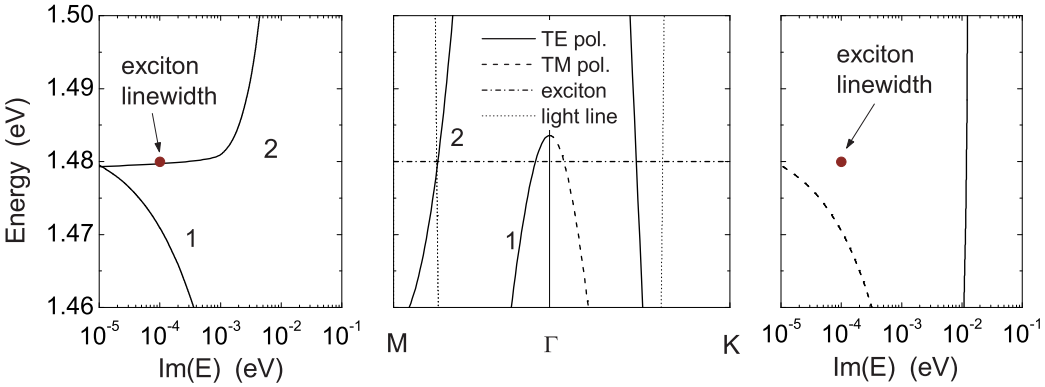

Figure 4.7: Complex energy dispersion of bare exciton and photon modes for energies around the excitonic resonance and along the main symmetry directions of the triangular lattice. Left: imaginary part of modes along ΓM. Middle: real part of modes. Right: imaginary part of modes along ΓK.

(odd) and TM-polarized (even), as they can be excited in experiments by these polarizations of incoming beam. The exciton resonance is also plotted as a dispersionless line at 1.48 eV. It can be seen that peculiar effects should arise in the two-dimensional photonic crystal slab when the exciton dispersion crosses more than one photonic mode. As it can be seen from Fig. 4.6, the exciton level crosses different photonic eigenmodes in different points of the irreducible Brillouin zone, the strong or weak coupling regime depending on the intrinsic photonic linewidth. Thus, it can happen that, within a given symmetry direction, the exciton is in strong coupling with one photonic mode and in weak coupling with the other, or it can be always in strong coupling, or only in weak coupling regimes. It should be noted that, in the absence of disorder effects, photonic crystal polariton states always form when the resonance condition occurs below the light line, owing to the vanishing imaginary part of truly guided photonic modes. In this case the polariton is non-radiative.

In order to understand the fundamental physical mechanism leading to the strong coupling regime, we plot in Fig. 4.7 the complex eigenenergies of bare exciton and photon modes in the energy window 1.46-1.50 eV. The fundamental exciton level (dot-dashed line in the middle panel) at 1.48 eV has dispersionless imaginary parts along all the symmetry directions, represented by closed points at $\mathrm{Im}(E) = 10^{-4}$ eV in the left and right hand side plots. The imaginary parts of photonic eigenmodes, calculated by the GME method and the perturbative coupling to radiative modes (see Chapter 1), display non-

trivial behavior as a function of the wave vector in the irreducible Brillouin zone.

The two photonic bands along ΓM, which are odd for mirror symmetry with respect to the plane of incidence, are marked by numbers 1 and 2 respectively. Correspondingly, the imaginary parts of mode energies for each of these two bands are plotted in the left panel of Fig. 4.7. As it can be noticed, band 2 has vanishingly radiative losses when crossing the light line and becoming a truly guided mode, while band 1 has vanishingly $\mathrm{Im}(E)$ on approaching the Γ point. The latter behavior is determined by symmetry considerations [47]. What is important to notice in the left panel of Fig. 4.7 is that in correspondence of the exciton resonance, both photonic eigenmodes have very small radiative losses ($\mathrm{Im}(E) < 10^{-3}$ eV), in particular the photonic radiative damping is much lower than the exciton-photon coupling for this structure (about 6 meV). We thus reasonably expect that photonic crystal polaritons should form at two different points in the irreducible Brillouin zone along ΓM, with two distinct anticrossings between exciton center-of-mass levels and photonic bands.

Considering now the ΓK direction, it can be seen that the two photonic modes have different symmetries with respect to the plane of incidence. In particular, the quasi-guided mode starting at the Γ point is even ($\sigma_{\mathbf{k}z} = +1$) with respect to the plane of incidence, while the other one is odd ($\sigma_{\mathbf{k}z} = -1$). The even mode has vanishingly $\mathrm{Im}(E)$ on approaching the Γ point, like the corresponding mode along ΓM. On the contrary, the odd mode has much higher radiation losses ($\mathrm{Im}(E) > 10$ meV). This means that excitons will be in strong coupling with the even band, while they will display a crossing behavior with the odd photonic mode.

We solve the quantum mechanical problem by employing 5 photonic bands and 10 exciton center-of-mass quantized eigenmodes in the basis set for the construction of the complex Hopfield matrix, for each **k**-point in the irreducible Brillouin zone. At the same time, like for the one-dimensional case, we solve the scattering matrix problem in order to calculate the angle-resolved surface reflectance for comparison between quantum and classical approaches.

In order to recover the dispersion of photonic crystal polaritons around the Γ point, TE- and TM-polarized incident plane waves have been used for reflectance calculations along ΓM and ΓK, respectively. In the scattering matrix treatment, a QW layer of width $L_{\mathrm{QW}} = 8$ nm and a LT splitting $\hbar\omega_{\mathrm{LT}} = 0.4$ meV has been assumed, which is consistent with the parameters used in the quantum calculation. Results are plotted in Fig. 4.8a and c, in which the reflectance spectra display the known features as a function of the angle of incidence, marking the excitation of the radiative eigenmodes

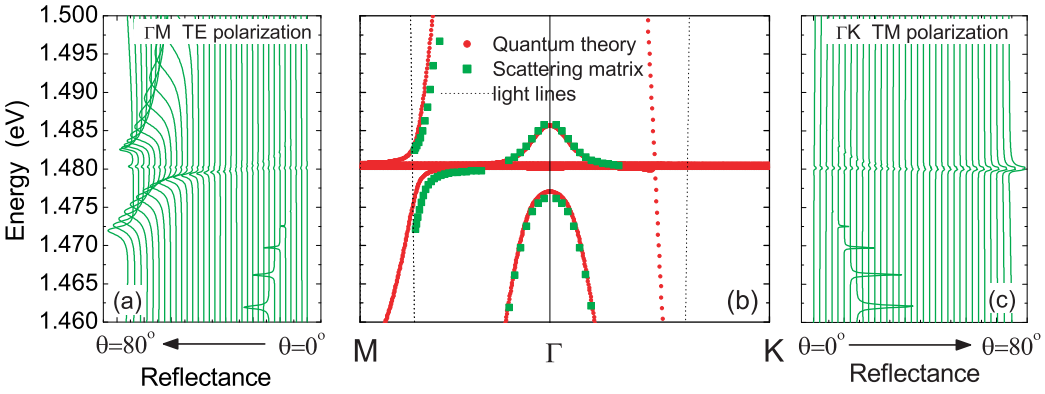

Figure 4.8: Photonic crystal polaritons in 2D triangular lattice along the main symmetry directions. Scattering matrix calculations of reflectance spectra along (a) ΓM (TE incident light) and (b) ΓK (TM incident light) are compared to quantum calculations of mode dispersion in (b): small circles are for the quantum theory results, and square points are extracted from reflectance spectra in (a) and (c).

of the structure. Even if these resonant features are not so clear as in the 1D case, it has been possible to extract the points $(k_{\|} = (\omega/c)\sin\theta, E)$ and to obtain the dispersion of these eigenmodes. The result is shown in Fig. 4.8b with square points, which are superimposed to the quantum theory calculation of eigenmode dispersion. Despite a negligible discrepancy in the high $\mathbf{k}$ region along ΓM, mainly due to the very small shift in the photonic energies caused by second-order coupling to radiative modes, which is not taken into account in the GME method (see Sec. 1.2), the overall agreement between the two complementary theoretical approaches is very satisfactory. In particular, coupled exciton-photon modes with two anti-crossings along ΓM can be seen, which confirm the arguments given from Fig. 4.7. Notice that the polariton splitting at resonance is, as in the one-dimensional case, ∼10 meV, i.e. larger than the typical values measured in III-V microcavities [116, 117, 118]. This is due, as said before, to the strong field confinement in the slab waveguide, as compared to semiconductor microcavities, where the electromagnetic field has a sizeable penetration length in the distributed Bragg reflectors. The thick line corresponding to the exciton resonance in Fig. 4.8b is due to the center-of-mass quantized energy levels calculated by solving the Schrödinger equation for the envelope function in the periodic piecewise constant potential, which are not resolved on this energy scale and appear as a continuum of modes. The crossing of the odd photonic mode and center-

of-mass quantized exciton energies along ΓK has been confirmed also by reflectance calculations (not shown here), by using a TE incident light beam. As a final remark, it should be noted that both in one- and two-dimensional case, the exciton resonance is always excited in reflectance. This is due to the fact that even in the strong coupling regime, the exciton is still radiative in the continuum of leaky modes of the effective planar waveguide. This has been also experimentally confirmed by transmission spectra in organic-based distributed feedback microcavities with an excitonic active layer in the core of the waveguide[9], as reported in Refs. [13, 98].

The results shown in this Section could be the starting point of exciting developments in this research field, and pave the way for a renewed interest in polariton physics. Even if the present work is only theoretical, there is great confidence that experimental proofs of our predictions could be made in GaAs-based systems. Calculations by the scattering matrix method represent an exact solution of Maxwell's equations, and are the theoretical realization of an angle-resolved reflectance experiment (see Apps. A and B). The main challenges for experimentalists should be the low temperature set-up conditions, the good fabrication accuracy the photonic crystal lattices, and the use of an appropriate tuning parameter. Collaborations have been started for the design and fabrication of samples in which photonic crystal polariton states could be detected.

The future perspectives, if these statements should be proved, take advantage of the past research on microcavity polaritons. We believe that many of the interesting physical properties studied in the last 10 years for planar microcavities with embedded QWs could be studied also for photonic crystal polaritons. Among the other things, the very interesting phenomenon of amplification of stimulated scattering due to the peculiar dispersion characteristics of light around the Γ point, in analogy to what has been discovered for cavity polaritons [121], greatly attracts our attention.

[9]Roughly speaking, these systems are analogous to the one represented in Fig. 4.3a, but with a weak index in-plane modulation and low index contrast along the vertical direction; the active medium is constituted by organic-based QW layers, whose excitons behave as Frenkel-type quasi-particles (i.e., not free in the plane of the QW).

Conclusions

In this work, a theoretical study of one- and two-dimensional photonic crystals embedded in planar dielectric waveguides, or photonic crystal slabs, has been presented. These systems have recently attracted much attention, because they allow for a full three dimensional control of light propagation or confinement, and they are much easier to fabricate than three-dimensional photonic crystals. The theoretical investigation of photonic crystal slabs has been undertaken by using a recently developed theoretical approach [46, 47], which has been defined Guided-Mode Expansion (GME) method.

The GME method has been described in detail in the first chapter. First of all, an introduction to the formalism and to the main physical concepts regarding photonic eigenmodes in periodic dielectric media has been provided, by introducing the plane-wave expansion method. After that, the physics of planar dielectric waveguides has been explained, and a comparison between experimental data and calculated photonic dispersion of guided modes in Silicon-on-Insulator (SOI) waveguides has been shown. This introductory Section has been intended to provide the non-specialized reader with a complete theoretical background in order to understand the GME method, which basically relies on separating the planar and vertical dynamics of the problem. Photonic eigenmodes in a photonic crystal slab are expanded in a set of factorized basis functions, which are constituted by plane waves for the planar coordinates and by the guided modes of an effective planar waveguide with spatially averaged dielectric constant for the vertical coordinate. The so called *light line issue* has been introduced and clarified, according to which only the modes whose dispersion falls below the light line of the cladding (or claddings if the waveguide is asymmetric) material are truly guided and stationary. The guided modes of the effective planar waveguide that, owing to the in-plane periodicity, are folded back into the irreducible Brillouin zone and fall above the light cone are defined *quasi-guided*. These modes have a finite radiative linewidth due to perturbative coupling to the continuum of leaky modes. A theory has been formulated to calculate both intrinsic (i.e.

due to the periodicity of the dielectric constant in the plane of the waveguide) and extrinsic (i.e. induced by disorder effects) losses in photonic crystal slabs. The approximations assumed in the numerical implementation of the method have been extensively discussed. The GME approach represents not only a fast and accurate method to calculate photonic mode dispersion and radiation losses in photonic crystal slabs, but also a clear theoretical framework for the understanding of the basic physical properties of these systems. Although it can be applied also to low contrast structures, accuracy of the method has been thoroughly checked mainly for what concerns high index contrast photonic crystal slabs, thus we have restricted our theoretical analysis to membranes or SOI structures.

The presentation of scientific results is organized into three chapters, whose main results are summarized in the following.

In Chapter 1 we have presented results for one-dimensional photonic crystal slabs, namely high index contrast and strong dielectric modulation waveguide gratings [49]. Even if these systems are known from the literature of diffraction gratings, no systematic study and fundamental understanding of their physical properties has been published before. In this chapter we address the problem of clarifying the nature of photonic eigenmodes, in both symmetric and asymmetric waveguide structures, as compared to the uniform dielectric slab and to the reference one-dimensional system, namely the well known distributed Bragg reflector. A thorough analysis of gap maps, calculated by considering both truly- and quasi-guided photonic modes, has been presented for different waveguiding layer thicknesses. The main conclusion is that a complete (i.e. common to all polarizations and parities of photonic modes) photonic band gap is generally not found in such systems, owing to the different confinement conditions of transverse and longitudinal polarization modes. This is at variance with the reference one-dimensional system for in-plane propagation, in which the two polarizations are degenerate and a complete band-gap is always found at normal incidence. A comparison with measured photonic band dispersion in SOI samples has been presented, thus showing the reliability of our theoretical approach. Then, a systematic study of intrinsic diffraction losses for quasi-guided modes in one-dimensional systems has been presented, showing the non-trivial behavior of the out-of-plane radiative mechanisms of Bloch waves as a function of band index and structure parameters.
In the second part of the chapter, a theoretical study of cavity modes in SOI-based one-dimensional photonic crystal slabs has been shown [54]. The cavity design was intended for an operation wavelength $\lambda = 1.5$ μm. The analysis of quality (Q) factors of cavity modes has been performed by using three differ-

ent theoretical approaches, namely GME, scattering matrix method (SMM), and Fourier modal expansion (FME) method. The Q-factors obtained by the FME method increase with the number of periods in the Bragg mirrors and tend to the vertical Q determined by GME or SMM methods when the effect of escape in the finite 1D structure is negligible. We have concluded that Q-factors of cavity modes can be obtained from experiments by coupling from the surface of the waveguide and measuring the reflectance of a periodized cavity system. The cavity mode in reflectance spectra is more easily detectable close to grazing (normal) incidence for structures with first- (second-) order mirrors. This may be advantageous over transmission measurements that are made difficult by the length of the structure, when the transmission in the cavity mode is very low owing to diffraction losses. Finally, a comparison between calculated and experimentally determined photonic dispersion in periodized cavity systems (realized with the proposed design) has shown a very good agreement, which is important for prospective studies on the experimental determination of Q-factors through these kind of measurements.

In Chapter 2 we addressed the problem of photonic eigenmodes in two-dimensional photonic crystal slabs. As model system, we have considered the most studied structure in literature, namely the triangular lattice of air holes both in membrane and SOI configurations. In the first part, an introduction to the basic properties and symmetry classification of quasi-guided modes has been given, and compared to dispersion properties of the uniform planar waveguide and the ideal two-dimensional photonic crystal. Then, the formation of propagating defect modes in straight line defect waveguides in the triangular lattice of air holes is described, by using the GME method with a supercell approach. In a photonic crystal slab, these defect modes can be guided, besides the total internal reflection mechanism to the dielectric/air interface, by the in-plane photonic band gap properties. This issue is a crucial one, because they could be useful as optical interconnects also with sharp bends in prospective applications to photonic integrated circuits. A comparison between GME calculations and measured dispersion characteristics of both truly- and quasi-guided photonic modes has been shown for SOI-based line defects photonic crystal waveguides with supercell repetition. A very good agreement has been found, by assuming nominal sample parameters, in particular for what concerns the theoretical fit of defect modes of both parities with respect to the plane of incidence [53].
A very important issue, for prospective applications of these systems to integrated photonics, is the non-trivial problem of out-of-plane radiation losses induced by structural imperfections of the periodic lattice [50]. In the second part of this chapter, we have shown a systematic study of disorder-induced

losses as a function of the main structural parameters and degree of disorder. The extrinsic losses of truly guided defect modes, whose dispersion lies below the cladding light line, increase quadratically with the disorder parameter. This indicates that small advances in the fabrication accuracy could lead to sensible lowering of these losses, giving rise to effective applications of these systems. For what concerns the dependence on structural parameters, extrinsic losses have been found to depend weakly on the air fraction, while they slightly increase on decreasing the core layer thickness. It has been shown that disorder-induced losses are very sensible to the increase of the channel width, i.e. to the distance of the row of holes surrounding the linear defect. In particular, propagation losses of ~ 0.15 dB/mm are predicted [52], which are definitely comparable to those of Silicon wires in the monomode frequency region [91]. These results still await for experimental confirmation, but they show that these systems are very promising in view of all-optical integration. A comparative analysis of disorder-induced losses in membrane and SOI systems has been also presented. Finally, our theoretical model has been tested through a favorably good agreement with available experimental measurements of losses in single-line defect photonic crystal waveguides made in Silicon membranes. In future developments of the present model, inclusion of side-wall roughness of each hole could be considered, with the purpose of making a direct comparison with strip Silicon waveguides and to prove the advantages of photonic crystal waveguides.

In the last Chapter we have shown the formulation of a pure quantum mechanical theory of radiation-matter interaction in photonic crystal slabs. Radiation-matter coupling in confined electronic and photonic systems has been one of the major source of research in Solid State Physics after the discovery of strong exciton-light interaction in planar microcavities with embedded quantum wells [116]. This strong coupling regime leads to the formation of mixed states of radiation and material excitations, called cavity polaritons.

In this work, we have addressed systems like one- and two-dimensional photonic crystal slabs with one or more quantum wells grown at the center of the core layer [51, 52]. The quantum well has the same in-plane periodic patterning as the photonic lattice. We assumed realistic parameters for both the dielectric material constituting the guiding layer for the electromagnetic field and the quantum well material. We assumed the latter to have a strong excitonic resonance in the energy range considered in the calculations. Our analysis has been restricted to photonic crystal membrane structures, in order to illustrate the main physical concepts of the problem. Extension to asymmetric systems are also being considered. We have shown that in photonic crystal slabs polaritonic effects can arise, and the exciton-photon cou-

pling is ~ 3 times larger than for microcavity polaritons. Results from the quantum treatment of radiation-matter interaction have been compared to semi-classical results from a scattering matrix approach, in which the quantum well layer has been assumed to have a frequency dispersive dielectric constant, showing an impressive good agreement. No adjustable parameters were considered in the calculations with the two complementary theoretical approaches. These results, if experimentally confirmed, should pave the way for new interesting research developments. Further applications of the present theory concern the study of nanocavity polariton states, in which QW excitons interact with three-dimensionally confined photonic eigenmodes in a photonic crystal membrane nanocavity. The interplay of photonic band gap properties and polaritonic effects within the same structure is expected to yield a renewed interest in topics such as the stimulated polariton scattering [121] and the polariton laser. Another interesting perspective, which has not been discussed in the present work, is the possibility to exploit high-Q photonic crystal nanocavities in order to observe strong coupling effects in three-dimensionally confined exciton and photon systems. In this case, a single quantum dot exciton should be placed at the electric field antinode position of a point defect cavity in a photonic crystal slab [55].

Future developments of the present work go in many directions, and some of them are briefly outlined here.
For what pertains one-dimensional systems, a perspective of the work presented in the first chapter is the application of GME to treat non-linear optical systems. The study of higher-order harmonics generation in waveguide-embedded photonic crystals is a very complicated problem. Concerning, e.g., second-harmonic generation in materials with a second-order optical non-linearity, gap maps calculations represent a powerful tool in order to find resonance conditions for the fundamental and the second-harmonic fields, by using different dielectric constants for the two resonant frequencies. These studies are being performed within the European project COST P11, in connection with the problem of phase-matching in one-dimensional gratings as a means for enhanced second-harmonic generation.
Disorder effects on propagation losses of linear defect modes in photonic crystal slab waveguides are being studied with the purpose of extending the model of disorder employed in the present work. In particular, a model to study scattering losses of guided modes induced by surface roughness is under investigation. This could bring a direct comparison of propagation losses between strip waveguides and photonic crystal linear waveguides of comparable dimensions. We believe that reduced scattering losses in photonic crystal waveguides can be reached with current fabrication technology, with the ad-

vantage of monomode propagation for dimensions of the system of the order of the dimensions of strip waveguides.
The study of the modifications of radiation-matter interaction induced by the spatial periodicity of the dielectric constant in the plane of the waveguide is not restricted to the strong coupling regime. In particular, peculiar modifications of spontaneous emission properties of active materials within a photonic crystal slab are expected to occur in the vicinity of a photonic band edge. Furthermore, the formation of photonic crystal polaritons in such systems opens the way for the study of stimulated polariton scattering. The quantum formalism could be extended to treat polariton-polariton scattering processes, analogous to what previously studied for microcavity polaritons [123].

The first book dedicated to the basic properties of photonic crystals dates back to 1995 [5], and it was intended as a starting tool for beginning researchers in this field. Since then, about nine years ago, a huge amount of work has been produced by the scientific community, and it is almost impossible to take account of the whole literature on this argument and of the many groups involved in photonic crystals research projects all over the world. Anyway, there is still a lot of work to do, and many physical aspects have to be clarified independently of the questions concerning the so called *killer application* of photonic crystals, which sometimes seems to be the only task moving research efforts. It is hard to predict, at the present stage, if photonic crystal-based integrated circuits will enter daily life, thus revolutionizing the technology market, but we hope that the present work can represent a useful step towards a full understanding of these interesting systems, which for physicists should be a good result regardless of application perspectives.

Appendix A

Experimental techniques

Since the beginning of the research field of photonic crystals in 1987 [2, 3], one of the main purposes has been the determination of the photonic band dispersion in photonic band gap materials, for which various methods have been proposed in the last 15 years. The most efficient technique for measuring quasi-guided modes in photonic crystal slabs, and indirectly their dispersion above the light cone, has been separately introduced in Refs. [13, 14]. It is based on the measurement of the optical transmittance or reflectance spectra at variable angles with respect to the slab surface. In the optical spectroscopy laboratory of the Department of Physics "A. Volta" of the University of Pavia, a *variable-angle reflectance* (VAR) set-up has been developed. It is worth remarking that all the experimental results shown in the present thesis have been obtained in Pavia (see also introductory notes). The VAR technique will be briefly outlined in this Appendix, and the reader will be referred to other publications for details. The present Appendix is necessary in order to better understand the comparisons between theory and experimental data shown throughout the present work.

The variable-angle reflectance

The technique basically consists in coupling an external light beam of known polarization to the photonic modes of the layered planar waveguide with a periodic patterning, as schematically shown in Fig. A.1a. These modes, folded in the first Brillouin zone owing to the periodicity in the plane, may become radiative. The excitation of a photonic mode is characterized by a particular resonant feature superimposed to the otherwise smooth reflectance spectrum of the unpatterned waveguide, coming from the interference fringes of the multilayered structure. The VAR is important also because it allows the measurement of both the real and imaginary parts of photonic eigen-

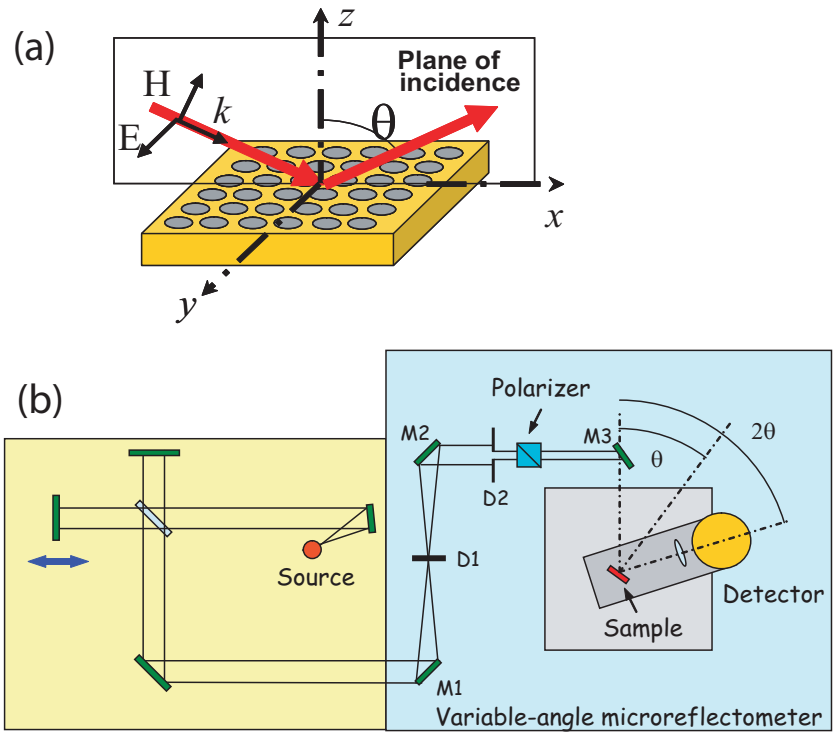

Figure A.1: (a) Geometrical scheme concerning the variable-angle reflectance experimental set-up; (b) description of the experimental realization of the variable angle reflectance set-up (courtesy of M. Galli).

modes, the latter being related to the spectral linewidth of the reflectance features. Thus, this technique can also be exploited, in principle, to estimate the propagation losses of quasi-guided modes. The same study can be performed on defect states, to infer the band dispersion and the attenuation length of guided modes in photonic crystal slab channel waveguides[1]. The angle θ is defined with respect to the direction perpendicular to the slab surface, and the polarization of the incoming beam is defined with respect to the vertical plane of incidence, as illustrated in Fig. A.1a.

The optical scheme of the set-up for variable angle reflectance is shown in A.1b. The light source is an arc lamp (both a Xenon and Mercury lamps were used) whose light, after being focused on the diaphragm (500 μm, 300 μm and 100 μ pinholes have been used, not shown in the scheme) and then collimated by a number of plane and circular mirrors, is sent in a Bruker IFS 66/S Fourier Transform spectrophotometer. The reduced light emitting area

[1]M. Galli, private communication.

of an arc lamp and so its increased brilliance with respect to normal halogen lamps give the advantage of a greater signal from the detector and so a smaller spot on the sample. At the exit of the instrument the parallel beam passes through a second diaphragm, so to reduce the numerical aperture of the system, thus increasing its angular resolution (which is better than $\pm 1^\circ$). While parallel, the light passes through a Glann-Taylor polarizer (to select between TE and TM polarized light) and is focalized on the sample by the parabolic mirror with long focal length, thus obtaining a 1 to 1 image of the pinhole on the sample's surface. The reflected light is collected by a lens and sent to the detector. The detectors used were a InSb nitrogen cooled photodiode, an InGaAs PIN photodiode and a Si photodiode. The output signal of the detector is then preamplified (integrated preamplifier in the first case, external in the second) before being sent to the electronic processing board of the IFS 66/S. Both the sample and the detector are placed on a circular rotation stage that allows them to independently rotate by an angle of 360°; furthermore, the sample is vertically placed on a x-y-z translation system with micrometric actuators in order to keep it in the optical focus of the system, choose a particular area of it (with the aid of a CCD camera) and switch between sample and reference mirror (a silver mirror, whose absolute reflectivity has been measured with the V-W method). The sample can be also rotated around an axis perpendicular to its surface, so to choose the proper lattice direction for the experiment.

How to extract, then, the photonic bands? The incoming momentum has an angle θ with respect to the vertical direction, and in general an angle ϕ with respect to the periodicity direction. The in-plane wave vector is simply determined by the kinematic process: $\mathbf{k} = (\omega/c)\sin\theta(\hat{\mathbf{x}}\cos\phi + \hat{\mathbf{y}}\sin\phi)$. Thus, for each frequency and angle of incidence of the incoming beam the corresponding wave vector is completely determined. For a fixed high symmetry direction of the periodic lattice, $\hat{\mathbf{x}}$, we can set, without loss of generality, $\phi = 0$. Then, the corresponding wave vector is simply obtained as $\mathbf{k} = (\omega/c)\hat{\mathbf{x}}\sin\theta$. By varying ω, and θ, one can sample the whole band dispersion lying above the light line along the main symmetry directions. From the energy position of the spectral resonances in VAR spectra and knowing the incident angles, the points in the $(\mathbf{k}, \omega)$ plane can be marked giving a direct measurements of photonic eigenmodes in photonic crystal slabs.

The attenuated total reflectance

An extension of this technique is the angle-resolved *Attenuated Total Reflectance* (ATR). The latter basically relies on the use of a prism between the incident beam and the sample surface, in order to couple the external

radiation to the evanescent modes of the structure, thus allowing for a direct measurement of the photonic dispersion of truly guided modes. When coupling with evanescent modes is considered, care must be taken to control the distance between the prism and the slab surface. Details concerning the practical realization of this experimental set-up are given in Ref. [53]. An example of application of ATR has been shown, e.g., in Fig. 1.6 for what concerns the measurement of truly guided modes in a homogeneous asymmetric slab made of a thin Silicon layer on a Silicon dioxide cladding. As in the case of ordinary VAR experiments, the dispersion in the $(\mathbf{k}, \omega)$ plane can be mapped by the knowledge of the incident angle and through the energy-momentum conservation law.

Appendix B

The scattering matrix method

The scattering matrix method (SMM) [31] allows to calculate reflection, transmission and diffraction for any layered structure having a one- or two-dimensional pattern, as schematically shown in Fig. B.1. It is the theoretical implementation of the experimental techniques described in App. A. The method is based on the idea of representing the electromagnetic field in each layer by two-dimensional plane-wave expansion and propagating the set of amplitudes through the layers by means of the scattering matrix, instead of the usual transfer matrix, because of better numerical stability.

Considering the j-th layer of a PhC slab, the magnetic field can be expanded on a zero-divergence plane-wave basis:

$$\begin{aligned}\mathbf{H}_{\mathbf{k},q}(\mathbf{x},z) = \quad & \sum_{\mathbf{G}} \Big(c_x(\mathbf{k}+\mathbf{G},q) \left[\hat{\mathbf{x}} - \tfrac{1}{q}(k_x+G_x)\hat{\mathbf{z}} \right] + \\ & + c_y(\mathbf{k}+\mathbf{G},q) \left[\hat{\mathbf{y}} - \tfrac{1}{q}(k_y+G_y)\hat{\mathbf{z}} \right] \Big) e^{i(\mathbf{k}+\mathbf{G})\cdot\mathbf{x}+iqz} \,, \end{aligned} \tag{B.1}$$

where $\mathbf{k}$ is the in-plane Bloch vector, q is the wave-vector along the vertical direction, $\mathbf{G}$ is a reciprocal vector and c_x, c_y are the expansion coefficients; $\hat{\mathbf{x}}, \hat{\mathbf{y}}, \hat{\mathbf{z}}$ are the axes unit vectors. Eventually, in each layer, one has to solve the following master equation

$$[\![\mathcal{H}]\!][\![\mathbf{C}]\!] = q^2 [\![\mathbf{C}]\!] \,, \tag{B.2}$$

where the form of the hamiltonian $[\![\mathcal{H}]\!]$ can be obtained by plugging the magnetic field expansion into Maxwell's curl equations. The coefficients are grouped in the vector $[\![\mathbf{C}]\!] = ([\![c_x]\!], [\![c_y]\!])^T$, where $[\![c_i]\!]_{\mathbf{G}} = c_i(\mathbf{k}+\mathbf{G}, q)$, i being either x either y. If N is the number of reciprocal vectors used in the expansion, the "hamiltonian" matrix has dimensions $2N \times 2N$. The fields in each layer can be expressed as a combination of backward and forward waves with vertical wave-vector q_n, where q_n^2 are the eigenvectors of Eq. B.2, and

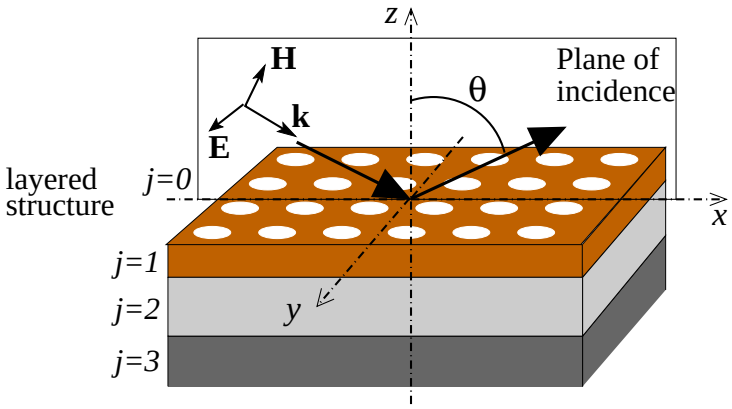

Figure B.1: Kinematics of reflection and diffraction in air. The angle of incidence θ is defined with respect to the vertical direction z. The index j labels the layers along the vertical direction.

complex amplitudes a_n and b_n. These amplitudes have to be determined by applying the boundary conditions at each dielectric interface, plus an initial condition. Since the boundary conditions are easily worked-out on the in-plane field components, it is convenient to find the relationship between the latter and the amplitudes a_n and b_n. Using the following matrix notation for the in-plane field components $[\![\mathbf{h}_\parallel(z)]\!]_\mathbf{G} = (h_x(\mathbf{k}+\mathbf{G};z), h_y(\mathbf{k}+\mathbf{G};z))^T$ the linear combination reads

$$[\![\mathbf{h}_\parallel(z)]\!] = \sum_n [\![\mathbf{C}]\!]_n \left(e^{iq_n z} a_n + e^{iq_n(d-z)} b_n\right) , \tag{B.3}$$

where $[\![\mathbf{C}]\!]_n$ are the eigenvectors of Eq. B.2, d is the thickness of the layer and $0 \leq z \leq d$. The arbitrary sign in $\sqrt{q_n^2}$ is chosen to make $\mathrm{Im}\{q_n\} > 0$. An expression similar to Eq. (B.3) holds for the electric field components.

The scattering matrix relates the amplitudes of forward and backward waves in different layers of the structure. More precisely, the ingoing waves are found in terms of the outgoing ones. Since the amplitudes are vectors of dimension $2N$, the scattering matrix $[\![S]\!]$ must have dimensions $4N \times 4N$:

$$\begin{pmatrix} [\![a]\!]_j \\ [\![b]\!]_{j'} \end{pmatrix} = [\![S(j',j)]\!] \begin{pmatrix} [\![a]\!]_{j'} \\ [\![b]\!]_j \end{pmatrix} . \tag{B.4}$$

where j and j' represent two layers. The scattering matrix contains the electromagnetic boundary conditions, i.e. continuity of the in-plane field components of $\mathbf{E}$ and $\mathbf{H}$. In a reflectance calculation, if $j = 0$ labels the surface and $j = N$ the substrate, $[\![a]\!]_0$ is determined by the incident geometry and

$[\![b]\!]_N = 0$, and thus $[\![b]\!]_0$ refers to reflected and diffracted waves at the surface, while $[\![a]\!]_N$ is for transmitted and diffracted waves in the substrate (see Fig. B.1). The SMM is particularly suited for modelling realistic conditions, including both material dispersion, $\epsilon(\omega)$, and absorption, $\mathrm{Im}\{\epsilon\} \neq 0$.

The incident TE or TM plane wave has to be translated into the amplitude $[\![a]\!]_0$. If the lattice period is sufficiently short that the in-plane wave-vector lies within the Brillouin zone, the incident fields correspond to the $\mathbf{G} = \mathbf{0}$ components of the amplitudes $[\![a]\!]_0$ and the others ($\mathbf{G} \neq 0$) are all zero. The reflected wave (r) is obtained from the $\mathbf{G} = 0$ component of the amplitude $[\![b]\!]_0$, which is then resolved into TE-TM polarization using the polarization projector operators. The reflection coefficient R is simply the Poynting vector of the reflected wave. All the $\mathbf{G} \neq \mathbf{0}$ components of $[\![b]\!]_0$ correspond to evanescent waves and contribute to the near field.
When the in-plane wave-vector of the incident wave is sufficiently large to lie outside the Brillouin zone, diffraction takes place. If $\mathbf{G}$ is the reciprocal vector that brings the ave-vector inside the Brillouin zone, the incident wave provides the $\mathbf{G}$-th components to $[\![a_0]\!]$, while all others are zero. The reflected wave is obtained by taking the same $\mathbf{G}$-th components of the fields calculated from $[\![b]\!]_0$. All the other components corresponding to non evanescent waves will contribute to diffraction (D). The same rule apply for transmission and diffraction in the substrate. If all media are lossless, then $(T + R + D)^{(\mathrm{TE})} + (T + R + D)^{(\mathrm{TM})} = 1$. On the contrary, in the presence of absorption, the sign $=$ must be replaced by $<$.

Bibliography

[1] E.M. Purcell, "Spontaneous emission probabilities at radio frequencies," *Phys. Rev.* **69**, 681 (1946).

[2] E. Yablonovitch, "Inhibited spontaneous emission in Solid-State Physics and electronics," *Phys. Rev. Lett.* **58**, 2059 (1987).

[3] S. John, "Strong localization of photons in certain disordered dielectric superlattices," *Phys. Rev. Lett.* **58**, 2486 (1987).

[4] A. Yariv and P. Yeh, *Optical Waves in Crystals* (Wiley, New York, 1984).

[5] J.D. Joannopoulos, R.D. Meade, and J.N. Winn, *Photonic Crystals: Molding the Flow of Light* (Princeton University Press, Princeton, 1995).

[6] K. Sakoda, *Optical Properties of Photonic Crystals* (Springer, Berlin, 2001).

[7] S.G. Johnson and J.D. Joannopoulos, *Photonic Crystals: The Road from Theory to Practice* (Kluwer Academic Publishers, Boston, 2002).

[8] G. Grosso and G. Pastori Parravicini, *Solid State Physics* (Academic Press, London, 2000).

[9] T.F. Krauss, R.M. De La Rue, and S. Brand, "Two-dimensional photonic-bandgap structures operating at near-infrared wavelengths," *Nature* **383**, 699 (1996).

[10] D. Labilloy, H. Benisty, C. Weisbuch, T.F. Krauss, R.M. De La Rue, V. Bardinal, R. Houdré, U. Oesterle, D. Cassagne, and C. Jouanin, "Quantitative measurement of transmission, reflection and diffraction of two-dimensional photonic band gap structures at near-infrared wavelengths," *Phys. Rev. Lett.* **79**, 4147 (1997).

[11] H. Benisty, C. Weisbuch, D. Labilloy, M. Rattier, C.J.M. Smith, T.F. Krauss, R.M. De La Rue, R. Houdré, U. Oesterle, C. Jouanin, and D. Cassagne, "Optical and confinement properties of two-dimensional photonic crystals," *J. Lightwave Technol.* **17**, 2063 (1999).

[12] E. Chow, S.Y. Lin, S.G. Johnson, P.R. Villeneuve, J.D. Joannopoulos, J.R. Wendt, G.A. Vawter, W. Zubrzycki, H. Hou, and A. Alleman, "Three-dimensional control of light in a two-dimensional photonic crystal slab," *Nature* **407**, 983 (2000).

[13] T. Fujita, Y. Sato, T. Kuitani, and T. Ishihara, "Tunable polariton absorption of distributed feedback microcavities at room temperature," *Phys. Rev.* B **57**, 12428 (1998).

[14] V.N. Astratov, D.M. Whittaker, I.S. Culshaw, R.M. Stevenson, M.S. Skolnick, T.F. Krauss, and R.M. De La Rue, "Photonic band-structure effects in the reflectivity of periodically patterned waveguides," *Phys. Rev.* B **60**, R16255 (1999).

[15] V. Pacradouni, W.J. Mandeville, A.R. Cowan, P. Paddon, J.F. Young, and S.R. Johnson, "Photonic band structure of dielectric membrane periodically textured in two dimensions," *Phys. Rev.* B **62**, 4204 (2000).

[16] A.R. Cowan, P. Paddon, V. Pacradouni, and J. Young, "Resonant scattering and mode-coupling in two-dimensional textured planar waveguides," *J. Opt. Soc. Am.* A **18**, 1160 (2001).

[17] M. Galli, M. Agio, L.C. Andreani, L. Atzeni, D. Bajoni, G. Guizzetti, L. Businaro, E. Di Fabrizio, F. Romanato, and A. Passaseo, "Optical properties and photonic bands of GaAs photonic crystal waveguides with tilted square lattice," *Eur. Phys. J.* B **27**, 79 (2002).

[18] A.D. Bristow, V.N. Astratov, R. Shimada, I.S. Culshaw, M.S. Skolnick, D.M. Whittaker, A. Tahraoui, and T.F. Krauss, "Polarization conversion in the reflectivity properties of photonic crystal waveguides," *IEEE J. Quantum Electron.* **38**, 880 (2002).

[19] M. Patrini, M. Galli, F. Marabelli, M. Agio, L.C. Andreani, D. Peyrade, and Y. Chen, "Photonic bands in patterned Silicon-on-Insulator waveguides," *IEEE J. Quantum Electron.* **38**, 885 (2002).

[20] D. Peyrade, E. Silberstein, Ph. Lalanne, A. Talneau, and Y. Chen, "Short Bragg mirrors with adiabatic modal conversion," *Appl. Phys. Lett.* **81**, 829 (2002).

[21] D. Peyrade, Y. Chen, A. Talneau, M. Patrini, M. Galli, F. Marabelli, M. Agio, L.C. Andreani, E. Silberstein, and Ph. Lalanne, "Fabrication and optical measurements of silicon on insulator photonic nanostructures," *Microelectron. Engin.* **61 – 62**, 529 (2002).

[22] A.D. Bristow, D.M. Whittaker, V.N. Astratov, M.S. Skolnick, A. Tahraoui, T.F. Krauss, M. Hopkinson, M.P. Croucher, and G.A. Gehring, "Defect states and commensurability in dual period $Al_xGa_{1-x}As$ photonic crystal waveguides," *Phys. Rev.* B **68**, 033303 (2003).

[23] M. Lončar, D. Nedeljković, T. Doll, J. Vučković, A. Scherer, and T.P. Pearsall, "Waveguiding in planar photonic crystals," *Appl. Phys. Lett.* **77**, 1937 (2000).

[24] N. Kawai, K. Inoue, N. Carlsson, N. Ikeda, Y. Sugimoto, K. Asakawa, and T. Takemori, "Confined band gap in an air-bridge type of two-dimensional AlGaAs photonic crystal," *Phys. Rev. Lett.* **86**, 2289 (2001).

[25] M. Notomi, K. Yamada, A. Shinya, J. Takahashi, C. Takahashi, and I. Yokohama, "Extremely large group-velocity dispersion of line-defect waveguides in photonic crystal slabs," *Phys. Rev. Lett.* **87**, 253902 (2001).

[26] M. Lončar, D. Nedeljković, T.P. Pearsall, J. Vučković, A. Scherer, S. Kuchinsky, and D.C. Allan, "Experimental and theoretical confirmation of Bloch-mode light propagation in planar photonic crystal waveguides," *Appl. Phys. Lett.* **80**, 1689 (2002).

[27] S. Fan, P.R. Villeneuve, J.D. Joannopoulos, and E.F. Schubert, "High extraction efficiency of spontaneous emission from slabs of photonic crystals," *Phys. Rev. Lett.* **78**, 3294 (1997).

[28] S.G. Johnson, S. Fan, P.R. Villeneuve, J.D. Joannopoulos, and L.A. Kolodziejski, "Guided modes in photonic crystal slabs," *Phys. Rev.* B **60**, 5751 (1999).

[29] S.G. Johnson, P.R. Villeneuve, S. Fan, and J.D. Joannopoulos, "Linear waveguides in photonic crystal slabs," *Phys. Rev.* B **62**, 8212 (2000).

[30] M. Qiu, "Band gap effects in asymmetric photonic crystal slabs," *Phys. Rev.* B **66**, 033103 (2002).

[31] D.M. Whittaker and I.S. Culshaw, "Scattering-matrix treatment of patterned multilayer photonic structures," *Phys. Rev.* B **60**, 2610 (1999).

[32] S.G. Tikhodeev, A.L. Yablonskii, E.A. Muljarov, N.A. Gippius, and T. Ishihara, "Quasiguided modes and optical properties of photonic crystal slabs," *Phys. Rev.* B **66**, 045102 (2002).

[33] A. Chutinan and S. Noda, "Waveguides and waveguide bends in two-dimensional photonic crystal slabs," *Phys. Rev.* B **62**, 4488 (2000).

[34] T. Ochiai and K. Sakoda, "Dispersion relation and optical transmittance of a hexagonal photonic crystal slab," *Phys. Rev.* B **63**, 125107 (2001).

[35] G.R. Hadley, "Out-of-plane losses of line-defect photonic crystal waveguides," *IEEE Photon. Technol. Lett.* **14**, 642 (2002).

[36] S. Fan and J.D. Joannopoulos, "Analysis of guided resonances in photonic crystal slabs," *Phys. Rev.* B **65**, 235112 (2002).

[37] E. Silvestre, J.M. Pottage, P.S.J. Russell, and P.J. Roberts, "Design of thin-film photonic crystal waveguides," *Appl. Phys. Lett.* **77**, 942 (2000).

[38] J. Čtyroký, "Photonic bandgap structures in planar waveguides," *J. Opt. Soc. Am.* A **18**, 435 (2001).

[39] Ph. Lalanne and H. Benisty, "Out-of-plane losses of two-dimensional photonic crystals waveguides: Electromagnetic analysis," *J. Appl. Phys.* **89**, 1512 (2001).

[40] M. Palamaru and Ph. Lalanne, "Photonic crystal waveguides: out-of-plane losses and adiabatic modal conversion," *Appl. Phys. Lett.* **78**, 1466 (2001).

[41] H. Benisty, D. Labilloy, C. Weisbuch, C.J.M. Smith, T.F. Krauss, D. Cassagne, A. Béraud, and C. Jouanin, "Radiation losses of waveguide-based two-dimensional photonic crystals: Positive role of the substrate," *Appl. Phys. Lett.* **76**, 532 (2000).

[42] T. Ochiai and K. Sakoda, "Nearly free-photon approximation for two-dimensional photonic crystal slabs," *Phys. Rev.* B **64**, 045108 (2001).

[43] K. Koshino, "Analytic approach to the optical response of one-dimensional photonic crystal slabs," *Phys. Rev.* B **67**, 165213 (2003).

[44] M. Agio, *Optical properties and wave propagation in semiconductor-based two-dimensional photonic crystals*, Ph.D. thesis, Pavia University, Italy, and Iowa State University, USA (2002).

[45] *IEEE J. Quantum Electron.* **38**, Feature Section on Photonic Crystal Structures and Applications, edited by T.F. Krauss and T. Baba, pp. 724-963 (2002).

[46] L.C. Andreani and M. Agio, "Photonic bands and gap maps in a photonic crystal slab," *IEEE J. Quantum Electron.* **38**, 891 (2002).

[47] L.C. Andreani, "Photonic bands and radiation losses in photonic crystal waveguides," *Phys. Stat. Sol.* B **234**, 139 (2002).

[48] L.C. Andreani and M. Agio, "Intrinsic diffraction losses in photonic crystal waveguides with line defects," *Appl. Phys. Lett.* **82**, 2011 (2003).

[49] D. Gerace and L.C. Andreani, "Gap maps and intrinsic diffraction losses in one-dimensional photonic crystal slabs," *Phys. Rev.* E **69**, 056603 (2004).

[50] D. Gerace and L.C. Andreani, "Disorder-induced losses in photonic crystal waveguides with line defects," *Opt. Lett.* **29**, 1897 (2004).

[51] D. Gerace, M. Agio, and L.C. Andreani, "Quantum theory of photonic crystal polaritons," *Phys. Stat. Sol.* C **1**, 446 (2004).

[52] L.C. Andreani, D. Gerace, and M. Agio, "Gap maps, diffraction losses and exciton-polaritons in photonic crystal slabs," *Phot. and Nanostruc.: Fundamentals and Applications* **2**, 103 (2004).

[53] M. Galli, M. Belotti, D. Bajoni, M. Patrini, G. Guizzetti, D. Gerace, M. Agio, L.C. Andreani, and Y. Chen, "Excitation of radiative and evanescent defect modes in linear photonic crystal waveguides," *Phys. Rev.* B **70**, 081307 (2004).

[54] D. Gerace, M. Agio, L.C. Andreani, and Ph. Lalanne, "Cavity modes in one-dimensional photonic crystal slabs," *Opt. Quant. Electron.* (2005, to be published).

[55] D. Gerace and L.C. Andreani, "Strong exciton-light coupling in photonic crystal nanocavities," *Phys. Stat. Sol.* C (2005, to be published).

[56] L. Li, "Use of Fourier series in the analysis of discontinuous periodic structures," *J. Opt. Soc. Am.* A **13**, 1870 (1996).

[57] K.M. Ho, C.T. Chan, and C.M. Soukoulis, "Existence of a photonic band gap in periodic dielectric structures," *Phys. Rev. Lett.* **65**, 3152 (1990).

[58] M. Plihal and A.A. Maradudin, "Photonic band-structure of two-dimensional systems: The triangular lattice," *Phys. Rev.* B **44**, 8565 (1991).

[59] U. Fano, "Effects of configuration interaction on intensities and phase shifts," *Phys. Rev.* **124**, 1866 (1961).

[60] V.M. Agranovich and V.E. Kravtsov, "Notes on crystal optics of superlattices," *Solid State Commun.* **55**, 85 (1985).

[61] Ph. Lalanne and G.M. Morris, "Highly improved convergence of the coupled-wave method for TM polarization," *J. Opt. Soc. Am.* A **13**, 779 (1996).

[62] R.W. Wood, "On a remarkable case of uneven distribution of light in a diffraction grating spectrum," *Phylos. Mag.* **4**, 396 (1902).

[63] J.W.S. Rayleigh, "On the dynamical theory of gratings," *Proc. Roy. Soc. London* A **79**, 399 (1907).

[64] C.K. Carniglia and L. Mandel, "Quantization of evanescent electromagnetic waves," *Phys. Rev.* D **3**, 280 (1971).

[65] R. Magnusson and S.S. Wang, "New principle for optical filters," *Appl. Phys. Lett.* **61**, 1022 (1992).

[66] L. Li and J.J. Burke, "Linear propagation characteristics of periodically segmented waveguides," *Opt. Lett.* **17**, 1195 (1992).

[67] E. Popov, "Light diffraction by relief gratings," *Progr. Optics* **31**, 141 (1993).

[68] M. Nevière, E. Popov, and R. Reinisch, "Electromagnetic resonances in linear and nonlinear optics: phenomenological study of grating behavior through the poles and zeros of the scattering operator," *J. Opt. Soc. Am.* A **12**, 513 (1995).

[69] E.G. Loewen and E. Popov, *Diffraction Gratings and Applications* (Dekker, New York, 1997).

[70] T. Tamir and S. Zhang, "Resonant scattering by multilayered dielectric gratings," *J. Opt. Soc. Am.* A **14**, 1607 (1997).

[71] S.M. Norton, G.M. Morris, and T. Erdogan, "Experimental investigation of resonant-grating filter lineshapes in comparison with theoretical models," *J. Opt. Soc. Am.* A **15**, 464 (1998).

[72] D.L. Brundrett, E.N. Glytsis, T.K. Gaylord, and J.M. Bendickson, "Effects of modulation strength in guided-mode resonant subwavelength gratings at normal incidence," *J. Opt. Soc. Am.* A **17**, 1221 (2000).

[73] M. Nevière, E. Popov, R. Reinisch, and G. Vitrant, *Electromagnetic Resonances in Nonlinear Optics* (Gordon and Breach, Amsterdam, 2000).

[74] Ph. Lalanne and E. Silberstein, "Fourier-modal methods applied to waveguide computational problems," *Opt. Lett.* **25**, 1092 (2000).

[75] S. Nilsen-Hofseth and V. Romero-Rochín, "Dispersion relation of guided-mode resonances and Bragg peaks in dielectric diffraction gratings," *Phys. Rev.* E **64**, 36614 (2001).

[76] E. Silberstein, Ph. Lalanne, J.P. Hugonin, and Q. Cao, "Use of grating theories in integrated optics," *J. Opt. Soc. Am.* A **18**, 2865 (2001).

[77] Q. Cao, Ph. Lalanne, and J.P. Hugonin, "Stable and efficient Bloch-mode computational method for one-dimensional grating waveguides," *J. Opt. Soc. Am.* A **19**, 335 (2002).

[78] M.G. Moharam, E.B. Grann, D.A. Pommet, and T.K. Gaylord, "Formulation for stable and efficient implementation of the rigorous coupled-wave analysis of binary gratings," *J. Opt. Soc. Am.* A **12**, 1068 (1995).

[79] E. Popov and M. Nevière, "Grating theory: new equations in Fourier space leading to fast converging results for TM polarization," *J. Opt. Soc. Am.* A **17**, 1773 (2000).

[80] J.P. Berenger, "A perfectly matched layer for the absorption of electromagnetic waves," *J. Comput. Phys.* **114**, 185 (1994).

[81] O. Painter, J. Vučković, and A. Scherer, "Defect modes of a two-dimensional photonic crystal in an optically thin dielectric slab," *J. Opt. Soc. Am.* B **16**, 275 (1999).

[82] Ph. Lalanne and J.P. Hugonin, "Bloch-wave engineering for high-Q, small-V microcavities," *IEEE J. Quantum Electron.* **39**, 1430 (2003).

[83] P.R. Villeneuve and M. Piché, "Photonic band gaps in two-dimensional square and hexagonal lattices," *Phys. Rev.* B **46**, 4969 (1992).

[84] R.D. Meade, K.D. Brommer, A.M. Rappe, and J.D. Joannopoulos, "Existence of a photonic band gap in two dimensions," *Appl. Phys. Lett.* **61**, 495 (1992).

[85] S.J. McNab, N. Moll, and Y.A. Vlasov, "Ultra-low loss photonic integrated circuit with membrane-type photonic crystal waveguides," *Opt. Express* **11**, 2927 (2003).

[86] Y. Sugimoto, Y. Tanaka, N. Ikeda, K. Asakawa, and K. Inoue, "Low-propagation loss of 0.76 dB/mm in GaAs-based single-line-defect two-dimensional photonic crystal slab waveguides up to 1 cm in length" *Opt. Express* **12**, 1090 (2004).

[87] K. Yamada, H. Morita, A. Shinya, and M. Notomi, "Improved line-defect structures for photonic-crystal waveguides with high group velocity," *Opt. Commun.* **198**, 395 (2001).

[88] M. Notomi, A. Shinya, K. Yamada, J. Takahashi, C. Takahashi, and I. Yokohama, "Structural tuning of guiding modes of line-defect waveguides of Silicon-on-Insulator photonic crystal slabs," *IEEE J. Quantum Electron.* **38**, 736 (2002).

[89] K.K. Lee, D.R. Lim, H.C. Luan, A. Agarwal, J. Foresi, and L.C. Kimerling, "Effect of size and roughness on light transmission in a Si/SiO_2 waveguide: Experiments and model," *Appl. Phys. Lett.* **77**, 1617 (2000).

[90] K.K. Lee, D.R. Lim, L.C. Kimerling, J. Shin, and F. Cerrina, "Fabrication of ultralow-loss Si/SiO_2 waveguides by roughness reduction," *Opt. Lett.* **26**, 1888 (2001).

[91] Y.A. Vlasov and S.J. McNab, "Losses in single-mode silicon-on-insulator strip waveguides and bends," *Opt. Express* **12**, 1622 (2004).

[92] H.-Y. Ryu, J.-K. Hwang, and Y.-H. Lee, "Effect of size nonuniformities on the band gap of two-dimensional photonic crystals," *Phys. Rev.* B **59**, 5463 (1999).

[93] Y. Tanaka, T. Asano, Y. Akahane, B.-S. Song, and S. Noda, "Theoretical investigation of a two-dimensional photonic crystal slab with truncated cone air holes," *Appl. Phys. Lett.* **82**, 1661 (2003).

[94] W. Bogaerts, P. Bienstman, and R. Baets, "Scattering at sidewall roughness in photonic crystal slabs," *Opt. Lett.* **28**, 689 (2003).

[95] S.G. Johnson, M.L. Povinelli, P. Bienstman, M. Skorobogatiy, M. Soljačić, M. Ibanescu, E. Lidorikis, and J.D. Joannopoulos, "Coupling, scattering, and perturbation theory: semi-analytical analyses of photonic-crystal waveguides," in *Proceedings of 5th International Conference on Transparent Optical Networks*, ed. by M. Marciniak, p. 103 (2003).

[96] A. D'Andrea and R. Del Sole, "Exciton wave functions and optical properties in a grating of quantum-well wires," *Phys. Rev.* B **46**, 2363 (1992).

[97] A.L. Yablonskii, E.A. Muljarov, N.A. Gippius, S.G. Tikhodeev, T. Fujita, and T. Ishihara, "Polariton effect in distributed feedback microcavities," *J. Phys. Soc. Jpn.* **70**, 1137 (2001).

[98] R. Shimada, A.L. Yablonskii, S.G. Tikhodeev, and T. Ishihara, "Transmission properties of a two-dimensional photonic crystal slab with an excitonic resonance," *IEEE J. Quantum Electron.* **38**, 872 (2002).

[99] S. Nojima, "Excitonic polaritons in one-dimensional photonic crystals," *Phys. Rev.* B **57**, 2057 (1998).

[100] S. Nojima, "Optical response of excitonic polaritons in photonic crystals," *Phys. Rev.* B **59**, 5662 (1999).

[101] K.C. Huang, P. Bienstman, J.D. Joannopoulos, K.A. Nelson, and S. Fan, "Field expulsion and reconfiguration in polaritonic photonic crystals," *Phys. Rev. Lett.* **90**, 196402 (2003).

[102] K.C. Huang, P. Bienstman, J.D. Joannopoulos, K.A. Nelson, and S. Fan, "Phonon-polariton excitations in photonic crystals," *Phys. Rev.* B **68**, 75209 (2003).

[103] R. Eichmann, B. Pasenow, T. Meier, T. Stroucken, P. Thomas, and S.W. Koch, "Semiconductor excitons in photonic crystals," *Phys. Stat. Sol.* B **238**, 439 (2003).

[104] D.G. Lidzey, D.D.C. Bradley, T. Virgili, A. Armitage, and M.S. Skolnick, "Room temperature polariton emission from strongly coupled organic semiconductor microcavities," *Phys. Rev. Lett.* **82**, 3316 (1999).

[105] K. Sumioka, H. Nagahama, and T. Tsutsui, "Strong coupling of exciton and photon modes in photonic crystal infiltrated with organic-inorganic layered perovskite," *Appl. Phys. Lett.* **78**, 1328 (2001).

[106] A.Y. Sivachenko, M.E. Raikh, and Z.V. Vardeny, "Excitations in photonic crystals infiltrated with polarizable media," *Phys. Rev.* A **64**, 13809 (2001).

[107] C.F. Klingshirn, *Semiconductor Optics* (Springer, Berlin, 1995).

[108] P. Yu and M. Cardona, *Fundamentals of Semiconductors* (Springer, Berlin, 1996).

[109] L.C. Andreani in: *Confined Electrons and Photons-New Physics and Devices*, edited by E. Burstein and C. Weisbuch (Plenum Press, New York, 1995).

[110] L.C. Andreani in: *Electron and Photon Confinement in Semiconductor Nanostructures*, edited by B. Deveaud, A. Quattropani, and P. Schwendimann (IOS Press, Amsterdam, 2003).

[111] K. Huang, "On the interaction between the radiation field and ionic crystals," *Proc. Roy. Soc. London* A **208**, 352 (1951).

[112] J.J. Hopfield, "Theory of the contribution of excitons to the complex dielectric constant of crystals," *Phys. Rev.* **112**, 1555 (1958).

[113] J.J. Hopfield, "Resonant scattering of polaritons as composite particles," *Phys. Rev.* **182**, 945 (1969).

[114] V.M. Agranovich, *J. Exp. Theor. Phys.* **37**, 430 (1959) [*Sov. Phys. JETP* **37**, 307 (1960)].

[115] G. Bastard, *Wave Mechanics Applied to Semiconductor Heterostructures* (Les Editions de Physique, Paris, 1989).

[116] C. Weisbuch, M. Nishioka, A. Ishikawa, and Y. Arakawa, "Observation of the coupled exciton-photon mode splitting in a semiconductor quantum microcavity," *Phys. Rev. Lett.* **69**, 3314 (1992).

[117] R. Houdré, C. Weisbuch, R.P. Stanley, U. Oesterle, P. Pellandini, and M. Ilegems, "Measurement of cavity-polariton dispersion curve from angle-resolved photoluminescence experiments," *Phys. Rev. Lett.* **73**, 2043 (1994).

[118] M.S. Skolnick, T.A. Fisher, and D.M. Whittaker, "Strong coupling phenomena in quantum microcavity structures," *Semicond. Sci. Technol.* **13**, 645 (1998).

[119] V. Savona, Z. Hradil, A. Quattropani, and P. Schwendimann, "Quantum theory of quantum-well polaritons in semiconductor microcavities," *Phys. Rev.* B **49**, 8774 (1994).

[120] V. Savona, L.C. Andreani, A. Quattropani, and P. Schwendimann, "Quantum well excitons in semiconductor microcavities: unified treatment of weak and strong coupling regimes," *Solid State Comm.* **93**, 733 (1995).

[121] P.G. Savvidis, J.J. Baumberg, R.M. Stevenson, M.S. Skolnick, D.M. Whittaker, and J.S. Roberts, "Angle-resonant stimulated polariton amplifier," *Phys. Rev. Lett.* **84**, 1547 (2000).

[122] G. Panzarini and L.C. Andreani, "Quantum theory of exciton polaritons in cylindrical semiconductor microcavities," *Phys. Rev.* B **60**, 16799 (1999).

[123] C. Ciuti, P. Schwendimann, B. Deveaud, and A. Quattropani, "Theory of the angle-resonant polariton amplifier," *Phys. Rev.* B **62**, 4825 (2000).

Acknowledgments

I would like to take the present opportunity to gratefully acknowledge my Doctoral supervisor, Prof. L. C. Andreani, for continuously supporting me, constantly being a guide during my research activities, encouraging my ideas, and giving me so many years of stimulating discussions and scientific learning. I am pleased to have these few lines to tell him that I will always bring with myself the things I have learned in the last three years, whatever will be my professional future.

Special thanks to Prof. A. Stella, for his generous support since the undergraduate years at Borromeo College, and for allowing my first teaching experiences that I will always remember as an important training ground; to M. Agio for his friendship, the theoretical aid on numerical methods and the precious suggestions provided during these years, which also helped me to face hard periods; to M. Galli for the tutorials concerning experimental measurements, which have been of priceless importance for my scientific growing. To all of them goes my genuine gratitude. Thanks to M. Belotti for his patient explanations on fabrication techniques and for providing me with some of the beautiful samples pictures shown in the present thesis.

These years at the Department of Physics "A. Volta" have been so special also thanks to the nice atmosphere created by the people constituting the Optical Spectroscopy group. In particular, I would like to thank Marco, Daniele, Cesare, Gabriele, Davide, Marco, Maddalena, Eva, Profs. G. Guizzetti and F. Marabelli. Last but not least, thanks to Paolo (a friend more than a colleague) and Francesco, of the Quantum Optics and Information group, for the stimulating work pauses and discussions.

The final part of the work, namely the one concerning the quantum theory of photonic crystal polaritons, is kindly dedicated to the memory of G. Panzarini, who is no more with us and whose previous work was of countless importance for the theoretical developments reported here, especially for the constant inspiration provided by her scientific insight.